POLITECNICO DI MILANO

MASTER OF SCIENCE IN SPACE ENGINEERING

Bearing-Only Strategies for Proximity Navigation on Cislunar Orbits

Author:
Michele CERESOLI

Supervisor:
Prof. Michèle LAVAGNA

Co-supervisor:
Giovanni ZANOTTI

School of Industrial and Information Engineering
Department of Aerospace Science and Technology

Academic Year 2019-2020

Abstract

The last decade has experienced a worldwide consolidation of numerous Moon related space missions to develop and advance the technologies required for a future exploration of Mars. Among those, NASA's Artemis program plays a dominant role, with its Lunar Orbital Platform Gateway (LOP-G) to operate as long-term modular infrastructure in deep-space. To successfully assembly and operate the Gateway, autonomous rendezvous, docking and undocking capabilities on non-keplerian orbits are required. However, despite a great deal of experience on guidance, navigation and control techniques for rendezvous in LEO has been gained through the ISS programme, no proximity operation has been autonomously performed so far in the non-keplerian regime.

In this context, the present work focuses on assessing the applicability of bearing-only navigation to perform proximity operations in the cislunar domain. This technique estimates the relative state of an observer by measuring through a single optical camera the line-of-sight angles to the target. Although this navigation solution requires simple, cheap, and lightweight navigation sensors, its application in the space environment has been sparsely studied because of inherent limitations in estimating the range. Using as a baseline existing researches in LEO, this thesis deeply investigates the impact of unobservabiity over the navigation quality in the non-keplerian regime and extends the results to any system that admits a discrete-time solution. In addition, it presents a framework to enable the implementation of computationally efficient Model Predictive Control (MPC) strategies in the Earth-Moon system.

A GNC architecture based on a Shrinking Horizon - MPC algorithm is proposed to synthetise a rendezvous trajectory, together with a novel approach to favour the target observability while respecting traditional rendezvous requirements. The results of a dedicated numerical testing campaign are presented to highlight the robustness of the proposed algorithm and its capability to meet safety and navigation requirements throughout the whole relative approach. Moreover, this thesis also offers an extensive sensitivity analysis to compare the effects of various degree of approximation on the estimation and guidance processes. Finally, the same architecture is exploited to perform relative navigation between flying distant heterogeneous non-keplerian orbits. The outcomes of this work demonstrate the applicability of bearing-only navigation to a large set of potential near-future missions in the cislunar environment, from small satellites as a primary navigation solution to a backup strategy for larger spacecraft.

Contents

List of Figures

List of Tables

List of Abbreviations

CW	**C**lohessy **W**iltshire
CR3BP	**C**ircular **R**estricted **T**hree **B**ody **P**roblem
DRO	**D**istant **R**etrograde **O**rbit
EpR3BP	**Ep**hemeris **R**estricted **T**hree **B**ody **P**roblem
EpR4BP	**Ep**hemeris **R**estricted **F**our **B**ody **P**roblem
DMC	**D**ynamic **M**odel **C**ompensation
FOWS	**F**uel **O**ptimal **W**eighted **S**um
JMC	**J**2000 **M**oon **C**entred
GNC	**G**uidance **N**avigation (and) **C**ontrol
IC	**I**nitial **C**ondition
KF	**K**alman **F**ilter
KOS	**K**eep **O**ut **S**phere
LEO	**L**ow **E**arth **O**rbit
LHS	**L**eft **H**and **S**ide
LOS	**L**ine **O**f **S**ight
LOPG	**L**unar **O**rbital **P**latform - **G**ateway
LP	**L**inear **P**rogramming
LVLH	**L**ocal **V**ertical **L**ocal **H**orizon
MOO	**M**ulti **O**bjective **O**ptimisation
MPC	**M**odel **P**redictive **C**ontrol
NAC	**N**arrow **A**ngle **C**amera
NC	**N**ormal **C**onstraint
NRHO	**N**ear **R**ectilinear **H**alo **O**rbit
QP	**Q**uadratic **P**rogramming
REF	**R**educed **E**chelon **F**orm
RHS	**R**ight **H**and **S**ide
RMC	**R**otating **M**oon **C**entred
SH-MPC	**S**hrinking **H**orizon - **M**odel **P**redictive **C**ontrol
SNC	**S**tate **N**oise **C**ompensation
SRP	**S**olar **R**adiation **P**ressure
STM	**S**tate **T**ransition **M**atrix
UKF	**U**nscented **K**alman **F**ilter
WS	**W**eighted **S**um

Chapter 1

Introduction

The last decade has experienced a worldwide consolidation of numerous Moon related space missions to develop and advance the technologies required for a future exploration of Mars. Among those, NASA's Artemis program plays a dominant role, aiming to bring back humans on the lunar surface by the mid-20s. In this framework, the Lunar Orbital Platform Gateway (LOP-G) will play a critical part as a long-term modular infrastructure, supporting activities on and around the Moon whilst allowing to conduct research and scientific experiments that require a deep-space environment (e.g., outside the protection of Earth's Van Allen radiation belts). The integration of the first two Gateway pieces is planned for 2023, with additional modules and robotics furnished by ESA, CSA, JAXA and Roscosmos to follow. The activities on the Gateway and on the lunar surface will be supported by various space transportation systems, such as the Space Launch System (SLS), the Cislunar Transfer Vehicle (CLTV) and other commercial vehicles which will deliver cargo, experiments and logistics. To enable and safely accomplish these assembly and re-supply missions, autonomous rendezvous and docking/undocking capabilities must be consolidated. In particular, although a great deal of experience on Guidance, Navigation and Control (GNC) techniques for rendezvous in Low Earth Orbit (LEO) has been gained through the International Space Station (ISS) programme, no proximity operation has been performed so far in the non-keplerian regime.

In addition, to guarantee the long-term sustainability of these future lunar exploration missions, the International Space Exploration Coordination Group (ISECG) has identified as a key point the collaboration with commercial partners through dedicated arrangements [1]. In this regard, the last years have seen the influence of private companies in the space sector to grow remarkably and few of those have already been awarded delivery contracts to the Gateway. Nevertheless, rendezvous operations generally require expensive and power-consuming hardware to measure the relative state, which can rarely be afforded on-board of small spacecraft. To bridge this gap, an alternative technique, known as bearing-only navigation (i.e., angles-only), has recently been proposed for in-orbit applications. This technique measures through a single optical camera the Line-of-Sight (LOS) angles (i.e., azimuth and elevation) to the target and thus represents a simple and low-cost solution to perform relative navigation from large distances. In particular, bearing-only measurements can be used as a primary navigation solution for small satellites to enable rendezvous with non-cooperative targets or as a back-up strategy for larger spacecraft. Even though the simplicity of this technique has spread its applications in many ground and naval operations, its implementation in the space environment has been sparsely studied because of inherent limitations in estimating the range.

In the recent years, various authors have studied the performance of bearing-only navigation in LEO, demonstrating that the observability gap can be overcome by

performing specific sets of maneuvers to alter the natural evolution of the spacecraft trajectory. Nevertheless, to the author's knowledge little research has been published to deal with this topic in the non-keplerian environment, thus the present thesis will focus on establishing the applicability of bearing-only measurements for rendezvous and proximity operation in the cislunar domain. In the remaining of this chapter, a brief literature review on the topic is reported, together with a general overview of thesis structure and objectives.

1.1 Literature Review

1.1.1 Bearing-Only Navigation

Bearing-only navigation has been studied by several authors in naval [2] [3], tracking [4] and orbit determination [5] applications. More recently, in the context of in-orbit relative motion Woffinden [6] and Grzymisch [7] have proved that a necessary and sufficient condition for observability is the execution of maneuvers that yield a difference of at least one measurement between the perturbed trajectory and its evolution if no maneuvers had occurred. Examples of unobservable control actions were also computed for impulsive and constant thrust maneuvers [7]. However, both studies exploited a linearised relative dynamic model based on Clohessy Wiltshire (CW) equations because typical non-linear observability approaches based on Lie derivatives [8] are unsuited for complex dynamic environments.

One of the first documented in-orbit demonstration of noncooperative far-range rendezvous based on bearing-only navigation was accomplished during the extended phase of the PRISMA mission in 2012, with the execution of the Advanced Rendezvous Demonstration using Global Positioning System and Optical Navigation (ARGON) experiment [9]. During the tests, a ground-in-the-loop architecture was exploited to process the images collected by the on-board camera and compute the control actions required to follow a predefined trajectory profile. In particular, the guidance strategy evaluated a safe rendezvous trajectory based on the relative eccentricity and inclination vectors; however, in- and out-of-plane maneuvers to improve observability were only chosen from a subset of already available fuel efficient solutions. Relying on the experience gained from ARGON, in 2016 a second in-orbit experiment called Autonomous Vision Approach Navigation and Target Identification (AVANTI) successfully performed two autonomous rendezvous with a noncooperative object from 13 and 3 km of initial distance, respectively [10]. Nevertheless, both missions as well as [11] identified a general lack of literature dealing with the design of rendezvous trajectory that favour the target observability while respecting safety and navigation requirements.

In this regard, few studies have developed expressions to quantify the observability of the trajectory and compute single optimal maneuvers. Woffinden [6] proposed a metric based on the relative range and the observability angle but analytical solutions were only found for very simple cases. On the other hand, Grzymisch [12] quantified the observability through the positive linear independence of the relative position vector with a maneuver and that of the natural evolution. The same author suggested an analytical closed-form expression for optimal maneuvers that yield the best possible improvement in the navigation estimate (i.e., those which maximise observability) which holds true for any system with a linear discrete-time solution. Moreover, he has also shown the possibility of combining the same observability

metric with a fuel objective to obtain a Quadratic Programming (QP) optimisation problem that can be solved multiple times along the trajectory with little computational effort [13]. Chari [14] investigated the performance of various formation geometries and concluded that the R-bar approach is much more effective at providing range observability than a V-bar approach. In particular, he shew that a motion normal to the line-of-sight yields significant improvements in the downrange uncertainty. Spurmann [15] proposed a spiraling approach based on the eccentricity and inclination vector separations to initiate a far-range approach. More recently, Mok [16] developed a one-step guidance which exploits the Fisher Information Matrix (FIM) to quantify and enhance the observability in a closed-loop architecture.

Concerning the navigation algorithms, many implementations adopt a traditional Extended Kalman Filter (EKF) to reduce the computational demands, even though it is well known the filter has weak robustness properties because of the measurement equations linearisation [17]. In this regard, Grzymisch proved the EKF performance can be enhanced by de-coupling the observable and unobservable states through a spherical coordinate parametrisation of CW's equations [18]. Additionally, he also developed a non-linear navigation filter based on a pseudo-measurement equation to overcome the EKF divergence for large initialisation errors [11].

1.1.2 Non-Keplerian Rendezvous Operations

Rendezvous operations have been researched since the beginning of the space exploration era, although with the end of the Apollo programme in 1972 the focus shifted towards proximity operations in LEO to support the development and maintenance of Skylab, Mir and the ISS. With the recent regrown interest in lunar exploration missions, several contemporary studies have explored rendezvous strategies for Near Rectilinear Halo Orbits (NRHO) because they emerged as the most promising candidate to stage the LOP-G [19] [20] [21]. In particular, Bucci [22] investigated Earth-Moon transfers and rendezvous phases with a spacecraft located on a NRHO, identifying the periselene region as an unfeasible area for proximity operations because of its numerical instability. Natural relative 6 Degrees-of-Freedom (DOF) motions for large structures in NRHO and Halo orbits have been studied by Colagrossi [23] and Colombi [24] to highlight potential exploitable features for the design of approaching and departing trajectories. In addition, the same authors have shown how relative 6 DOF Guidance and Control (CG) functions can be designed through a direct transcription of the energy optimal control problem to accomplish a rendezvous.

Alternative promising optimal control strategies rely on Model Predictive Control (MPC) techniques as they can easily account for constraints and non-linearities [25] [26]. The resulting optimisation problem is solved online and multiple times along the rendezvous approach to update the maneuver plan and contain errors provoked by uncertain estimates and environmental disturbances. In this regard, Berning [27] proposed a sup-optimal Nonlinear MPC for station-keeping on NRHOs and used a 4^{th} order Runge-Kutta scheme to numerically approximate the dynamics. Indeed, one of the major drawbacks of some MPC formulation is that they might result expensive from a computational standpoint. In this regard, a linearised model for formation flying in non-keplerian orbits was developed by Luquette [28] and successfully applied for rendezvous applications by Bucci et al. [29]. The very same model was adopted by Pesce [30] for autonomous vision-based navigation around uncooperative objects.

1.2 Thesis Objectives and Outline

The existing literature studies on bearing-only navigation are all focused on LEO applications. Thus, many of them exploit the closed-form analytical solution of Clohessy Wiltshire's equations to investigate the observability properties of various natural and forced motions. However, as highlighted by [23], the dynamics of cislunar relative motion has a completely different behaviour from that of LEO because the period of a non-keplerian orbit in the Earth-Moon system is much bigger than the duration of the rendezvous. In this regard, the research work of Grzymisch [11] has extended many bearing-only concepts to a generic discrete-time linear system and has developed a robust framework to account for observability inside a rendezvous optimisation problem. Nevertheless, the performance of that architecture have been tested only in the LEO environment.

Therefore, the main contribution of this thesis are grouped in two areas. The initial objectives are to asses the impact of unobservability over the navigation quality in the non-keplerian regime and find a general criterion to evaluate which set of maneuvers is most capable of reducing the navigation uncertainty. In particular, the goal is to identify an observability metric which holds irrespective of the environment properties so that the results here obtained can be easily generalised and employed in other scenarios. In the second place, exploiting the results of the observability analyses, this thesis develops a GNC architecture based on bearing-only navigation to perform various proximity operations in the cislunar domain.

The work of this thesis is structured as follows:

- **Chapter 2** provides an overview of the non-keplerian dynamic models: the equations for the Circular Restricted Three Body Problem (CR3BP) and high-fidelity ephemeris models are discussed. Then, an efficient discrete-time matrix approximation for the relative model is presented.
- **Chapter 3** introduces the most common formulations for non-linear navigation filters, together with their implementation for bearing-only measurements in the non-keplerian dynamics. In addition, a brief mention of real-world application is made by discussing the effects of different camera properties over the estimation errors.
- **Chapter 4** characterises the observability of bearing-only navigation in the cislunar domain and investigates the capability of various observability metrics to provide optimal observable maneuvers.
- **Chapter 5** introduces the mathematical formulation for the GNC architecture. It shows how a computationally efficient Shrinking Horizon - MPC can be developed for non-keplerian applications. Moreover, already existing observability metrics are generalised to linear time-varying systems and a novel non-linear strategy is proposed.
- **Chapter 6** presents the results of the numerical simulations performed to assess the validity of the proposed architecture. The performance of different observability metrics are compared and critically analysed from an operational perspective. In addition, a sensitivity analysis is reported to highlight the applicability of the approach on different orbital families and its robustness to various degrees of approximation.
- **Chapter 7** summaries the results obtained in this work and suggests possible future developments.

Chapter 2

Non-Keplerian Dynamics

This chapter intends to provide a complete mathematical description of all the models employed to describe the absolute and relative motion of two objects in the cislunar environment. All bodies are assumed to be point-masses, capable only of translational motion. No reference is made to their orientation in space since this investigation deals with the estimation of the relative position and velocity only.

2.1 The Circular Restricted Three Body Problem

In first approximation, an object in the cislunar space domain is influenced by the gravitational potential of both Moon and Earth, thus the classical Keplerian Two Body Problem (2BP) is unable to provide a reliable description of the motion of a spacecraft. Instead, a formulation based on the Circular Restricted Three Body Problem (CR3BP) can provide a useful framework for preliminary analyses on the dynamics of such environment.

The classical CR3BP describes the motion of a small body, with mass m_B, under the influence of two major attractors P_1 and P_2, called primaries, with masses much bigger than m_B. This assumption allows to neglect the impact of m_B over the motion of M_1 and M_2. Thus, the primaries revolve in Keplerian orbits around their common barycentre. It is further assumed that their motion is circular.

Under this hypothesis, it is possible to define a rotating frame, the *Synodic Reference Frame*, fixed with respect to the relative position of the primaries. The adoption of such frame can provide many insights on the dynamic problem and the resulting symmetry is often exploited to perform differential corrections and find periodic solutions. Let ($\hat{\mathbf{X}}$, $\hat{\mathbf{Y}}$, $\hat{\mathbf{Z}}$) be the vector basis of an inertial reference frame $\hat{I}$ and let ($\hat{\mathbf{x}}$, $\hat{\mathbf{y}}$, $\hat{\mathbf{z}}$) be the basis of the synodic reference frame $\hat{S}$, with the $\hat{\mathbf{x}}$ axis always parallel to the line between the primaries and directed towards P_2. The origin of both frames is located in the barycentre of the system with $\hat{\mathbf{z}}$ parallel to $\hat{\mathbf{Z}}$ and normal to the plane of motion of the primaries. The orientation of the synodic frame with respect to the inertial one is described by θ, the angle between $\hat{\mathbf{X}}$ and $\hat{\mathbf{x}}$. Conventionally, at the initial time the two frames are aligned and $\theta = 0$. A sketch of the system geometry is reported in Figure reffig: syn reference.

Additionally, the differential equations that govern the dynamics are normalised with respect to the physical properties of the system, so that the resulting distance between the primaries, the total mass and the angular velocity are unitary. The main characteristic quantities are defined as following:

- The characteristic length equals the distance between the two primaries and, thanks to the assumption of circular motion, is constant in time: $L^* = d_1 + d_2$.

- The characteristic mass M^* is defined as the total mass of the system. Since m_b is much smaller than M_1 and M_2, M^* equals the sum of the masses of the two primaries: $M^* = M_1 + M_2$.
- The characteristic time T^* is chosen as the inverse of the angular velocity of the system: $T^* = 1/\Omega = \sqrt{L^{*3}/(GM^*)}$. As a consequence, the dimensionless orbital period of the primaries is 2π and the normalised time equals the angle θ between the inertial and synodic frame. Moreover, also the non-dimensional universal gravitational constant becomes unitary.

All the other quantities, such as velocities, accelerations and forces, can be expressed as combinations of these three. The characteristic quantities of the Earth-Moon system are here reported:

$\mathbf{L}^*$ [km]	$\mathbf{M}^*$ [kg]	$\mathbf{T}^*$ [s]
384400	$6.045638 \cdot 10^{24}$	$3.751578 \cdot 10^5$

TABLE 2.1: Main characteristic quantities of the Earth-Moon system

The normalised system results more robust to numerical errors and the dynamics can be univocally represented by the mass-parameter μ, defined as:

$$\mu = \frac{M_2}{M_1 + M_2} \tag{2.1}$$

Exploiting this definition, the masses of the primaries are expressed as: $M_1 = 1 - \mu$ and $M_2 = \mu$. The mass parameter also defines the location of P_1 and P_2 along $\hat{\mathbf{x}}$, which are $-\mu$ and $1 - \mu$ respectively.

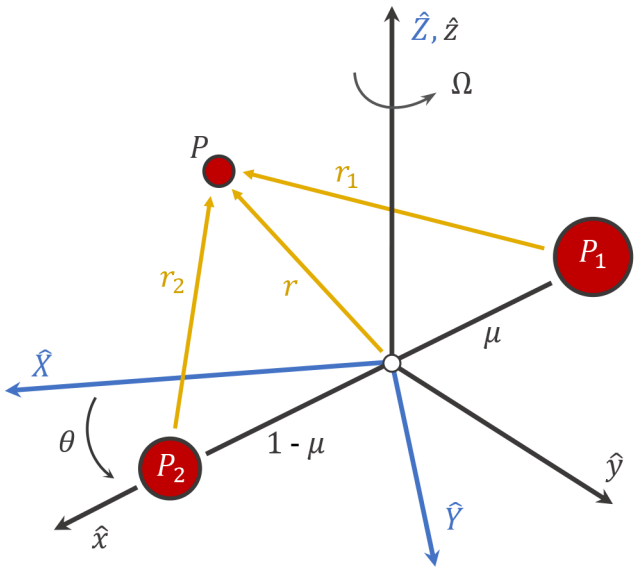

FIGURE 2.1: Geometry and reference systems of the CR3BP

A brief derivation of the CR3BP equations of motion is hereby reported; for a more comprehensive dissertation, the reader is encouraged to refer to [31]. The set of

dimensionless differential equations that rule the absolute dynamics in the inertial frame can be derived combining Newton's second law and Newton's law of gravity to obtain:

$$\ddot{\mathbf{r}} = -\frac{(1-\mu)}{r_1^3}\mathbf{r_1} - \frac{\mu}{r_2^3}\mathbf{r_2} \tag{2.2}$$

where $\mathbf{r_1}$ and $\mathbf{r_2}$ represent the relative positions of m_B with respect to the two primaries. The general kinematic relations that link the first and second-order time derivatives of a vector between an inertial and a rotating frame are:

$$\left(\frac{d\mathbf{r}}{dt}\right)_i = \left(\frac{d\mathbf{r}}{dt}\right)_r + \mathbf{\Omega}_{r/i} \times \mathbf{r} \tag{2.3}$$

$$\left(\frac{d^2\mathbf{r}}{dt^2}\right)_i = \left(\frac{d^2\mathbf{r}}{dt^2}\right)_r + 2\mathbf{\Omega}_{r/i} \times \left(\frac{d\mathbf{r}}{dt}\right)_r + \left(\frac{d\mathbf{\Omega}_{r/i}}{dt}\right)_r \times \mathbf{r} + \mathbf{\Omega}_{r/i} \times (\mathbf{\Omega}_{r/i} \times \mathbf{r}) \tag{2.4}$$

where $\mathbf{\Omega}_{r/i}$ is the angular velocity vector between the rotating and inertial frame. For the normalised case at hand $\mathbf{\Omega}_{r/i} = \hat{\mathbf{Z}}$ and $\dot{\mathbf{\Omega}}_{r/i} = 0$. Combining (2.2) with (2.4) the general dimensionless equations of motion in the synodic frame are written as:

$$\mathbf{f}(\mathbf{x}) = \begin{cases} \ddot{x} = x + 2\dot{y} - \dfrac{(1-\mu)(x+\mu)}{r_1^3} - \dfrac{\mu(x-1+\mu)}{r_2^3} \\ \ddot{y} = y - 2\dot{x} - \dfrac{(1-\mu)y}{r_1^3} - \dfrac{\mu y}{r_2^3} \\ \ddot{z} = -\dfrac{(1-\mu)z}{r_1^3} - \dfrac{\mu z}{r_2^3} \end{cases} \tag{2.5}$$

The distances from P_1 and P_2 are respectively:

$$r_1 = \sqrt{(x+\mu)^2 + y^2 + z^2} \tag{2.6}$$

$$r_2 = \sqrt{(x+\mu-1)^2 + y^2 + z^2} \tag{2.7}$$

The system (2.5) depends only on the mass parameter μ and is autonomous (i.e. time does not explicitly appear inside the equations). However, to obtain the evolution of the dynamics, a numerical integration is necessary since a closed-form analytical solution does not exist for such system. Indeed, it can be shown that in the rotating frame there is only one analytical integral of motion, known as the *Jacobi Constant*, and defined as:

$$JC = 2U^* - (\dot{x}^2 + \dot{y}^2 + \dot{z}^2) \tag{2.8}$$

where U^* is the pseudo-potential function, a modified expression of the gravitational potential:

$$U^* = \frac{1}{2}(x^2 + y^2) + \frac{1-\mu}{r_1} + \frac{\mu}{r_2} \tag{2.9}$$

The Jacobi constant is associated to the mechanical energy of m_b in the synodic frame: the lower the value of JC, the higher the energy is. Additionally, the system (2.5) admits five equilibrium solutions, called *Lagrangian points* and named after their energy level. The first three lie on the $\hat{x}$ axis and are unstable. The remaining two form equilateral triangles with the primaries and are stable only if $\mu < 0.03852$.

2.2 Ephemeris Model and Perturbations

The CR3BP is a valid tool to perform preliminary analyses on the dynamics of a spacecraft in the the cislunar space, however, for certain applications a higher fidelity propagator is deemed necessary. Indeed, such approximation neglects two factors that play an important role in the behaviour of the Earth-Moon system: the eccentricity of the primaries' orbits and the influence of other gravitational bodies (e.g., the Sun) [23][22].

In this framework, the ephemerides of the Sun and the Moon are obtained from the NASA / Jet Propulsion Laboratory (JPL) SPICE Toolkit. The model returns the positions of the two celestial bodies in the J2000 frame $\hat{J}$, an inertial reference system centered in Earth's barycentre. Denoting $(\hat{\mathbf{X}}, \hat{\mathbf{Y}}, \hat{\mathbf{Z}})$ the basis vectors, the frame is defined such that at the epoch J2000, $\hat{\mathbf{X}}$ is pointing in the direction of the mean equinox, $\hat{\mathbf{Z}}$ is orthogonal to the plane defined by the mean equator and $\hat{\mathbf{Y}}$ completes the right-handed triad.

Before describing the set of differential equations that govern the new dynamics, a few remarks are mandatory. The CR3BP equations (2.5) formulated in either $\hat{I}$ or $\hat{S}$ have as origin the barycentre of the Earth-Moon system. However, since in the ephemeris model the relative position of that point with respect to either of the primaries is not fixed, the barycentre holds no benefits anymore. Additionally, computing the trajectory of a spacecraft with respect to a central body, can usually provide more insights on the overall motion. Therefore, as the focus of this work is to investigate the bearing-only performance in the cislunar domain, the equations of motions for the N-body ephemeris model are formulated with respect to the Moon. To distinguish from the previously defined system, the J2000 frame centred in the Moon is here called the *J2000 Moon-Centred* (JMC) frame.

Further, to improve the numerical accuracy, all quantities are non-dimensionalised with respect to the characteristic quantities of the system. However, since in this model the primaries do not follow a circular motion, it is necessary to use the instantaneous characteristic quantities [32], denoted with a tilde and equal to:

$$\tilde{L} = \|\mathbf{R}_m\| \qquad \tilde{\omega} = \frac{\tilde{h}}{\tilde{L}^2} = \frac{\|\mathbf{R}_m \times \mathbf{V}_m\|}{\tilde{L}^2} \tag{2.10}$$

where $\tilde{\omega}$ is the instantaneous angular velocity. $\mathbf{R}_m$ and $\mathbf{V}_m$ are the dimensional position and velocity vectors of the Moon with respect to Earth in the J2000 frame, as obtained from the ephemerides. Then, the characteristic time is evaluated as the inverse of $\tilde{\omega}$. For obvious reasons, the characteristic mass is unchanged from Table 2.1. Once this quantities have been evaluated, all the position vectors coming from SPICE are normalised before entering the differential equations.

The spacecraft inertial acceleration as seen by P_j and subject to the gravitational influence of N-bodies is expressed, in non dimensional form, as [33]:

$$\ddot{\mathbf{r}}_{sj} = -\mu_j \frac{\mathbf{r}_{sj}}{r_{sj}^3} - \sum_{\substack{k=1 \\ k \neq j}}^{N} \mu_k \left(\frac{\mathbf{r}_{sk}}{r_{sk}^3} + \frac{\mathbf{r}_{kj}}{r_{kj}^3} \right) \tag{2.11}$$

where the vector $\mathbf{r}_{kj}$ is the relative position of the k-th body relative to P_j, the subscript s indicates the spacecraft and μ_k is the dimensionless mass of the k-th object.

Applying this equation to the Earth-Moon system in the JMC frame and temporarily neglecting the presence of other bodies, yields:

$$\ddot{\mathbf{r}}_{BM} = -\mu \frac{\mathbf{r}_{BM}}{r_{BM}^3} - (1-\mu)\left(\frac{\mathbf{r}_{BE}}{r_{BE}^3} + \hat{\mathbf{r}}_{EM}\right) \tag{2.12}$$

$\mathbf{r}_{BM}/\mathbf{r}_{BE}$ are respectively the spacecraft positions with respect to Earth and Moon, whereas $\mathbf{r}_{EM}$ is the position of Earth relative to the Moon. Notice that thanks to the normalisation step, this quantity will always be a unit vector and so the denominator is trivial. When the positions of Moon and Earth are obtained from the ephemerides, this equation represents the dynamical model for the Ephemeris Restricted Three Body Problem (EpR3BP) expressed in the JMC frame. However, the new system is non-autonomous as the relative positions vary in function of the solving epoch: different initial epochs lead to different solutions for the spacecraft motion. Thus, to allow for comparisons between different simulations, the default value of the starting epoch has been set to January 1st, 2026.

As a last remark, this model can be easily expanded to include different kinds of environmental forces, other than the gravitational actions of Earth and Moon. Among the many actors, the most common and studied perturbations are the sun's gravitational force, the solar radiation pressure and non-uniform gravity fields. Once an analytical expression for their acceleration is available, the associated term is normalised and inserted inside equation (2.12).

2.2.1 Fourth-body Effects

For the Earth-Moon scenario, the gravitational pull of the Sun is one of the most important perturbing forces and must be included in any high-fidelity model. The forth-body gravitational force in the JMC frame is easily modelled by exploiting equation (2.11):

$$\mathbf{a}_{4th} = -\mu_s \left(\frac{\mathbf{r}_{BS}}{r_{BS}^3} + \frac{\mathbf{r}_{SM}}{r_{SM}^3}\right) \tag{2.13}$$

In accordance with the notation above, $\mathbf{r}_{BS}$ is the spacecraft position relative to the Sun, $\mathbf{r}_{SM}$ is the relative position of the Sun with respect to the Moon and μ_s is the non-dimensional Sun's mass. If both relative position vectors are normalised prior to their usage in this equation, the acceleration coming from (2.13) can be directly inserted inside (2.12). The resulting dynamic system constitutes the basis of the Ephemeris Restricted Four Body Problem (EpR4BP).

2.2.2 Solar Radiation Pressure

The Solar Radiation Pressure (SRP) is the result of the interaction between the energetic photons coming from the Sun and the surface that is immersed into these particles. When the photons collide, three types of phenomena are possible: specular reflection, diffusive reflection and absorption. The intensity of each interaction depends on the surface characteristics and on the angle between the incident particles and the local surface normal. As a result, the photons exert both forces and torques on the spacecraft.

To simplify the analysis and considering that so far the satellite has been modelled as a point-mass with infinitesimal dimensions, the SRP's action is computed using

the *cannonball model* [34], which assumes the spacecraft is a sphere with radius R. The resulting force is:

$$\mathbf{a}_{SRP} = \nu \frac{\Lambda}{c} c_R A_s \hat{\mathbf{r}}_{BS} \tag{2.14}$$

where A_s is the cross-sectional absorbing area, c is the speed of light, Λ is the flux density at the distance from the Sun ($\Lambda \simeq 1350\ W/m^2$ for the Earth-Moon system) and $\hat{\mathbf{r}}_{BS}$ is the unit vector pointing from the Sun towards the spacecraft in the JMC frame. c_R is the radiation pressure coefficient that accounts for the characteristics of the surface. It varies between 1, if the momentum is completely absorbed, and 2 when all the radiation is reflected, effectively doubling the exerted force. ν is called the *shadow function* and is either equal to 0 or 1 depending on whether or not the spacecraft is shadowed. Finally, the acceleration coming from equation (2.14) must be dimensionalised using the instantaneous quantities defined in (2.10) and added to (2.12).

2.3 Coordinate Frames Transformations

Coordinate frame transformations are useful to study the motion of a spacecraft from different perspectives. For example, a periodic orbit in the synodic frame does not display the same kind of periodicity in the inertial frame. On the other hand, the shape of some resonant orbits is best analysed from an inertial viewpoint rather than a rotating one. Additionally, to transition a periodic CR3BP solution in higher-fidelity models, the spacecraft coordinates must be first converted from the $\hat{S}$ frame to the J2000 one.

2.3.1 Synodic Frame to Inertial Frame

In the context of the CR3BP, the conversion matrix from the synodic frame $\hat{S}$ to $\hat{I}$ is obtained by combining two transformations. First, using as a reference Figure 2.1, the position is easily converted by performing a clockwise rotation of θ around the $\hat{\mathbf{Z}}$-axis:

$$\mathbf{X} = \mathbf{C}_p \mathbf{x} = \begin{bmatrix} \cos\theta & -\sin\theta & 0 \\ \sin\theta & \cos\theta & 0 \\ 0 & 0 & 1 \end{bmatrix} \mathbf{x} \tag{2.15}$$

where $\mathbf{X}$ and $\mathbf{x}$ are the positions vector in the inertial and synodic frame, respectively. This expression is valid whenever the two frames are assumed to be aligned at the initial time, i.e., $\theta = 0$ at $t = 0$. If that is not the case, θ must be substituted with $(\theta + \theta_0)$. Recall that, thanks to the normalisation, θ can be used interchangeably with t. Then, an expression to rotate between synodic and inertial velocities can be obtained either by using the kinematic relationship in (2.3) or by differentiating (2.15). Since $\dot{\theta} = 1$, both methods yield:

$$\dot{\mathbf{X}} = \mathbf{C}_v \mathbf{x} + \mathbf{C}_p \dot{\mathbf{x}} = \begin{bmatrix} -\sin\theta & -\cos\theta & 0 \\ \cos\theta & -\sin\theta & 0 \\ 0 & 0 & 0 \end{bmatrix} \mathbf{x} + \mathbf{C}_p \dot{\mathbf{x}} \tag{2.16}$$

Finally, combining (2.15) and (2.16) the complete transformation is:

$$\begin{bmatrix} \mathbf{X} \\ \dot{\mathbf{X}} \end{bmatrix} = \begin{bmatrix} \mathbf{C}_p & \mathbf{0} \\ \mathbf{C}_v & \mathbf{C}_p \end{bmatrix} \begin{bmatrix} \mathbf{x} \\ \dot{\mathbf{x}} \end{bmatrix} \tag{2.17}$$

Although the CR3BP equations have been formulated with respect to the Earth-Moon barycentre, this transformation holds irrespective of the point used as origin of the synodic frame. Thus it is equally valid if the centre is set at a primary. If the opposite transformation is desired, i.e., from the inertial to the synodic frame, the transformation matrix to use is the inverse of (2.17).

2.3.2 CR3BP to Ephemeris Model

To transition a periodic solution in the synodic frame to an ephemeris model, it is necessary to express the CR3BP states in the inertial JMC frame [32]. The first step is to shift the orbital states from the barycentre of the system to the Moon. Then, the data is dimensionalised using the instantaneous characteristic quantities defined in (2.10).

Before introducing the transformation matrix, it is convenient to define an instantaneous rotating frame, here called the *J2000 Rotating Moon-Centred* (RMC) frame [24]. It is similar to the synodic frame but its basis vectors ($\hat{\tilde{\mathbf{x}}}$, $\hat{\tilde{\mathbf{y}}}$, $\hat{\tilde{\mathbf{z}}}$) are expressed relative to the J2000 frame:

$$\hat{\tilde{\mathbf{x}}} = \frac{\mathbf{R}_m}{R_m} \qquad \hat{\tilde{\mathbf{y}}} = \hat{\tilde{\mathbf{z}}} \times \hat{\tilde{\mathbf{x}}} \qquad \hat{\tilde{\mathbf{z}}} = \frac{\mathbf{R}_m \times \mathbf{V}_m}{\|\mathbf{R}_m \times \mathbf{V}_m\|} \tag{2.18}$$

where $\mathbf{R}_m$ and $\mathbf{V}_m$ are again the instantaneous position and velocity of the Moon relative to Earth in the J2000 frame. These axes are then used to construct the rotation matrix for the position vector:

$$\tilde{\mathbf{X}} = \tilde{\mathbf{C}}_p \tilde{\mathbf{x}} = \begin{bmatrix} \hat{\tilde{\mathbf{x}}} & \hat{\tilde{\mathbf{y}}} & \hat{\tilde{\mathbf{z}}} \end{bmatrix} \tilde{\mathbf{x}} = \begin{bmatrix} C_{11} & C_{11} & C_{13} \\ C_{21} & C_{22} & C_{23} \\ C_{31} & C_{32} & C_{33} \end{bmatrix} \tilde{\mathbf{x}} \tag{2.19}$$

which transforms the dimensional position vector $\tilde{\mathbf{x}}$ in the RMC frame (coming from the previous step) to $\tilde{\mathbf{X}}$, its inertial JMC counterpart. The structure of $\tilde{\mathbf{C}}_p$ does not allow for a simple analytical time-derivative. Thus, to obtain the inertial velocity, the kinematic relationship (2.3) is exploited:

$$\frac{d\tilde{\mathbf{X}}}{dt} = \frac{d\tilde{\mathbf{x}}}{dt} + \tilde{\boldsymbol{\omega}} \times \tilde{\mathbf{x}} = (\dot{\tilde{x}} - \tilde{\omega}\tilde{y})\,\hat{\tilde{\mathbf{x}}} + (\dot{\tilde{y}} + \tilde{\omega}\tilde{x})\,\hat{\tilde{\mathbf{y}}} + \dot{\tilde{z}}\hat{\tilde{\mathbf{z}}} \tag{2.20}$$

where $\tilde{\boldsymbol{\omega}}$ is the instantaneous angular velocity of the rotating frame and equals $\tilde{\omega}\hat{\tilde{\mathbf{z}}}$ by definition. Notice that, since the data comes from the ephemerides, the instantaneous dimensional angular velocity is no longer constant and unitary. The inertial velocity is then obtained by applying the transformation in equation (2.19) to (2.20) (see [32][35] for further details). The final result is:

$$\begin{bmatrix} \tilde{\mathbf{X}} \\ \dot{\tilde{\mathbf{X}}} \end{bmatrix} = \begin{bmatrix} \tilde{\mathbf{C}}_p & \mathbf{0} \\ \tilde{\mathbf{C}}_v & \tilde{\mathbf{C}}_p \end{bmatrix} \begin{bmatrix} \tilde{\mathbf{x}} \\ \dot{\tilde{\mathbf{x}}} \end{bmatrix} \tag{2.21}$$

where the matrix $\tilde{\mathbf{C}}_v$ is defined as

$$\tilde{\mathbf{C}}_v = \tilde{\omega} \begin{bmatrix} C_{12} & -C_{11} & 0 \\ C_{22} & -C_{21} & 0 \\ C_{32} & -C_{31} & 0 \end{bmatrix} \tag{2.22}$$

Equation (2.21) allows to transform a state from the RMC to the JMC frame and, whenever the opposite conversion is required, the inverse of this transformation matrix is used. However, as stated earlier, before applying the transformation, the rotating states must be dimensionalised. This step is required because the angular velocity obtained from (2.10) is dimensional. Finally, once the conversion has been applied, the primary-centred inertial states can be normalised using the very same instantaneous characteristic quantities.

In some cases it is useful to exploit the dynamics from an inertial perspective. For example, when in a navigation filter the ephemeris dynamics is approximated with the CR3BP, an accurate value for the process noise is easier to find in a fixed reference frame. In these instances, it is possible to establish a direct link between the two inertial frames using a transformation matrix similar to Equation (2.21). Additionally, since both frames are fixed by definition, the orientation of one relative to the other is constant in time. Therefore, it is only necessary to know the relative attitude at one particular moment to perform the conversion at any other time. Assuming that the synodic and inertial CR3BP frames are initially aligned, the transformation matrix from the inertial frame $\hat{I}$ to the JMC is computed in the exact same way of Equation (2.21), with the instantaneous axes evaluated at the initial epoch. It must be remarked that also in this procedure, before applying the transformation, the initial states in $\hat{I}$ must be transitioned to a Moon-centred representation and dimensionalised. The advantage of this last methodology relies in the exploitation of a constant matrix to perform the conversion.

2.4 Generation of Periodic Orbits

The inherent nature of the three body problem is chaotic and the resulting motion is extremely sensitive to the selection of the initial conditions. Thus, periodic orbital solutions can only be found through numerical correction algorithms. In literature, one of the most common techniques is to exploit a multiple-targetting scheme combined with a Newton-Rhapson solver. Such methodology is well discussed in [23] [36] [37], therefore only a short summary is here reported.

2.4.1 Differential Corrector

Given the potential initial conditions $\mathbf{X}_0$, the purpose of the algorithm is to correct their values to enforce a periodic behaviour. Assume a set of n design variables $\mathbf{X}$ subject to m constraints expressed as $\mathbf{F}(\mathbf{X})$. Then, $\mathbf{X}^*$ is identified as a solution if it satisfies $\mathbf{F}(\mathbf{X}^*) = 0$ under reasonable tolerances. Starting from the initial guess, the constraint equation can be expanded in a Taylor series as:

$$\mathbf{F}(\mathbf{X_0} + \delta\mathbf{X}) \approx \mathbf{F}(\mathbf{X_0}) + \mathcal{D}\mathbf{F}(\mathbf{X_0})\delta\mathbf{X} \approx \mathbf{0} \tag{2.23}$$

where $\mathcal{D}\mathbf{F}(\mathbf{X_0})$ is the Jacobian of the constraint function with respect to the free-variables vector $\mathbf{X}$. Whenever the number of constraints is smaller than the number of independent variables, a minimum norm solution of (2.23) is sought to update the current guess. The new guess at each iteration is obtained as:

$$\mathbf{X}_{k+1} = \mathbf{X}_k - \mathcal{D}\mathbf{F}(\mathbf{X}_k)^T \left[\mathcal{D}\mathbf{F}(\mathbf{X}_k) \cdot \mathcal{D}\mathbf{F}(\mathbf{X}_k)^T\right]^{-1} \mathbf{F}(\mathbf{X}_k) \tag{2.24}$$

If a single-shooting method is used, the constraint vector simply enforces the periodicity between the initial and final state. On the other hand, if a multiple-shooting

scheme is exploited, the trajectory is discretised into N patch points and the constraint vector is augmented to enforce the continuity across the $N-1$ arcs.

Analytical solutions for the Jacobian $\mathcal{D}\mathbf{F}(\mathbf{X})$ in equation (2.24) are easily derived by making use of linear variational equations. These last allow to study the motion in the neighbourhood of a reference solution by mapping a perturbation of the initial states to a variation on the final ones through the usage of a *state transition matrix*, defined as:

$$\mathbf{\Phi}(t, t_0) = \frac{\partial \mathbf{X}}{\partial \mathbf{X}_0} \tag{2.25}$$

The properties of this matrix are well-discussed in section 2.5.2. Analytical expressions for the evaluation of both (2.24) and (2.25) are available in [24] [36]. For what concerns the initial guess, different methods can be exploited to compute the variables required to run the algorithm, e.g., analytical approximations near the equilibrium points, Poincarè maps, exploitation of the Monodromy matrix eigenvectors and heuristic methods. A good number of initial conditions for different families of periodic solutions can be found in [38].

Generally, the multiple-shooting technique results more reliable and is particularly useful to transition a periodic solution from the CR3BP to the ephemeris model. The first step is to discretise the trajectory into a series of patch points, with the number that depends on the sensitivity of the orbit. Then, to enforce a quasi-periodic behaviour, the previous points are duplicated and stacked together to obtain the desired number of revolutions. However, note that a large number of revolutions makes the problem harder to solve and depending on the stability of the target orbit, in some cases a solution may not be found. Finally, the patch points are transformed to the *JMC* frame at the associated epochs and a correction technique is applied to converge towards a continuous quasi-periodic solution.

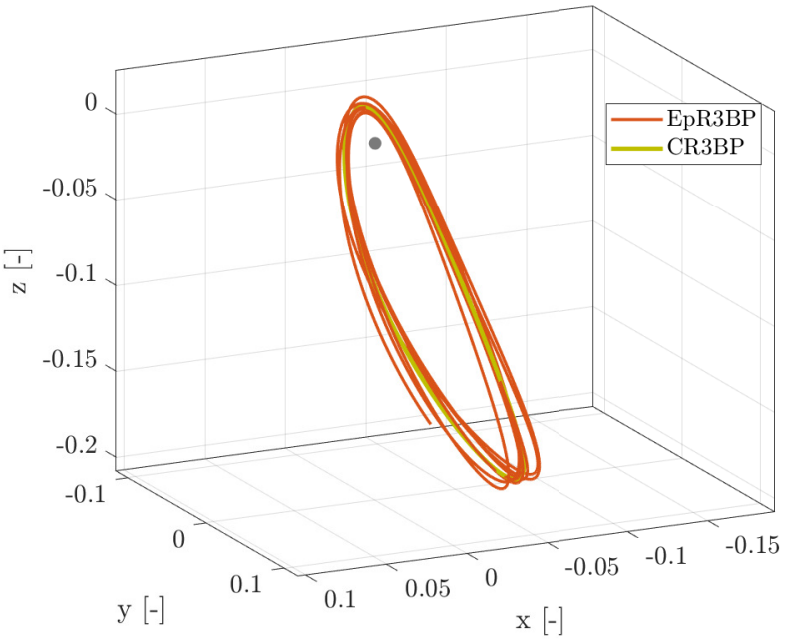

FIGURE 2.2: Comparison between the original CR3BP periodic orbit and the associated quasi-periodic solution in the EpR3BP for a L2 Southern NRHO orbit in the RMC frame

Additionally, if perturbations are added to the dynamics, the newly found solutions may diverge early on. To compensate for their effects, it is possible to include their contribution inside (2.25). Then, the aforementioned correction procedure is exploited using as baseline the EpR3BP quasi-periodic solution found at the previous step.

2.4.2 Continuation Methods

Once a periodic orbit has been obtained, additional orbits can be found exploiting the information of the first solution. The two most common numerical techniques are the single-parameter and the pseudo-arc length continuation methods. The former modifies only one parameter of the first solution and then seeks a new periodic orbit. Instead, the pseudo-arc length algorithm continues in a direction tangent to the null-space of the Jacobian matrix in (2.24). Its major advantage is that it does not require any a-priory knowledge on the geometry of the orbits to expand the family [23]. A very similar method is presented in [37], where an additional constraint is included to fix the relative distance between two adjacent initial solutions. This way, a smooth visualisation of the whole family is easily obtained. Moreover, to ensure that the future members are moving in the same direction, the sign of the null-space $\boldsymbol{\nu}$ is selected to enforce the following inequality:

$$\boldsymbol{\nu} \cdot (\mathbf{X}_{k+1} - \mathbf{X}_k) > 0 \tag{2.26}$$

Finally, note that in some sensitive regions, the selected step-size between one orbit and the other might be too large. In such cases it is convenient to adaptively reduce its size until a solution is found.

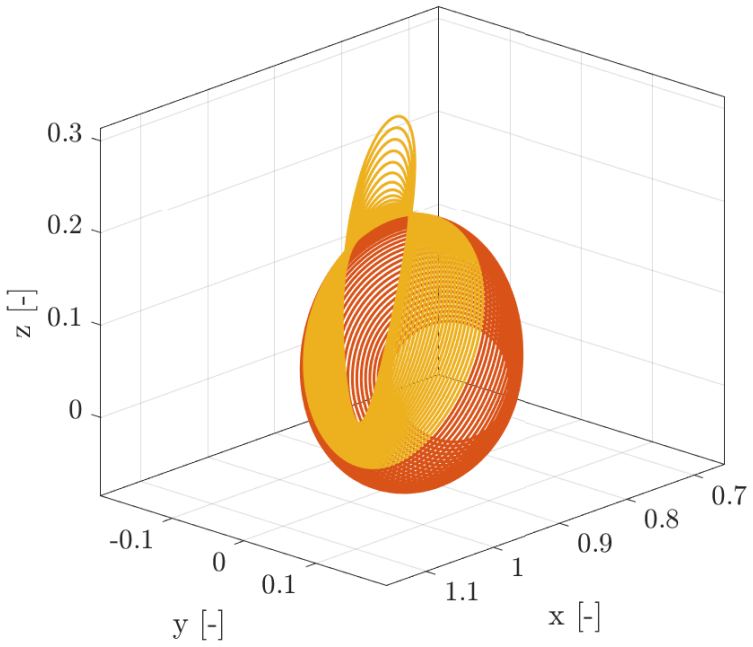

FIGURE 2.3: Family of periodic Halo (*red*) and NRHO (*yellow*) orbits around L1, computed in the CR3BP

2.5 Relative Dynamics

The relative translational dynamics is easily obtained by differentiating the definition of the relative position vector of the chaser with respect to the target, denoted as $\mathbf{x}$:

$$\ddot{\mathbf{x}} = \ddot{\mathbf{r}}_C - \ddot{\mathbf{r}}_T \tag{2.27}$$

The expressions of $\ddot{\mathbf{r}}_C$ and $\ddot{\mathbf{r}}_T$ are obtained either from equation (2.5) or (2.12) and represent the absolute acceleration vectors of the two spacecraft. The relative state in (2.27) are expressed accordingly to the frame used to evaluate the absolute dynamics, be it the inertial or the rotating one. Notice that the propagation of the relative dynamics always requires the knowledge of the relative variables and the absolute state of either the chaser or the target. However, in a typical bearing-only implementation, the chaser is only equipped with a camera that measures its relative state with respect to the target. It is then necessary to obtain additional information regarding the absolute dynamics by communicating with the target itself or through the help of ground-stations. This characteristic is a fundamental difference with respect to classical LEO relative dynamics models, which require knowledge of only the 6 relative states. The practical consequences of this will be further analysed in the next sections.

2.5.1 Linearised Relative Dynamics

Although the non-Keplerian environment is strongly non-linear, the relative dynamics can be linearised with respect to the target position by applying a first-order Taylor expansion, under the assumption that the relative distance between the spacecraft is much smaller than the distance between the target and the primaries [28]. The linearised relative dynamics is expressed in the inertial frame as:

$$\begin{bmatrix} \dot{\mathbf{x}} \\ \ddot{\mathbf{x}} \end{bmatrix} \approx \begin{bmatrix} \mathbf{0} & \mathbf{I}_3 \\ \Xi(t) & \mathbf{0} \end{bmatrix} \begin{bmatrix} \mathbf{x} \\ \dot{\mathbf{x}} \end{bmatrix} + \begin{bmatrix} \mathbf{0} \\ \mathbf{I}_3 \end{bmatrix} (\mathbf{u} + \delta\mathbf{a}) \tag{2.28}$$

where $\mathbf{I}_3$ is a $3x3$ identity matrix, $\mathbf{u}$ is the control input and $\delta\mathbf{a}$ is the contribution of the environmental perturbing accelerations. The matrix $\Xi(t)$ depends only on the absolute position of the target (which is in turn function of time), and is defined as:

$$\Xi(t) = -\left(\frac{1-\mu}{r_{T_1}^3} + \frac{\mu}{r_{T_2}^3}\right)\mathbf{I}_3 + 3\frac{1-\mu}{r_{T_1}^3}\left[\hat{\mathbf{r}}_{T_1}\hat{\mathbf{r}}_{T_1}^{\mathrm{T}}\right] + 3\frac{\mu}{r_{T_2}^3}\left[\hat{\mathbf{r}}_{T_2}\hat{\mathbf{r}}_{T_2}^{\mathrm{T}}\right] \tag{2.29}$$

where $\hat{\mathbf{r}}_{T_1}$ and $\hat{\mathbf{r}}_{T_2}$ identify the relative inertial unit position vectors between the target and the two primaries. The great advantages introduced by this approximate formulation are related to the possibility of exploiting the techniques of the linear control theory to design the trajectory profile for the proximity dynamics. An additional benefit of equation (2.28) is that it does not make any assumptions on the model used to propagate the dynamics, thus it can be straightforwardly adapted to work either in the CR3BP or with the ephemeris model by changing the expression of the primaries position vectors. To express equation (2.28) in a rotating frame, the whole system has to be modified to account for the presence of non-inertial contributions. Combining the transformation relationships of (2.17) with (2.28), the linearised

relative dynamics in the rotating frame is:

$$\begin{bmatrix}\dot{\mathbf{x}}\\ \ddot{\mathbf{x}}\end{bmatrix} = \begin{bmatrix}\mathbf{0} & \mathbf{I}_3\\ \boldsymbol{\Xi}(t) + [\dot{\boldsymbol{\Omega}}\times] - [\boldsymbol{\Omega}\times][\boldsymbol{\Omega}\times] & -2[\boldsymbol{\Omega}\times]\end{bmatrix}\begin{bmatrix}\mathbf{x}\\ \dot{\mathbf{x}}\end{bmatrix} + \begin{bmatrix}\mathbf{0}\\ \mathbf{I}_3\end{bmatrix}(\mathbf{u} + \delta\mathbf{a}) \tag{2.30}$$

where $[\boldsymbol{\Omega}\times]$ is a skew-symmetric matrix containing the components of the synodic angular velocity vector $\boldsymbol{\Omega}$ (the subscript $_{r/i}$ has been dropped to improve readability). For the CR3BP, the equation can be further simplified recalling that $\dot{\boldsymbol{\Omega}} = \mathbf{0}$:

$$\begin{bmatrix}\dot{\mathbf{x}}\\ \ddot{\mathbf{x}}\end{bmatrix} = \begin{bmatrix}\mathbf{0} & \mathbf{I}_3\\ \boldsymbol{\Xi}(t) - [\boldsymbol{\Omega}\times][\boldsymbol{\Omega}\times] & -2[\boldsymbol{\Omega}\times]\end{bmatrix}\begin{bmatrix}\mathbf{x}\\ \dot{\mathbf{x}}\end{bmatrix} + \begin{bmatrix}\mathbf{0}\\ \mathbf{I}_3\end{bmatrix}(\mathbf{u} + \delta\mathbf{a}) \tag{2.31}$$

Notice that the expression of $\boldsymbol{\Xi}(t)$ has remained unchanged; the only difference is that $\hat{\mathbf{r}}_{T_1}$ and $\hat{\mathbf{r}}_{T_2}$ (and all other quantities), are now evaluated in the synodic frame. As a last comment, a similar linearisation process can be carried out using as a reference the chaser rather than the target. If this were the case, $\boldsymbol{\Xi}(t)$ would contain only the information regarding the former spacecraft. However, from a GNC perspective, such formulation does not result convenient at all. A detailed explanation is given in section 5.3.1.

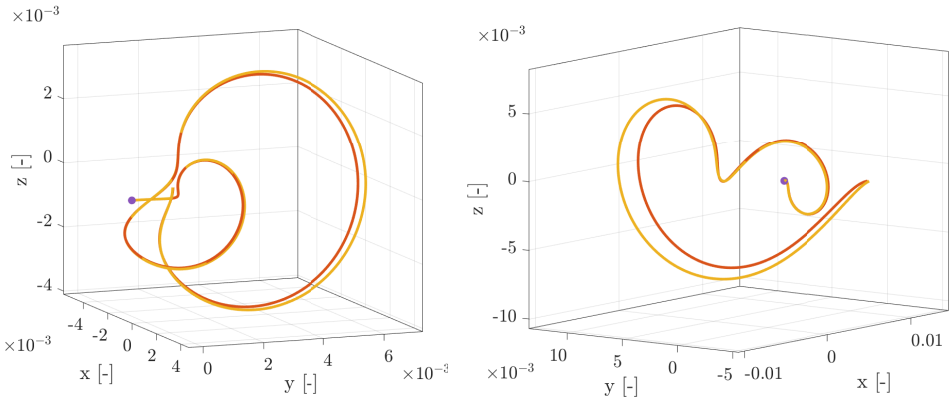

(*a*) Central manifold

(*b*) Unstable manifold

FIGURE 2.4: Comparison between the exact (*red*) and linear (*yellow*) relative dynamics at an initial distance of 500 km. The starting point is marked with a violet dot.

In the figure above, the dynamics has been propagated for two periods of the target orbit. The highest errors between the two models are reached when the reference spacecraft is in the perilune region, where the linear formulation fails to accurately reproduce the gravitational action.

2.5.2 State Space Formulation

The systems in equations (2.28) and (2.31) can be written in state-space form as:

$$\dot{\mathbf{x}} = \mathbf{A}(t)\mathbf{x} + \mathbf{B}\mathbf{u} \tag{2.32}$$

A closed-form solution of this system does not exist since $\mathbf{A}$ is dependent on the absolute dynamics of the target, which requires a numerical integration. Nevertheless,

given $\mathbf{x}(t_0)$ and $\mathbf{u}(t)$ the solution of (2.32) can be separated into two contributions:

$$\mathbf{x}(t) = \mathbf{\Phi}(t, t_0)\mathbf{x}(t_0) + \int_{t_0}^{t} \mathbf{\Phi}(t, \tau)\mathbf{B}\mathbf{u}(\tau)d\tau \tag{2.33}$$

where the two terms are associated to the system free and forced responses, respectively. The matrix function $\mathbf{\Phi}(t, \tau)$, is called the *state transition matrix* (STM) and has the following properties:

$$\begin{aligned} &\dot{\mathbf{\Phi}}(t, \tau) = \mathbf{A}(t)\mathbf{\Phi}(t, \tau) \\ &\mathbf{\Phi}(\tau, \tau) = \mathbf{I} \\ &\mathbf{\Phi}(t_2, t_0) = \mathbf{\Phi}(t_2, t_1)\mathbf{\Phi}(t_1, t_0) \end{aligned} \tag{2.34}$$

It is possible to show that if $\mathbf{A}(t)$ is continuous or piece-wise continuous, $\mathbf{\Phi}$ exists and is unique. Considering our expression of $\mathbf{A}$, the only problems arise when the position of the target corresponds with one of the two primaries (i.e., the denominators nullify). However, these scenarios are physically impossible, thus the solution to equation (2.34) always exists. Since an analytical expression is not available, we are limited to a numerical solution of (2.34 a) with (2.34 b) as boundary condition. Given a time interval $[t_k,\ t_{k-1}]$, different strategies are available to compute $\mathbf{\Phi}(t_k, t_{k-1})$; the simpler is to integrate numerically the target absolute dynamics simultaneously with (2.34 a/b), to obtain:

$$\mathbf{\Phi}(t_k, t_{k-1}) = \int_{t_{k-1}}^{t_k} \mathbf{A}(\mathbf{x}_t(\tau))\mathbf{\Phi}(\tau,\ t_{k-1})\, d\tau \quad \text{with} \quad \mathbf{\Phi}(t_{k-1}, t_{k-1}) = \mathbf{I}_6 \tag{2.35}$$

where the dependence of $\mathbf{A}$ on the target state $\mathbf{x}_t$ has been made explicit. Once $\mathbf{\Phi}(t_k, t_{k-1})$ is known, the natural evolution of the relative dynamics is immediately available from the first term of (2.33). A remarkable difference with respect to classic relative models, such as the Clohessy-Wiltshire (CW) equations, other than the inexistence of an analytical solution is that the model in (2.32) is a time-varying linear system, thus:

$$\mathbf{\Phi}(t_k + \Delta t, t_k) \neq \mathbf{\Phi}(t_i + \Delta t, t_i) \quad \text{if} \quad t_i \neq t_k \tag{2.36}$$

Indeed, the dependence of $\mathbf{\Phi}$ on the target state generates different results for different initial times since $\mathbf{x}_t(t_i) \neq \mathbf{x}_t(t_k)$. Therefore, it is necessary to compute $\mathbf{\Phi}$ at each discretisation time even if a uniform time-step is adopted.

The solution of the forced response is more complicated and only in few cases the convolution integral of the time-varying maneuver $\mathbf{u}(t)$ can be written as the product between a matrix and a vector. The solution for two basic types of maneuvers is here derived by explicitly substituting the value of $\mathbf{u}$. For impulsive controls at the beginning of the time interval, the input is defined as: $\mathbf{u}(t) = \mathbf{u}\delta(t)$, where the Dirac-delta $\delta(t - \tau)$ is used to describe an impulse at time τ. Substituting inside the integral yields:

$$\int_{t_0}^{t} \mathbf{\Phi}(t, \tau)\mathbf{B}\mathbf{u}(\tau)d\tau = \int_{t_0}^{t} \mathbf{\Phi}(t, \tau)\mathbf{B}\mathbf{u}\delta(\tau)d\tau = \mathbf{\Phi}(t, t_0)\mathbf{B}\mathbf{u} = \mathbf{G}(t, t_0)\mathbf{u} \tag{2.37}$$

Thus, for impulsive maneuvers, the input matrix $\mathbf{G}(t, t_0)$ is readily available once the STM is known. If constant-thrust maneuvers are assumed, the time dependence

of $\mathbf{u}(t)$ vanishes and the term can be moved out of the integral:

$$\int_{t_0}^{t} \mathbf{\Phi}(t,\tau)\mathbf{B}\mathbf{u}(\tau)d\tau = \int_{t_0}^{t} \mathbf{\Phi}(t,\tau)\, d\tau\, \mathbf{B}\mathbf{u} = \mathbf{G}(t,t_0)\mathbf{u} \tag{2.38}$$

This time, however, the solution of the matrix $\mathbf{G}(t,t_0)$ requires the numerical integration of the above integral. This procedure is very cumbersome because of the presence of $\mathbf{\Phi}(t,\tau)$, which adds the computation of (2.35) at each time-step. To summarise:

$$\mathbf{G}(t,t_0) = \begin{cases} \mathbf{\Phi}(t,t_0)\mathbf{B} & \text{for} \quad \mathbf{u}(t) = \mathbf{u}\delta(t) \\ \int_{t_0}^{t} \mathbf{\Phi}(t,\tau)\, d\tau\mathbf{B} & \text{for} \quad \mathbf{u}(t) = \mathbf{u} \end{cases} \tag{2.39}$$

In both cases, the computation of $\mathbf{G}$ requires only knowledge of $\mathbf{\Phi}$, and so of the target dynamics. Once that is available, the discrete-time solution of the relative dynamics is given by:

$$\mathbf{x}(t_k) = \mathbf{\Phi}(t_k, t_{k-1})\mathbf{x}(t_{k-1}) + \mathbf{G}(t_k, t_{k-1})\mathbf{u} \tag{2.40}$$

From a GNC perspective, this result is very useful since it allows for the implementation of traditional guidance and control techniques to govern the chaser trajectory in proximity of the target. Additionally, the few studies [7] [12] [39] regarding in-orbit bearing only applications in LEO have been derived under the assumption that a discrete-time solution of the relative dynamics is available. Thus, this formulation allows the exploitation of the same approach in a completely different environment. Additionally, $\mathbf{\Phi}$ is also necessary for the propagation of the covariance in standard navigation filters.

However, from a computational standpoint, the exact evaluation of $\mathbf{\Phi}$ and $\mathbf{G}$ at each time step can be too burdensome as it requires the integration of 42 differential equations at each update time. As highlighted in [40], different truncated Taylor series can be used to approximate (2.35), with great advantages in terms of computational effort as only the knowledge of the Jacobian $\mathbf{A}(t)$ (and its derivative) is required. The three analysed methods are summarised in the table below.

	Description	Expression
1	1^{st}- order	$\mathbf{I} + \mathbf{A}_k\Delta t$
2	2^{nd}- order without $\dot{\mathbf{A}}_k$	$\mathbf{I} + \mathbf{A}_k\Delta t + \mathbf{A}_k^2\Delta t^2/2$
3	2^{nd}- order	$\mathbf{I} + \mathbf{A}_k\Delta t + (\mathbf{A}_k^2 + \dot{\mathbf{A}}_k)\Delta t^2/2$

TABLE 2.2: Approximation techniques for $\mathbf{\Phi}(t_k + \Delta t, t_k)$

Please notice that $\mathbf{A}_k$ is used to indicate the value of $\mathbf{A}(t)$ at time t_k. For the linearised relative CR3BP, the time-derivative of the Jacobian is easily obtained by deriving (2.29), as all the other terms in the matrix are constant. However, if a different dynamical model is employed, the time-derivative of $\mathbf{\Omega}$ has to be included. The analytical expression of $\dot{\mathbf{\Xi}}$ is:

$$\dot{\mathbf{\Xi}}(t) = 3\mathbf{\Lambda}(t) - 9\mathbf{\Gamma}(t) + 3\mathbf{\Psi}(t) \tag{2.41}$$

$$\begin{aligned}
\mathbf{\Lambda}(t) &= \left[\frac{c_1}{r_{T_1}^2}(\mathbf{v}_{T_1}\cdot\mathbf{r}_{T_1}) + \frac{c_2}{r_{T_1}^2}(\mathbf{v}_{T_2}\cdot\mathbf{r}_{T_2})\right]\mathbf{I}_3 \\
\mathbf{\Gamma}(t) &= \frac{c_1}{r_{T_1}^2}(\mathbf{v}_{T_1}\cdot\mathbf{r}_{T_1})\left[\hat{\mathbf{r}}_{T_1}\hat{\mathbf{r}}_{T_1}^T\right] + \frac{c_2}{r_{T_2}^2}(\mathbf{v}_{T_2}\cdot\mathbf{r}_{T_2})\left[\hat{\mathbf{r}}_{T_2}\hat{\mathbf{r}}_{T_2}^T\right] \\
\mathbf{\Psi}(t) &= c_1\left[\hat{\mathbf{r}}_{T_1}\frac{d\hat{\mathbf{r}}_{T_1}^T}{dt} + \frac{d\hat{\mathbf{r}}_{T_1}}{dt}\hat{\mathbf{r}}_{T_1}^T\right] + c_2\left[\hat{\mathbf{r}}_{T_2}\frac{d\hat{\mathbf{r}}_{T_2}^T}{dt} + \frac{d\hat{\mathbf{r}}_{T_2}}{dt}\hat{\mathbf{r}}_{T_2}^T\right]
\end{aligned} \tag{2.42}$$

where the two unknown coefficients are defined as:

$$c_1(t) = \frac{1-\mu}{r_{T_1}^3} \qquad c_2(t) = \frac{\mu}{r_{T_2}^3} \tag{2.43}$$

the derivative of the unit vector $\hat{\mathbf{r}}_{T_i}$ is:

$$\frac{d\hat{\mathbf{r}}_{T_i}}{dt} = \frac{\mathbf{v}_{T_i}}{r_{T_i}} - \frac{\mathbf{r}_{T_i}}{r_{T_i}^3}(\mathbf{r}_{T_i}\cdot\mathbf{v}_{T_i}) \tag{2.44}$$

and $\mathbf{v}_{T_1}$ and $\mathbf{v}_{T_2}$ are the relative velocities of the target with respect to the primaries. If $\dot{\mathbf{\Xi}}(t)$ is evaluated in the synodic frame, then $\mathbf{v}_{T_1} = \mathbf{v}_{T_2} = \mathbf{v}$ because the positions of the primaries are fixed. Finally, the time-derivative of $\mathbf{A}$ in the CR3BP is:

$$\dot{\mathbf{A}}(t) = \begin{bmatrix} \mathbf{0} & \mathbf{0} \\ \dot{\mathbf{\Xi}}(t) & \mathbf{0} \end{bmatrix} \tag{2.45}$$

From (2.45) one can see that the complete expression of the 2$^{\text{nd}}$- order Taylor expansion does not introduce any additional information on the components of $\mathbf{\Phi}$ related to the position. Thus, the only difference between the 2$^{\text{nd}}$ and 3$^{\text{rd}}$ methods in Table 2.2 is associated with the velocity. Figure 2.5 illustrates the times required by the different methods compared to the exact solution of (2.35). It immediately stands out that all three approximations require up to 3 order of magnitude less time than the exact solution. Furthermore, their timings hold irrespective of the propagation time-step, whereas the numerical integration displays a clear growing trend. As expected, out of the three expansions the last one always requires a slightly higher time because it has to evaluate both the Jacobian and its derivative.

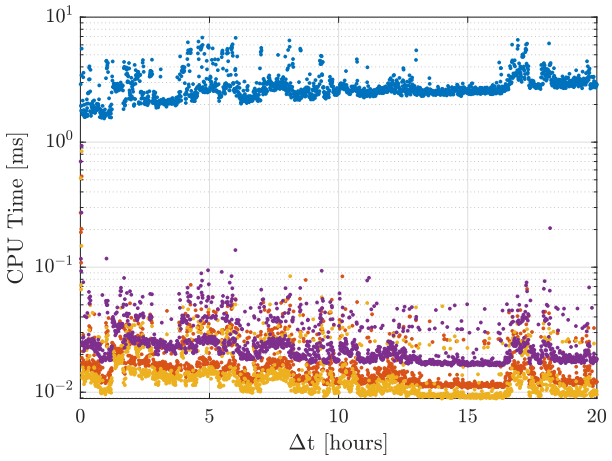

FIGURE 2.5: Comparison between different STM approximation techniques in terms of computational time. The blue dots are the timings required for the exact integration of Eq. (2.35), while the yellow, red and violet lines represent the 1$^{\text{st}}$, 2$^{\text{nd}}$ and 3$^{\text{rd}}$ methods of Table 2.2, respectively. Results obtained with an Intel i7-6700 and a RAM of 16 GB.

Figure 2.6, instead, reports the prediction accuracy, with the error defined as the

difference between the exact CR3BP non-linear relative dynamics and the various linear solutions. Notice that now, the numerical integration of the linear dynamics is also treated as an approximation. The performance of the truncated 2^{nd} - order are not reported because, as highlighted above, it has the same accuracy of the complete 2^{nd} - order for the position and of the 1^{st} - order in terms of velocities. The results are very encouraging because even after 20 hours, the position error is just slightly bigger than 1 km. Thus, both Taylor approximations are well-suited for on-board GNC applications as they allow a very good trade-off between modelling errors and computational effort.

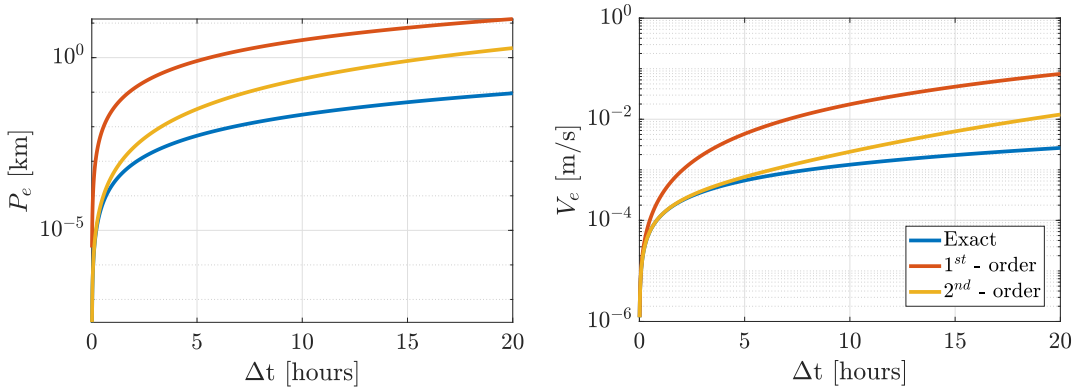

(*a*) Position error

(*b*) Velocity error

FIGURE 2.6: Prediction errors for different STM approximation techniques at the NRHO apolune The blue line identifies the exact numerical integration of the linearised dynamics.

As a final remark, these performance may vary depending on the relative initial conditions and on the location of the target around its orbit. For example, it has already been shown [23] that in the NRHOs perilune region the trend of the error gives acceptable results only for brief propagation times with respect to other points along the very same orbit. Indeed, the assumption of relative distance between the spacecraft much smaller than that between the target and the primaries is satisfied with a much higher tolerance at the apolune than the perilune. Thus, considering the typical relative distances of most rendezvous operations, it is reasonable to assume that the linearised model can be exploited by GNC algorithms in most of the cis-lunar space domain, except for the regions closest to the Moon.

Chapter 3

Sensors & Filtering Techniques

This chapter deals with the main techniques to estimate the states of a dynamic system when noisy measurements are available. In particular, when applied to in-orbit bearing-only solutions, the aim of the filter is to provide an estimate of the relative position and velocity of the chaser with respect to a target, given only the line-of-sight angles. For a generic dynamic linear system, the most common technique is the so-called Kalman Filter, an optimal linear estimator that mathematically provides the *best estimate* of the state variables. However, when speaking of bearing-only navigation, one has to deal with a non-linear measurement equation, thus the Kalman Filter must be slightly modified to account for non-linearities. In this regard, both the EKF and UKF are flight-proven technologies.

The chapter begins by illustrating the geometry of the measurement model, showing how it can be implemented to co-exist with a three-degrees-of-freedom formulation. A brief mention of real-world applications is made by discussing the effect that different camera properties have on measurement errors. Additionally, the range of relative distances where angles-only navigation is relevant is retrieved through simple mathematical and geometric considerations. Then, a detailed description of the filtering solutions exploited in this work is provided, together with their application to the non-keplerian dynamics. Finally, the last section deals with the techniques for the tuning of the state noise covariance matrix.

3.1 Observation Model

3.1.1 Pinhole Camera

In real applications, the measurements are obtained by applying image processing techniques to the data coming from the camera. These algorithms must be capable of recognising and locating the position of the target object, distinguishing it from other source of noise (e.g., the stars or other planetary bodies in the background). Some practical considerations regarding the bearing-only applicability range can be introduced by modelling the sensor as a simple pinhole camera [30]. It is based on the assumption that all the light rays travel through an infinitely small aperture at the centre and are projected onto the image plane of the camera. Since it does not rely on lenses to focus the light, distortion effects are neglected.

This simple approximation allows to narrow the set of suitable sensors that can be used to for a bearing-only application. For example, consider an object with characteristic length L_r at a distance R. Using as a reference Figure 3.1 and exploiting the rules of similar triangles, one can determine the minimum focal length f required to

identify the target with a given amount of pixels covered c_p:

$$\frac{L_r}{L_c} = \frac{R}{f} \qquad \longrightarrow \qquad f = \frac{Rc_p\rho_p}{L_r} \tag{3.1}$$

where L_c is the expected image size on the camera and ρ_p the pixel size in meters, such that: $L_c = c_p\rho_p$.

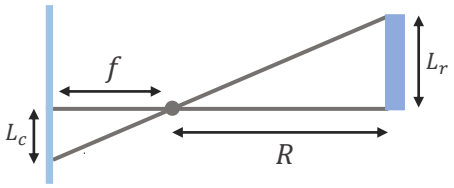

FIGURE 3.1: Pinhole Camera Model

Additionally, for a given array size W (i.e., the number of pixels in each direction), the Field-of-View (FOV), here denoted as θ, can be computed as follows:

$$\tan\left(\frac{\theta}{2}\right) = \frac{1}{2}\frac{W\rho_p}{f} \tag{3.2}$$

Substituting (3.1) inside (3.2) a relationship between θ and R is obtained:

$$\theta = 2\tan^{-1}\left(\frac{WL_r}{2Rc_p}\right) \tag{3.3}$$

Equations (3.1) and (3.3) respectively express the focal length and FOV required to distinguish an object as function of the relative distance between the target and the camera itself for a given pixel coverage. Figure 3.2 shows the behaviour of both parameters as function of the target distance. They illustrate the minimum and maximum values of f and θ, respectively required to identify the target with the given pixel coverage. For example, if the relative bearing-only navigation was to begin at an initial distance from the LOP-G of 600 km, the minimum focal length to guarantee a coverage of at least 4 pixels would be 0.27m. Any value lower than this would imply the target projection onto the camera plane is not big enough.

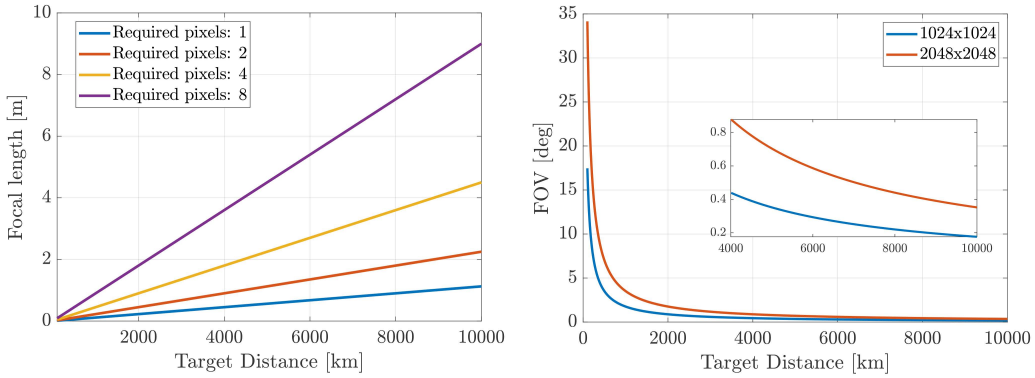

(*a*) Focal length

(*b*) Field of View (FOV)

FIGURE 3.2: Focal length and FOV required to identify a target at different distances. The maximum FOV has been computed assuming a 4 pixels coverage of the target. A dimension of 120 m was set for the target, mimicking the ISS size. A pixel size of 13.5μm is assumed.

For the same pixel coverage and distance, the right plot indicates the FOV should be no greater than 2.92° with a camera resolution of 1024 pixels. The same figure suggests that a Narrow Angle Camera (NAC) with a very small FOV should be used to identify the target when the distances are in the order of thousands of kilometers. Thus it is reasonable to expect that for a rendezvous with the LOP-G (or structures of similar sizes) the maximum relative distance to begin the bearing-only navigation is set in the order of thousands of km. However, to properly identify this range a more detailed analysis should be performed, taking into account the optical characteristics of the target, the illumination conditions and the performance of the image processing algorithms. As a last remark, these values strongly depends on the real size of the object. Indeed, for the same requirements of pixel coverage, camera resolution and initial distance mentioned previously, the minimum focal length increases to 0.8m, whereas the maximum FOV drops to 0.97°.

Whenever the apparent size of the target on the camera focal plane is greater than 1 pixel, it is theoretically possible to estimate the relative range by inverting (3.1), as long as the target size is known. This would provide 3 relative measurements (azimuth, elevation and distance) and greatly enhance the performance of the bearing-only navigation. Moreover, if this was possible, all the studies regarding maneuvers to enhance the state observability would be unjustified. Unfortunately, in a practical scenario, the presence of noisy pixels introduces range estimation errors far greater than those due to the inherent observability issues of the system. To prove this statement, a simple relation to compute the relative range error can be obtained manipulating (3.1). Define R and $\hat{R}$ the exact and estimated ranges, respectively. Then:

$$R = \frac{L_r f}{n\rho_p} \qquad \tilde{R} = \frac{L_r f}{(n+\sigma_p)\rho_p} \tag{3.4}$$

where n is the number of pixels associated to the real object and σ_p the amount of noisy pixels. Subtracting the expressions yields:

$$\delta\tilde{R} = \tilde{R} - R = \frac{L_r f}{\rho_p}\left(\frac{1}{n+\sigma_p} - \frac{1}{n}\right) = -\frac{L_r f}{\rho_p}\frac{\sigma_p}{n(n+\sigma_p)} \tag{3.5}$$

From (3.1) the real number of pixels n is inferred as:

$$n = \frac{L_r f}{R\rho_p} \tag{3.6}$$

By substituting (3.6) into (3.5), the value of the relative estimation error is re-written as:

$$\frac{\delta\tilde{R}}{R} = -\frac{R\rho_p\sigma_p}{L_r f + R\rho_p\sigma_p} \tag{3.7}$$

Finally, if the focal length is expressed in function of the distance D where a minimum pixel coverage of c_p is desired (through Eq. 3.1), the relative range error becomes:

$$\frac{\delta\tilde{R}}{R} = -\frac{R\sigma_p}{c_p D + R\sigma_p} \tag{3.8}$$

This equation allows to evaluate the relative range error that would be introduced if the apparent size of the target was used to estimate the relative distance. The error is function of the exact range R, the number of noisy pixels σ_p and the desired pixel coverage c_p at an arbitrary distance D. Notice that it holds irrespective of the target real size.

The behaviour of $\delta\tilde{R}/R$ is shown in Figure 3.3 and 3.4. The former suggests that to lower the relative range error, the distance where the angles-only navigation is set to begin should be maximised. Physically, when requesting the same pixel coverage at different distances, the FOV of the camera must decrease. Therefore, if the camera resolution is fixed, the angular size of each pixel reduces and the impact of noise effects is attenuated. Nevertheless, both figures clearly demonstrate that estimating the range from the apparent size of the target is unfeasible for a real application. Indeed, even for distances in the order of tenths of kilometers, it would introduce an error that is at least 5 or 10 times greater than that admissible for typical rendezvous operations.

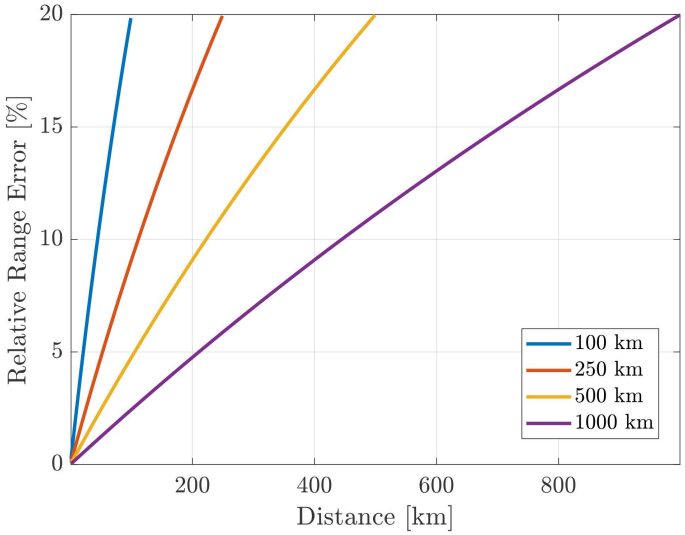

FIGURE 3.3: Variations of the relative range error as function of the distance for different initial conditions. The number of noisy pixel is set to 1 and the minimum coverage at the farthest distance is set to 4 pixel.

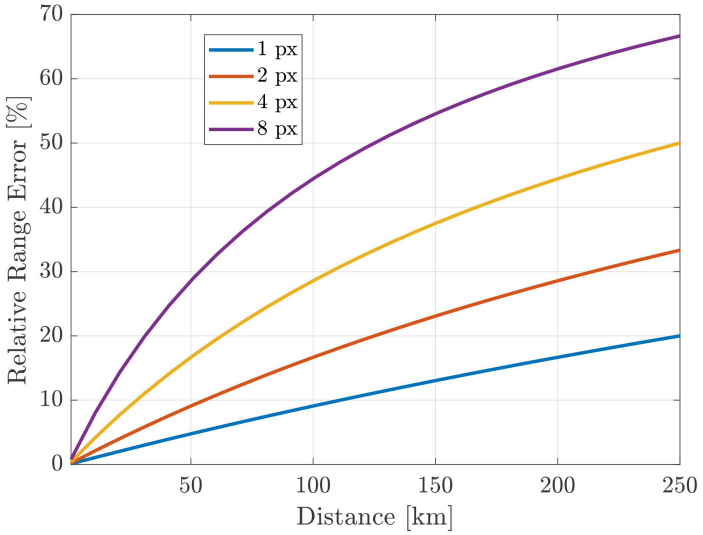

FIGURE 3.4: Variations of the relative range error for different noise conditions. A minimum 4 pixel coverage is required at 250 km.

3.1.2 Measurement Angles

Exploiting the rules of similar triangles, the three-dimensional position of the target ($\mathbf{X} = [X, Y, Z]^T$) can be mapped to the respective 2D coordinates in the camera plane $[u, v]$ as:

$$u = f\frac{X}{Z} \quad \text{and} \quad v = f\frac{Y}{Z} \tag{3.9}$$

Then, knowing the camera specifications (e.g., the FOV), these coordinates are transformed into the corresponding azimuth and elevation angles. However, these measurements are expressed in the sensor frame $\mathcal{I}_s$, thus they must be rotated to the frame used to propagate the dynamics inside the navigation filter. In this regard, additional errors are introduced inside the readings by the imperfect knowledge of the spacecraft attitude.

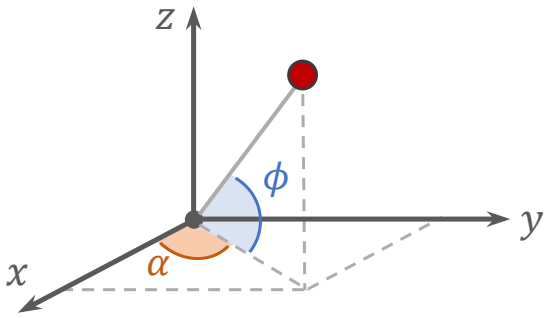

FIGURE 3.5: Measurement angles definition in the relative frame

Since the goal of this thesis is to evaluate the feasibility of bearing-only navigation for rendezvous operations in the cis-lunar domain, the measurement model is simplified and the angles are directly obtained from their definition:

$$\begin{bmatrix} \alpha \\ \phi \end{bmatrix} = \begin{bmatrix} \tan^{-1}(y/x) \\ \sin^{-1}(z/\sqrt{x^2+y^2+z^2}) \end{bmatrix} = \mathbf{h}(\mathbf{x}) \tag{3.10}$$

where α is the azimuth and ϕ the elevation angle. They are defined from -180° to 180° and from -90° to 90° respectively. Exploiting equation (3.10), one can easily adopt a simple point mass approximation for the spacecraft without the need of introducing the attitude dynamics. Whenever these angles are measured with a non-ideal sensor, the noise is assumed additive and is included as:

$$\begin{bmatrix} \tilde{\alpha} \\ \tilde{\phi} \end{bmatrix} = \begin{bmatrix} \alpha \\ \phi \end{bmatrix} + \begin{bmatrix} \delta\alpha \\ \delta\phi \end{bmatrix} = \tilde{\mathbf{h}}(\mathbf{x}, \mathbf{v}) = \mathbf{h}(\mathbf{x}) + \mathbf{v} \tag{3.11}$$

3.2 Non-linear Filters

The bearing-only navigation problem in the cis-lunar space is represented by the following non-linear model:

$$\begin{aligned} \dot{\mathbf{x}} &= \mathbf{g}(\mathbf{x}, \mathbf{x}_t, \mathbf{u}, t) \\ \mathbf{y} &= \mathbf{h}(\mathbf{x}) \end{aligned} \tag{3.12}$$

where $\mathbf{x}$ is the relative state vector, $\mathbf{x}_t$ the absolute state of the target, $\mathbf{g}$ describes the system dynamics, $\mathbf{u}$ is a control input and $\mathbf{y}$ is the output. As already underlined in the previous chapter, the contribution of $\mathbf{x}_t$ is necessary for the propagation

of the non-keplerian dynamics because the relative equations of motion cannot be simplified to a function of only the relative states. Additionally, in the most general scenario, time explicitly enters in the state equation because the ephemeris model is not autonomous. However, in a practical implementation, the exact dynamics of the system is unknown and different degrees of approximation are possible depending on the desired accuracy. Moreover, the measured angles will always be corrupted by some kind of noise, leading to an inherent uncertainty of the relative state.

Let us suppose that the system (3.12) can be approximated inside the navigation filter as:

$$\begin{aligned} \dot{\mathbf{x}}(t) &= \mathbf{A}(\mathbf{x}_t(t))\mathbf{x}(t) + \mathbf{B}\mathbf{u}(t) + \mathbf{B}\mathbf{w}(t) \\ \mathbf{y}(t) &= \tilde{\mathbf{h}}(\mathbf{x}(t),\, \mathbf{v}(t)) \end{aligned} \tag{3.13}$$

where the linear formulation of Eq. (2.32) is exploited to model the real dynamics. The terms $\mathbf{v}$ and $\mathbf{w}$ are the measurement and process noise and are used to account for random disturbances and modelling errors. In particular, in this work $\mathbf{w}$ is used to account for the un-modelled perturbing effects of both the SRP and the Sun's gravitational field. It is proven that its presence prevents the divergence of the filter estimates due to errors in the dynamical model. Additionally, both the EKF and UKF assume $\mathbf{w}(t)$ and $\mathbf{v}(t)$ to be Gaussian white noise processes such that [41]:

$$\begin{aligned} &E\left[\mathbf{v}(t)\right] = \mathbf{0} \quad \text{and} \quad E\left[\mathbf{w}(t)\right] = \mathbf{0} \\ &E[\mathbf{v}(t)\mathbf{v}^T(\tau)] = \mathbf{R}(t)\delta(t-\tau) \\ &E[\mathbf{w}(t)\mathbf{w}^T(\tau)] = \mathbf{Q}(t)\delta(t-\tau) \end{aligned} \tag{3.14}$$

where E is the expected value operator, $\mathbf{Q}(t)$ is the power spectral density of $\mathbf{w}$ and $\mathbf{R}(t)$ is the *measurement noise covariance* matrix. The discrete time solution for the system in (3.13) would be:

$$\begin{aligned} \mathbf{x}_k &= \mathbf{f}_k(\mathbf{x}_{k-1},\, \mathbf{x}_{t_{k-1}},\, \mathbf{u}_{k-1},\, \mathbf{w}_{k-1}) \\ \mathbf{y}_k &= \tilde{\mathbf{h}}(\mathbf{x}_k,\, \mathbf{v}_k) \end{aligned} \tag{3.15}$$

It is clear however, that this form of propagation would require the integration of the state equations at each update time to obtain $\mathbf{x}_k$. Moreover, one would need to simultaneously integrate the relative state dynamics with the absolute dynamics of the target due to their coupling via the Jacobian $\mathbf{A}$. On the other hand, in section 2.5.2 it was shown that a suitable expansion of the STM is well capable of approximating the results coming from the numerical integration. In particular, Figure 2.6 indicates that for typical filter update times (e.g. 1 Hz), the errors introduced by the approximation are completely negligible. Thus, to ease the computational burden, the following discrete-time model is employed to simulate the real-world dynamics in the navigation filter:

$$\begin{aligned} \mathbf{x}_k &= \mathbf{\Phi}_{k-1}\mathbf{x}_{k-1} + \mathbf{G}_{k-1}\mathbf{u}_{k-1} + \mathbf{G}_{k-1}\mathbf{w}_{k-1} \\ \mathbf{y}_k &= \tilde{\mathbf{h}}(\mathbf{x}_k,\, \mathbf{v}_k) \end{aligned} \tag{3.16}$$

where $\mathbf{\Phi}_{k-1}$ is evaluated with one of the relationships in Table 2.2 and $\mathbf{G}_{k-1}$ exploits the equations in (2.39). However, since both matrices depend on $\mathbf{x}_{t_{k-1}}$, at each time step k the navigation filter requires information on the absolute state of the target to work properly. Notice that for non-impulsive maneuvers, the solution of $\mathbf{G}_{k-1}$ requires the integration of the whole dynamics nonetheless. A suitable work-around

could then be found by exploiting Simpson's rules or similar techniques to approximate definite integrals. If that is the case, the different values of $\mathbf{\Phi}$ are straightforwardly obtained by changing the propagation time Δt. As a last remark, system (3.16) holds true for both the CR3BP and the EpR3BP as the only difference relies in the definition of the target position with respect to the primaries.

Although the state equation in (3.16) is linear, the outputs of the systems are still non-linear function of the relative states, thus a non-linear filter is required anyway.

3.2.1 Extended Kalman Filter

The EKF is an extension of the Kalman Filter to non linear models. It relies on the linearisation of the KF equations with respect to the state estimate at each time-step. The whole estimation procedure can be divided into two subsequent stages, the prediction and the correction steps, respectively. The former is computed as:

$$\begin{aligned} \hat{\mathbf{x}}_k^- &= \mathbf{\Phi}_{k-1}\hat{\mathbf{x}}_{k-1}^+ + \mathbf{G}_{k-1}\mathbf{u}_{k-1} \\ \mathbf{P}_k^- &= \mathbf{\Phi}_{k-1}\mathbf{P}_{k-1}^+\mathbf{\Phi}_{k-1}^T + \mathbf{S}_{k-1} \end{aligned} \tag{3.17}$$

Instead, the correction stage takes the form of:

$$\begin{aligned} \mathbf{z}_k &= \mathbf{y}_k - \mathbf{h}(\hat{\mathbf{x}}_k^-) \\ \mathbf{K}_k &= \mathbf{P}_k^-\mathbf{H}_k^T(\mathbf{H}_k\mathbf{P}_k^-\mathbf{H}_k^T + \mathbf{R}_k)^{-1} \\ \hat{\mathbf{x}}_k^+ &= \hat{\mathbf{x}}_k^- + \mathbf{K}_k\mathbf{z}_k \\ \mathbf{P}_k^+ &= (\mathbf{I} - \mathbf{K}_k\mathbf{H}_k)\mathbf{P}_k^-(\mathbf{I} - \mathbf{K}_k\mathbf{H}_k)^T + \mathbf{K}_k\mathbf{R}_k\mathbf{K}_k^T \end{aligned} \tag{3.18}$$

where $\mathbf{K}_k$ is the Kalman gain, $\mathbf{y}_k$ are the sensor measurements and $\mathbf{S}_{k-1}$ is the *state process covariance* matrix. $\mathbf{H}_k$ is the linearised measurement function, evaluated at the predicted state $\hat{\mathbf{x}}_k^-$ and equals:

$$\mathbf{H}_k = \frac{\partial \mathbf{h}}{\partial \mathbf{x}}\Big|_{\hat{\mathbf{x}}_k^-} = \begin{bmatrix} -\dfrac{y}{x^2+y^2} & \dfrac{x}{y^2+x^2} & 0 & 0 & 0 & 0 \\ -\dfrac{zx}{r^2\sqrt{x^2+y^2}} & -\dfrac{xy}{r^2\sqrt{x^2+y^2}} & \dfrac{\sqrt{x^2+y^2}}{r^2} & 0 & 0 & 0 \end{bmatrix}\Bigg|_{\hat{\mathbf{x}}_k^-} \tag{3.19}$$

with $r = \sqrt{x^2+y^2+z^2}$. Notice that the covariance update in the correction step is the so-called *Joseph's Formula*, a more robust version of the original update equation that guarantees the covariance matrix $\mathbf{P}_k^+$ remains positive definite. From the definition of $\mathbf{w}$, the process covariance $\mathbf{S}$ can be expressed as:

$$\mathbf{S}_k = \int_{t_{k-1}}^{t_k} \mathbf{\Phi}(t_k,\tau)\mathbf{B}\mathbf{Q}(\tau)\mathbf{B}^T\mathbf{\Phi}^T(t_k,\tau)d\tau \tag{3.20}$$

In practice, to simplify the computation an approximate value of $\mathbf{S}_k$ is exploited; computed according to the methods explained in Section 3.3.

One common problem when dealing with azimuth measurements is called the *azimuth mutation*. It happens when the chaser crosses the negative side of the x-axis, leading to a sudden change of the azimuth readings from π to -π or viceversa. As a consequence, the estimation error drastically increases and the filter diverges. To prevent the issue, a modified measurement method has been proposed [42], where

the azimuth sine and cosine replace the original data. However, the resulting formulation leads to a non-additive measurement noise, in contrast with the original assumptions of the EKF. The reasons behind the divergence are due to the unusual large values of the innovation $\mathbf{z}_k$ when the filter predicts the chaser to be on one side of the x-axis and the measurements say otherwise. Thus, a simple approach is here applied to ensure that $\mathbf{z}_k$ always remains bounded, that is:

$$z_{\alpha_k} = z_{\alpha_k} \pm 2\pi \quad \text{while} \quad |z_{\alpha_k}| > c \tag{3.21}$$

where z_{α_k} refers to the azimuth component of the innovation vector and c is an arbitrary design threshold (a value of $5/6\pi$ has proven to work). Note that if the measurement function was based on the pixels coordinates in (3.9), the rotation to the chaser frame would prevent this issue from happening.

One of the major drawbacks of the EKF is that it can generate unreliable results when applied to highly non-linear systems, such as bearing-only problems. Another source of issue is that the Jacobian $\mathbf{H}$ should be computed at the true state of the system and, as this is not possible, the usage of the predicted states further increases the estimation errors.

3.2.2 Unscented Kalman Filter

In the last decades, several alternatives have been proposed to address the EKF drawbacks; one of the most common is the UKF. As the name suggests, it is based on the *unscented transformation*, a method to compute the statistics of a random variable subject to a nonlinear transformation [43]. This is performed by generating a set of $2n+1$ sigma points $\boldsymbol{\mathcal{X}}^i_{k-1}$ as follows:

$$\begin{aligned}
\boldsymbol{\mathcal{X}}^0_{k-1} &= \hat{\mathbf{x}}_{k-1} & W_i &= \frac{\kappa}{n+\kappa} & i &= 0 \\
\boldsymbol{\mathcal{X}}^i_{k-1} &= \hat{\mathbf{x}}_{k-1} + \left(\sqrt{(n+\kappa)\mathbf{P}^+_{k-1}}\right)_i & W_i &= \frac{\kappa}{2(n+\kappa)} & i &= 1,...,n \\
\boldsymbol{\mathcal{X}}^i_{k-1} &= \hat{\mathbf{x}}_{k-1} - \left(\sqrt{(n+\kappa)\mathbf{P}^+_{k-1}}\right)_i & W_i &= \frac{\kappa}{2(n+\kappa)} & i &= n+1,...,2n
\end{aligned} \tag{3.22}$$

where $\left(\sqrt{(n+\kappa)\mathbf{P}^+_{k-1}}\right)_i$ is the i-th column of the matrix square root $\mathbf{L}$ such that:

$$(n+\kappa)\mathbf{P}^+_{k-1} = \mathbf{L}\mathbf{L}^T \tag{3.23}$$

W_i is the weight associated to the i-th point, κ is a scaling parameter and n is the number of estimated states (see [44] for further details). Some formulations assign to W_0 two slightly different values for the estimates of the mean and of the covariance. Nevertheless, the performance of the two alternatives are identical. Representing with $\mathcal{U}(\hat{\mathbf{x}}_{k-1},\ \mathbf{P}_{k-1})$ the unscented transformation in Eq. 3.22, the UKF prediction step is written as:

$$\begin{aligned}
\boldsymbol{\mathcal{X}}^i_{k-1} &= \mathcal{U}(\hat{\mathbf{x}}^+_{k-1}, \mathbf{P}^+_{k-1}) \\
\boldsymbol{\mathcal{X}}^i_{k|k-1} &= \boldsymbol{\Phi}_{k-1}\boldsymbol{\mathcal{X}}^i_{k-1} + \mathbf{G}_{k-1}\mathbf{u}_{k-1} \\
\hat{\mathbf{x}}^-_k &= \sum_{i=0}^{2n} W_i \boldsymbol{\mathcal{X}}^i_{k|k-1} \\
\mathbf{P}^-_k &= \sum_{i=0}^{2n} W_i \left(\boldsymbol{\mathcal{X}}^i_{k|k-1} - \hat{\mathbf{x}}^-_k\right)\left(\boldsymbol{\mathcal{X}}^i_{k|k-1} - \hat{\mathbf{x}}^-_k\right)^T + \mathbf{S}_{k-1}
\end{aligned} \tag{3.24}$$

For the correction stage, the general version of the UKF would require a new generation of sigma points with mean $\hat{\mathbf{x}}_k^-$ and covariance $\mathbf{P}_k^-$. However, under the assumption of additive process and measurement noise, the previously propagated points $\boldsymbol{\mathcal{X}}_{k|k-1}^i$ can be exploited for the next step. The measurement update equations are then expressed as:

$$\begin{aligned}
\boldsymbol{\mathcal{Y}}_{k|k-1}^i &= \mathbf{h}(\boldsymbol{\mathcal{X}}_{k|k-1}^i) \\
\hat{\mathbf{y}}_k^- &= \sum_{i=0}^{2n} W_i \boldsymbol{\mathcal{Y}}_{k|k-1}^i \\
\mathbf{z}_k &= \mathbf{y}_k - \hat{\mathbf{y}}_k^- \\
\mathbf{P}_{yy_k} &= \sum_{i=0}^{2n} W_i \left(\boldsymbol{\mathcal{Y}}_{k|k-1}^i - \hat{\mathbf{y}}_k^-\right)\left(\boldsymbol{\mathcal{Y}}_{k|k-1}^i - \hat{\mathbf{y}}_k^-\right)^T + \mathbf{R}_k \\
\mathbf{P}_{xy_k} &= \sum_{i=0}^{2n} W_i \left(\boldsymbol{\mathcal{X}}_{k|k-1}^i - \hat{\mathbf{x}}_k^-\right)\left(\boldsymbol{\mathcal{Y}}_{k|k-1}^i - \hat{\mathbf{y}}_k^-\right)^T \\
\boldsymbol{\mathcal{K}}_k &= \mathbf{P}_{xy_k}\mathbf{P}_{yy_k}^{-1} \\
\hat{\mathbf{x}}_k^+ &= \hat{\mathbf{x}}_k^- + \boldsymbol{\mathcal{K}}_k \mathbf{z}_k \\
\mathbf{P}_k^+ &= \mathbf{P}_k^- - \boldsymbol{\mathcal{K}}_k \mathbf{P}_{yy_k}\mathbf{K}^T
\end{aligned} \tag{3.25}$$

To prevent the azimuth mutation when $\mathbf{z}_k$ is computed, its value is bounded with (3.21). The clear advantage with respect to the EKF is that the computation of Jacobians is not required. Additionally, the unscented transformation is capable of partially capturing some discontinuities of the non-linear function $\mathbf{h}$. The major drawback is that the computation of the sigma points is computationally expensive. For this reason, an alternative and more efficient version has been proposed. It is called the Square-Root UKF and exploits the propagation of the matrix square-root of the state covariance matrix [45].

3.3 Process Noise Covariance

The tuning of the process covariance $\mathbf{S}_k$ is always a cumbersome procedure because it relies on the designer's ability to select proper values for the approximation errors of the dynamic model. Moreover, the tuning in some peculiar environments, such as the cis-lunar space, has proven particularly challenging because of the strong non-linearities of the real dynamics. The inclusion of additional time-varying perturbing effects (e.g., the SRP) further increased the complexity of the task at hand. For these scenarios a more reliable and intuitive approach is desirable.

As stated previously, the EKF and UKF assume the state noise $\mathbf{w}(t)$ to be a white noise process, leading to the following expression for the process noise covariance (here reported from 3.20):

$$\mathbf{S}_k = \int_{t_{k-1}}^{t_k} \boldsymbol{\Phi}(t_k, \tau)\mathbf{B}\mathbf{Q}(\tau)\mathbf{B}^T\boldsymbol{\Phi}^T(t_k, \tau)d\tau \tag{3.26}$$

This equation does not allow a straightforward and fast numerical implementation, therefore two approximations have been proposed by [41]. They are respectively called the *State Noise Compensation* (SNC) and the *Dynamic Model Compensation* (DMC). A brief description of both is given in the following paragraphs.

3.3.1 State Noise Compensation

Given the original dynamic model:

$$\dot{\mathbf{x}}(t) = \mathbf{A}(\mathbf{x}_t(t))\mathbf{x}(t) + \mathbf{B}\mathbf{u}(t) + \mathbf{B}\mathbf{w}(t) \tag{3.27}$$

In the SNC, the unmodelled accelerations $\mathbf{w}(t)$ are assumed to be uncorrelated random walks with a fixed intensity. It is further supposed they can be described by a spectral density $\mathbf{Q}$ in the form of:

$$\mathbf{Q}(t) = \begin{bmatrix} q_x & 0 & 0 \\ 0 & q_y & 0 \\ 0 & 0 & q_z \end{bmatrix} \simeq \sigma_w^2 \mathbf{I}_3 \tag{3.28}$$

Please note that for the future derivation of $\mathbf{S}$, the matrix $\mathbf{Q}$ is not required to be diagonal nor to have equal elements. However, this approximation is quite useful for a first rough tuning of σ_w. Indeed, the greater the number of independent elements in $\mathbf{Q}$ and the harder/burdensome it is to properly tune them. Thus, an easier way to approach the problem is to exploit a single parameter to reduce the tuning space. Then, the elements can be diversified to increase the accuracy of the estimation.

The final expression of $\mathbf{S}_k$ is obtained by assuming that the update time is small enough for $\mathbf{\Phi}$ to be approximated by a 1^{st}-order expansion. Under these hypothesis the integral in (3.20) is written as:

$$\mathbf{S}_k = \begin{bmatrix} \mathbf{Q}_k \dfrac{\Delta t^3}{3} & \mathbf{Q}_k \dfrac{\Delta t^2}{2} \\ \mathbf{Q}_k \dfrac{\Delta t^2}{2} & \mathbf{Q}_k \Delta t \end{bmatrix} \tag{3.29}$$

This value of $\mathbf{S}_k$ holds as long as the update time is constant, whenever that is not the case, the matrix must be properly adjusted. The major drawback of this approach relies in the assumption that $\mathbf{w}(t)$ is a white noise process, since in practical applications all unmodelled accelerations are correlated in time.

3.3.2 Dynamic Model Compensation

The drawbacks of the SNC are compensated in the DMC by modelling the dynamic errors, here called $\boldsymbol{\eta}$, as a time-correlated first-order Gauss-Markov process. The time evolution of these biases would then satisfy the following differential equation:

$$\dot{\boldsymbol{\eta}}(t) = -\boldsymbol{\beta}\boldsymbol{\eta}(t) + \mathbf{w}(t) \tag{3.30}$$

This expression yields a process noise that includes a deterministic contribution as well as a random term. To account for (3.30), the state vector is augmented with the values of $\boldsymbol{\eta}$. Note that some alternative versions of Eq. (3.30) exists, such that the time-correlation coefficients $\boldsymbol{\beta}$ change with time. However, the resulting model would require an additional extension of the state vector dimensions (up to 12 components), thus they are here neglected.

The state transition matrix of the newly augmented system $\mathbf{\Phi}^a$ can be written as:

$$\mathbf{\Phi}^a_{k-1} = \begin{bmatrix} \mathbf{\Phi}_{pp} & \mathbf{\Phi}_{pv} & \boldsymbol{\eta}_p \\ \mathbf{\Phi}_{vp} & \mathbf{\Phi}_{vv} & \boldsymbol{\eta}_v \\ \mathbf{0} & \mathbf{0} & \boldsymbol{\eta}_\eta \end{bmatrix} \tag{3.31}$$

By assuming that the three components of $\boldsymbol{\eta}$ are uncorrelated, the matrices in the third column become diagonal and their generic i-th element is expressed as:

$$\begin{aligned} \eta_{p_i} &= \frac{\Delta t}{\beta_i} + \frac{1}{\beta_i^2}\left(e^{-\beta_i \Delta t} - 1\right) \\ \eta_{v_i} &= \frac{1}{\beta_i}\left(1 - e^{-\beta_i \Delta t}\right) \\ \eta_{\eta_i} &= e^{-\beta_i \Delta t} \end{aligned} \tag{3.32}$$

Finally the process noise covariance is:

$$\mathbf{S}_k = \begin{bmatrix} \gamma_{pp}\mathbf{Q} & \gamma_{pv}\mathbf{Q} & \gamma_{p\eta}\mathbf{Q} \\ \gamma_{pv}\mathbf{Q} & \gamma_{vv}\mathbf{Q} & \gamma_{v\eta}\mathbf{Q} \\ \gamma_{p\eta}\mathbf{Q} & \gamma_{v\eta}\mathbf{Q} & \gamma_{\eta\eta}\mathbf{Q} \end{bmatrix} \tag{3.33}$$

where $\mathbf{Q}$ has the same form of (3.28). The matrices γ are all diagonal with the i-th element equal to:

$$\begin{aligned} \gamma_{pp_i} &= \frac{\Delta t^3}{3\beta_i^2} - \frac{\Delta t^2}{\beta_i^3} + \frac{\Delta t}{\beta_i^4}\left(1 - 2e^{-\beta_i \Delta t}\right) + \frac{1}{2\beta_i^5}\left(1 - e^{-2\beta_i \Delta t}\right) \\ \gamma_{pv_i} &= \frac{\Delta t^2}{2\beta_i^2} - \frac{\Delta t}{\beta_i^3}\left(1 - e^{-\beta_i \Delta t}\right) + \frac{1}{\beta_i^4}\left(1 - e^{-\beta_i \Delta t}\right) - \frac{1}{2\beta_i^4}\left(1 - e^{-2\beta_i \Delta t}\right) \\ \gamma_{p\eta_i} &= \frac{1}{2\beta_i^3}\left(1 - e^{-\beta_i \Delta t}\right) - \frac{\Delta t}{\beta_i^2} e^{-\beta_i \Delta t} \\ \gamma_{vv_i} &= \frac{\Delta t}{\beta_i^2} - \frac{2}{\beta_i^3}\left(1 - e^{-\beta_i \Delta t}\right) + \frac{1}{2\beta_i^3}\left(1 - e^{-2\beta_i \Delta t}\right) \\ \gamma_{v\eta_i} &= \frac{1}{2\beta_i^2}\left(1 + e^{-2\beta_i \Delta t}\right) - \frac{1}{\beta_i^2} e^{-\beta_i \Delta t} \\ \gamma_{\eta\eta_i} &= \frac{1}{2\beta_i}\left(1 - e^{-2\beta_i \Delta t}\right) \end{aligned} \tag{3.34}$$

Besides achieving a higher estimation accuracy, the DMC model is less sensitive to tuning. That is, it achieves good performance over a broader range of σ_w when compared to the SNC. Nevertheless, also in this case, a good assumption to start the tuning process is to exploit identical values for the elements of $\boldsymbol{\beta}$ as well as of $\mathbf{Q}$.

As a last remark, please notice that the expressions for the coefficients of $\mathbf{S}_k$ have been obtained by evaluating the integral in (3.26) with a first-order expansion of the STM that is different from the one reported in (3.31). In particular, the the top-left portion was set equal to the product between the identity matrix ($\mathbf{I}_6$) and the time-step. Nevertheless, the usage of (3.31) for the prediction stage has proven more effective when applied to the non-keplerian space. This method will be adopted for all the numerical simulations of this work.

Chapter 4

Observability Analysis

This chapter begins by tackling the bearing-only observability dilemma from different perspectives. Geometric considerations are first employed to introduce the problem and are followed by a mathematical description to rigorously derive the observability and unobservability criteria. Then, a continuous "measure" of observability is suggested to develop a closed-form analytical solution for the maneuvers that provide the best improvement in the navigation process. The effectiveness of these maneuvers to provide an optimal solution is discussed and the results on the Keplerian and non-Keplerian regimes are shown.

As mentioned in the introduction, bearing-only navigation is the problem of determining the relative position and velocity of a chaser with respect to a target by measuring only the line-of-sight angles (i.e, azimuth and elevation). The inherent simplicity of this approach makes it a very appealing technology to replace the costly and power demanding traditional navigation methods for rendezvous. Nevertheless, bearings-only navigation suffers from the limitation in determining the range to the target.

Recent studies in LEO orbits have shown that the observability gap can be overcome by performing specific sets of maneuvers to alter the trajectory of the spacecraft with respect to its original natural evolution. However, to the author's knowledge, the bearing-only navigation has been very little studied for rendezvous applications in non-keplerian regimes. Therefore, this chapter is completely dedicated on assessing the applicability of LEO bearing-only solutions to perform proximity operations in the cis-lunar domain.

Since all the existing analyses adopt as a baseline the Closhessy-Wiltshire (CW) model, the linearised relative dynamics presented in section 2.5.1 is here exploited to mimic a similar approach. Additionally, throughout the chapter, the results coming from the linear formulation are constantly compared with the real non-linear dynamics to highlight potential differences and, where possible, exploit their benefits.

4.1 Observability and Unobservability Criteria

Under the assumption that the non-keplerian relative dynamics can be approximated with a linear model, the bearing-only navigation problem can be described by the following system:

$$\begin{aligned} \dot{\mathbf{x}}(t) &= \mathbf{A}(t)\mathbf{x}(t) + \mathbf{B}\mathbf{u}(t) \qquad \text{with} \quad \mathbf{x}(t_0) = \mathbf{x}_1 \\ \mathbf{y}(t) &= \mathbf{h}(\mathbf{x}(t)) \end{aligned} \tag{4.1}$$

characterised by linear state equations and a non-linear measurement function $\mathbf{h}(\mathbf{x})$, with $\mathbf{x} \in \mathbb{R}^6$ and $\mathbf{y} \in \mathbb{R}^2$. The initial point $\mathbf{x}_1$ is unknown and belongs to a set Ω of admissible initial conditions.

The system (4.1) is said to be *completely observable* in Ω in the time interval $[t_1, t_k]$ if there exist a one-to-one correspondence between the set of initial states Ω and the set of measurements described by the output $\mathbf{y}(t)$ in $[t_1, t_k]$. In other words, given $\mathbf{x}_1 \in \Omega$, the system is completely observable if there does not exist another $\mathbf{x}_2 \in \Omega$, such that the set of measurements $\mathbf{h}(\mathbf{x}(\mathbf{x}_1, t)) = \mathbf{h}(\mathbf{x}(\mathbf{x}_2, t))$ in $[t_1, t_k]$ [46]. In this regard, it is important to distinguish a single measurement from the whole measurement profile. The former is associated with a single sensor reading, whereas the latter is the ensemble of all the different measurements over an arbitrary observation interval. From the previous definition it is then clear that global observability in Ω is granted only if the initial point can be uniquely determined on the basis of its measurement profile. According to the previous notation, this means that at least one measurement generated by $\mathbf{x}_1$ must be different from the readings of $\mathbf{x}_2$.

For a generic linear system, a simple criteria for global observability exists and is based on evaluating the rank of the observability matrix. Unfortunately, in our case the measurements are associated with the azimuth and elevation angles, meaning that the outputs are inherently non-linear functions of the states. With this in mind, many authors have proposed a polar or spherical coordinate parametrization of the relative dynamics when dealing with bearing-only applications. For example [18] developed a spherical model starting from CW's equation of relative dynamics, decoupling the observable and unobservable states and effectively improving the accuracy of the navigation filter. However, despite in such formulation the measurement function is linear, the state-dynamics is expressed as a non-linear function of the new coordinates, thus a non-linear approach to establish observability is required nonetheless.

Classical non-linear techniques rely on Lie derivatives to derive the sufficient and necessary conditions for the global observability of non-linear systems. These criteria are based on the construction of a non-linear observability map, obtained by iteratively deriving the measurement function in time (see [8] [46] for a detailed explanation). Such approach has proven beneficial in the frame of ground and naval applications, where the relative dynamics is somewhat written in a simple form [2]. Yet, the non-keplerian space (and in a greater perspective, the whole space domain) is a much more complex scenario, one for which a more straightforward proof of observability is desirable.

Recent studies have already established the observability criteria for in-orbit bearing-only navigation. In particular [39] has exploited a geometric interpretation of the problem to analyse the observability of specific scenarios. On the other hand, [7] used an analytical approach to derive the observability conditions in a linear framework. In addition, it also adopted the very same criteria to find the set of maneuvers that, if executed, do not provide observability. On the basis of these works, this section shows that the results of these formulations are also valid in a completely different dynamical environment. Additionally, the effects of un-modelled non-linear gravitational terms to produce observability are quantified and analysed from a practical viewpoint.

4.1.1 Geometric Interpretation

To gain a physical perspective on the problem, it is useful to establish a link between the system dynamics (i.e., the spacecraft trajectory) and the outputs. In doing so, the Line-of-Sight (LOS) unit vector $\boldsymbol{\iota}_r(t)$ can be written in terms of the angle measurements as:

$$\boldsymbol{\iota}_r(t) = \begin{bmatrix} \cos\alpha(t)\cos\phi(t) \\ \cos\alpha(t)\sin\phi(t) \\ \sin\alpha(t) \end{bmatrix} = \frac{\mathbf{r}(t)}{\|\mathbf{r}(t)\|} \tag{4.2}$$

where α, ϕ are respectively the azimuth and elevation angles and $\mathbf{x}_r$ is the relative position vector. Defining $\boldsymbol{\Lambda}$ the positions-related portions of the state transition matrix in (2.40), such that $\boldsymbol{\Lambda} = [\boldsymbol{\Phi}_{rr} \;\; \boldsymbol{\Phi}_{rv}]$ and assuming a null input vector $\mathbf{u}$, the LOS measurements can be recast as function of the initial conditions $\mathbf{x}_1$ as:

$$\bar{\boldsymbol{\iota}}_r(t) = \frac{\boldsymbol{\Lambda}\mathbf{x}_1}{\|\boldsymbol{\Lambda}\mathbf{x}_1\|} \tag{4.3}$$

where $\boldsymbol{\Lambda}$ is always evaluated from t_1 to t. The bar over $\bar{\boldsymbol{\iota}}_r(t)$ is used to underline that these angle measurements are associated with the natural dynamics. According to the previous definition, in order for $\mathbf{x}_1$ to be observable, the collection of all $\bar{\boldsymbol{\iota}}_r(t)$ over every $t \in [t_1, t_k]$ must be unique. However, it is easy to notice that the same LOS profile is obtained by scaling the initial conditions $\mathbf{x}_1$ by any arbitrary factor $\beta > 0$ [39]:

$$\frac{\boldsymbol{\Lambda}(\beta\mathbf{x}_1)}{\|\boldsymbol{\Lambda}(\beta\mathbf{x}_1)\|} = \frac{\beta}{|\beta|}\frac{\boldsymbol{\Lambda}\mathbf{x}_1}{\|\boldsymbol{\Lambda}\mathbf{x}_1\|} = \mathrm{sgn}(\beta)\frac{\boldsymbol{\Lambda}\mathbf{x}_1}{\|\boldsymbol{\Lambda}\mathbf{x}_1\|} \tag{4.4}$$

If $\beta < 0$, the resulting measurement profile is opposite to the original one, making $\mathbf{x}_1$ observable. Therefore, if the exact dynamics were represented by a linear model and no maneuvers were performed, the system would be unobservable for any given initial condition, as there exist infinite $\mathbf{x}_2 = \beta\mathbf{x}_1$ such that the measurement profile generated by $\mathbf{x}_1$ is indistinguishable. This issue is visually illustrated in Figure 4.1.

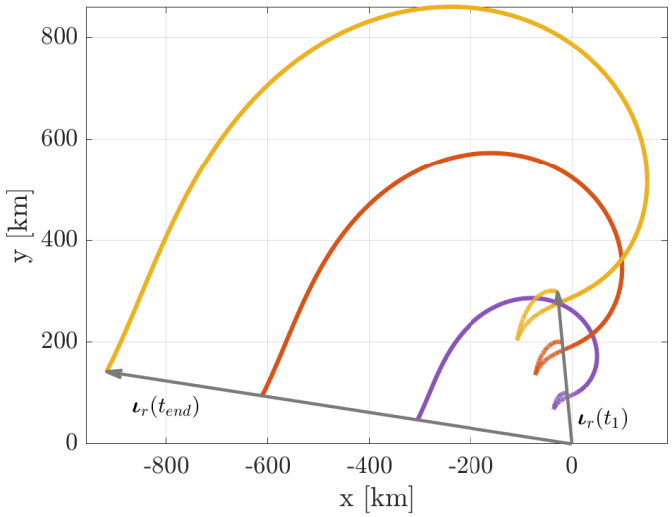

FIGURE 4.1: Ensemble of unobservable line-of-sight profiles

Figure 4.1 displays the evolution of the linearised relative dynamics around a target

on a Lyapunov orbit, with the chaser located in the unstable manifold, for three different values of β. The LOS vectors at the beginning and end of the time-window are used to highlight that the measurement profiles are equal. [6] effectively proves that the only parameter that cannot be distinguished from identical angle measurements is the range between the two spacecraft (i.e., the scaling parameter β). Despite this, observability is gained when the chaser is maneuvered in appropriate directions that allow to determine the unknown range.

When a generic maneuver profile $\mathbf{u}(t)$ is performed, the new LOS vector at time t_k is obtained from (2.33):

$$\boldsymbol{\iota}_r(t_k) = \frac{\boldsymbol{\Lambda}_k \mathbf{x}_1 + \int_{t_1}^{t_k} \boldsymbol{\Lambda}(t_k,\tau)\mathbf{B}\mathbf{u}(\tau)d\tau}{\|\boldsymbol{\Lambda}_k \mathbf{x}_1 + \int_{t_1}^{t_k} \boldsymbol{\Lambda}(t_k,\tau)\mathbf{B}\mathbf{u}(\tau)d\tau\|} = \frac{\bar{\mathbf{r}}(t_k) + \delta\mathbf{r}(t_k)}{\|\bar{\mathbf{r}}(t_k) + \delta\mathbf{r}(t_k)\|} \tag{4.5}$$

where $\bar{\mathbf{r}}$ represents the nominal trajectory profile and $\delta\mathbf{r}(t_k)$ is associated with the displacements due to the cumulative effects of $\mathbf{u}(t)$ over the interval $[t_1, t_k]$. Recalling the structure of $\mathbf{B}$ from (2.28), the convolution integral can be simplified to:

$$\delta\mathbf{r}(t) = \int_{t_1}^{t_k} \boldsymbol{\Lambda}(t_k,\tau)\mathbf{B}\mathbf{u}(\tau)d\tau = \int_{t_1}^{t_k} \boldsymbol{\Phi}_{rv}(t_k,\tau)\mathbf{u}(\tau)d\tau \tag{4.6}$$

Re-introducing the scaling parameter β, the request of unique LOS vectors is translated to:

$$k_1\left(\bar{\mathbf{r}}(t) + \delta\mathbf{r}(t)\right) \neq k_2\left(\beta\bar{\mathbf{r}}(t) + \delta\mathbf{r}(t)\right) \quad \forall\beta > 0 \wedge \beta \neq 1 \tag{4.7}$$

with $k_{1/2}$ replacing the denominators of (4.5). A sufficient condition to ensure that two vectors are different is when they are not parallel to each other. Mathematically, this is obtained by demanding that their cross-product is not null. Following the derivation of [6], the result requires that:

$$\delta\mathbf{r}(t) \times \bar{\mathbf{r}}(t) \neq \mathbf{0} \tag{4.8}$$

Therefore, a maneuver guarantees observability when it produces a perturbation of the trajectory $\delta\mathbf{r}(t)$ that is not aligned with the natural evolution $\bar{\mathbf{r}}(t)$, meaning:

$$\int_{t_1}^{t} \boldsymbol{\Phi}_{rv}(t,\tau)\mathbf{u}(\tau)d\tau \neq \rho(t)\boldsymbol{\Lambda}\mathbf{x}_1 \quad \forall t \in [t_1, t_k] \tag{4.9}$$

where $\rho(t)$ acts as a scaling factor. Notice that this parameter is allowed to change in time, as the only thing that matters is for the two vectors to be aligned. This relation must hold throughout all the observation period otherwise, if even a single measurement is different, the trajectory becomes observable. To prove the validity of (4.9), let us check what happens when that hypothesis is violated. Assume that the deviation $\delta\mathbf{r}(t)$ is always parallel to the nominal position vector:

$$\delta\mathbf{r}(t) = \rho(t)\bar{\mathbf{r}}(t) \tag{4.10}$$

Substituting inside (4.5), the new measurement profile becomes:

$$\boldsymbol{\iota}_r(t) = \frac{\bar{\mathbf{r}}(t) + \rho(t)\bar{\mathbf{r}}(t)}{\|\bar{\mathbf{r}}(t) + \rho(t)\bar{\mathbf{r}}(t)\|} = \frac{1+\rho(t)}{|1+\rho(t)|}\frac{\bar{\mathbf{r}}(t)}{\|\bar{\mathbf{r}}(t)\|} = \operatorname{sgn}\left(1+\rho(t)\right)\bar{\boldsymbol{\iota}}_r(t) \tag{4.11}$$

Equation (4.11) proves that for any $\rho(t) > -1$, the two unit vectors are identical. Additionally, this result is easily generalised to any arbitrary scaling β of the initial

conditions, such that $\rho(t) > -\beta$:

$$\boldsymbol{\iota}_r(t) = \frac{\beta\bar{\mathbf{r}}(t) + \rho(t)\bar{\mathbf{r}}(t)}{\|\beta\bar{\mathbf{r}}(t) + \rho(t)\bar{\mathbf{r}}(t)\|} = \operatorname{sgn}(\beta + \rho(t))\,\bar{\boldsymbol{\iota}}_r(t) \tag{4.12}$$

The conditions over $\rho(t)$ guarantee that the sign functions are always equal to one. Whenever that is not the case, the two relative unit vectors are opposite and the measurement profiles are different. Thus, (4.11) and (4.12) also highlight a potential exception to the previous criteria: even though the deviation produced by a maneuver is parallel to the natural evolution of the trajectory, the relative range can be uniquely determined if the two LOS vectors are opposite. Although theoretically valid, from a practical viewpoint this class of maneuvers is inadmissible for a rendezvous because they all result in the chaser passing through the target onto the opposite side, rotating $\boldsymbol{\iota}_r(t)$ of 180 degrees.

In summary, the necessary and sufficient conditions for observability can be written as a simple criterion by introducing the *observability angle* [39]. It represents the angle between the natural $\bar{\boldsymbol{\iota}}_r(t)$ and true $\boldsymbol{\iota}_r(t)$ line-of-sight vectors:

$$\theta(t) = \cos^{-1}\left(\bar{\boldsymbol{\iota}}_r(t) \cdot \boldsymbol{\iota}_r(t)\right) \tag{4.13}$$

This angle is directly related to the difference between the two measurement profiles. Exploiting this definition, a trajectory is said to be observable in the time-window $[t_1, t_k]$ if:

$$\exists t \in [t_1,\, t_k]: \quad \theta(t) \neq 0 \tag{4.14}$$

Meaning that, if the observability angle is different from zero at any arbitrary time of the observation window, the initial conditions can be uniquely determined. From (4.14) the unobservability criteria is easily written as:

$$\theta(t) = 0 \quad \forall t \in [t_1,\, t_k] \tag{4.15}$$

4.1.2 Analytical Derivation

The previous derivation relied on geometric considerations regarding the line-of-sight to establish the necessary and sufficient conditions for the observability of the in-orbit bearing-only problem. However, it does not apply for many practical applications. For example, one may be interested in determining the subset of maneuvers that do not produce observability. In this regard, equation (4.9) has been exploited for few very simple cases in LEO, where the dynamics can be expressed analytically, but the same approach cannot be applied to the cislunar domain. Bearing that in mind, [7] has developed an alternative methodology to establish the observability conditions, one that relies on a mathematical interpretation of the problem. Its major advantage is that it provides simple formula applicable to any system with a discrete-time solution, such is our case.

In this framework, the observability criterion is found by showing when the initial conditions can be solved from a discrete formulation of the problem. The original derivation exploits the CW equations, for which the matrices $\boldsymbol{\Phi}(t_k + \Delta t, t_k)$ and $\boldsymbol{\Phi}(t_i, +\Delta t, t_i)$ are equal for all values of k and i. As highlighted in (2.5.2), that is true only if the linear system is time-invariant; unfortunately that is not the case for the non-keplerian regime. Moreover, the expressions for unobservable maneuvers are

found by exploiting analytical solutions of $\mathbf{\Phi}$ and $\mathbf{G}$, which do not exist in our domain. On account of this, the formulation is here generalised to any linear system that admits a discrete solution in the form of (2.40) and the validity of the results obtained for impulsive and constant-thrust maneuvers is extended to problems that can only be solved numerically.

Before proceeding with the derivation, it is useful to introduce the so-called *pseudo-measurement equation*, inspired by the work of [2]. It is an algebraic manipulation of the original measurement equation, written in a linear form with respect to the relative states $\mathbf{x}$ (see [7] for the full derivation):

$$\mathbf{0} = \mathbf{H}(\mathbf{y})\mathbf{x} \tag{4.16}$$

where $\mathbf{y} = [\alpha,\ \phi]^T$ is the output vector containing the azimuth and elevation angles, respectively. $\mathbf{H}(\mathbf{y})$ is called the pseudo-matrix and is defined as:

$$\mathbf{H}(\mathbf{y}) = \begin{bmatrix} -\sin(\phi) & 0 & \operatorname{sgn}(\phi)\cos(\phi)\cos(\alpha) & 0 & 0 & 0 \\ -\sin(\alpha) & \cos(\alpha) & 0 & 0 & 0 & 0 \end{bmatrix} \tag{4.17}$$

This matrix can be determined explicitly from the knowledge of the output angles. The only downside of this expression is that it holds for any state vector as well as its opposite, whereas that is not the case for the original output equation. Specifically, $\mathbf{H}(\mathbf{y})\mathbf{x} = \mathbf{H}(\mathbf{y})(-\mathbf{x})$ even though $\mathbf{h}(\mathbf{x}) \neq \mathbf{h}(-\mathbf{x})$. Although this limitation does not have a major impact, it will impose some additional constraints on the expressions that exploit $\mathbf{H}$.

The observability requirement can be derived by considering that the state vector is made by a total of 6 components: 3 positions and 3 velocities. Since at each time-step two angles are obtained, a minimum of three different sensor readings are necessary to solve for the initial condition $\mathbf{x}_1$. The sequence of relative states over the discrete observation window $[t_1,\ t_2,\ t_3]$ is:

$$\begin{aligned} \mathbf{x}_2 &= \mathbf{\Phi}_1\mathbf{x}_1 + \mathbf{G}_1\mathbf{u} \\ \mathbf{x}_3 &= \mathbf{\Phi}_2\mathbf{\Phi}_1\mathbf{x}_1 + \mathbf{\Phi}_2\mathbf{G}_1\mathbf{u} \end{aligned} \tag{4.18}$$

where the compact notation $\mathbf{\Phi}_{k-1}$ stands for $\mathbf{\Phi}(t_k, t_{k-1})$ to remind that the matrix is evaluated with $\mathbf{x}_{t_{k-1}}$. To simplify the analysis, it is here supposed that the spacecraft is maneuvering only between the interval $[t_1,\ t_2]$. Moreover, the only assumption regarding the type of maneuver is that the resulting convolution integral can be interchanged with the product between $\mathbf{G}$ and $\mathbf{u}$. Using the newly defined matrix $\mathbf{H}$, the measurements associated to these states are written as:

$$\begin{aligned} \mathbf{0} &= \mathbf{H}(\mathbf{y}_1)\mathbf{x}_1 \\ \mathbf{0} &= \mathbf{H}(\mathbf{y}_2)\mathbf{x}_2 = \mathbf{H}(\mathbf{y}_2)\mathbf{\Phi}_1\mathbf{x}_1 + \mathbf{H}(\mathbf{y}_2)\mathbf{G}_1\mathbf{u} \\ \mathbf{0} &= \mathbf{H}(\mathbf{y}_3)\mathbf{x}_3 = \mathbf{H}(\mathbf{y}_3)\mathbf{\Phi}_2\mathbf{\Phi}_1\mathbf{x}_1 + \mathbf{H}(\mathbf{y}_3)\mathbf{\Phi}_2\mathbf{G}_1\mathbf{u} \end{aligned} \tag{4.19}$$

This system can be re-arranged in matrix form to separate the natural contribution of $\mathbf{x}_1$ from the perturbation due to $\mathbf{u}$:

$$\begin{bmatrix} \mathbf{0} \\ -\mathbf{H}(\mathbf{y}_2)\mathbf{G}_1 \\ -\mathbf{H}(\mathbf{y}_3)\mathbf{\Phi}_2\mathbf{G}_1 \end{bmatrix} \mathbf{u} = \begin{bmatrix} \mathbf{H}(\mathbf{y}_1) \\ \mathbf{H}(\mathbf{y}_2)\mathbf{\Phi}_1 \\ \mathbf{H}(\mathbf{y}_3)\mathbf{\Phi}_2\mathbf{\Phi}_1 \end{bmatrix} \mathbf{x}_1 \tag{4.20}$$

For the CW model, it has been shown that the matrix on the Right Hand Side (RHS) is full rank. The proof has been obtained by exploiting the analytical expressions of $\mathbf{H}$ and $\mathbf{\Phi}$ to create a symbolic representation of the matrix. Again, this procedure cannot be applied for our case because $\mathbf{\Phi}$ is known only numerically. However, it is easy to notice that the first two rows, represented by $\mathbf{H}(\mathbf{y}_1)$, are always linearly independent because of the inherent nature of $\mathbf{H}$. Therefore, the only exceptions could be due to particular combinations of $\mathbf{y}_i$ and $\mathbf{\Phi}_i$ that yield a zero determinant for the whole matrix. For the LEO scenario, such solutions have not been found, thus it could be reasonable to assume that the RHS matrix is always full rank even in the non-keplerian domain.

If the previous statement is valid, in order to obtain a non-trivial solution for $\mathbf{x}_1$ (i.e., $\mathbf{x}_1 \neq \mathbf{0}$), at least some components on the left side must be different from zero. Therefore, the necessary and sufficient conditions can be written as:

$$\begin{bmatrix} \mathbf{H}(\mathbf{y}_2)\mathbf{G}_1 \\ \mathbf{H}(\mathbf{y}_3)\mathbf{\Phi}_2\mathbf{G}_1 \end{bmatrix} \mathbf{u} \neq \mathbf{0} \tag{4.21}$$

By analysing this system, the very same observations made through a geometric formulation of the problem, can now be established mathematically. Indeed, in order for (4.21) to be satisfied, the input $\mathbf{u}$ must be different from zero. Namely, a necessary condition for observability is the execution of a maneuver. Moreover, as previously seen, even if a maneuver is performed, observability is not necessarily granted. This happens whenever the nullity of the matrix in (4.21) (i.e. the number of vectors in its null-space) is greater than zero.

This result can be generalised to multiple maneuvers over any number of sample intervals. For example, if a second maneuver was performed at time t_2, the system (4.20) would become:

$$\begin{bmatrix} \mathbf{0} \\ -\mathbf{H}(\mathbf{y}_2)\mathbf{G}_1 \\ -\mathbf{H}(\mathbf{y}_3)\mathbf{\Phi}_2\mathbf{G}_1 \end{bmatrix} \mathbf{u}_1 + \begin{bmatrix} \mathbf{0} \\ \mathbf{0} \\ -\mathbf{H}(\mathbf{y}_3)\mathbf{G}_2 \end{bmatrix} \mathbf{u}_2 = \begin{bmatrix} \mathbf{H}(\mathbf{y}_1) \\ \mathbf{H}(\mathbf{y}_2)\mathbf{\Phi}_1 \\ \mathbf{H}(\mathbf{y}_3)\mathbf{\Phi}_2\mathbf{\Phi}_1 \end{bmatrix} \mathbf{x}_1 \tag{4.22}$$

Equation (4.22) underlines again that in order to have a non-trivial solution for $\mathbf{x}_1$, at least one between $\mathbf{u}_1$ and $\mathbf{u}_2$ must be different from zero and the null-space of the corresponding matrix must be empty. The benefit of adding a second maneuver is an increased flexibility of the system. Indeed, assuming $\mathbf{u}_1$ different from zero but unobservable, the initial conditions can still be recovered if $\mathbf{u}_2$ is observable. By manipulating the expressions in (4.19), it can be proved that this observability condition is physically translated into requiring that at least one of the measurements after the maneuver took place must be different from the natural evolution of the dynamics [7].

4.1.3 Non-linear Effects

Before investigating the subsets of unobservable maneuvers, it is appropriate to quantify the ability of non-linear terms to enhance the observability of the system. The approach suggested by [6] is to treat the neglected accelerations as *pseudo-maneuvers* and analytically evaluate their contribution from the measurement profile equation. As that is not feasible for the case at hand, a different measure of observability is proposed, inspired by the work of [47].

Given an arbitrary finite set of measurement times $\mathcal{T} = [t_1, t_2, ..., t_N]$, it is possible to define a function $\mathbf{V}(\mathbf{x}) : \mathbb{R}^6 \to \mathbb{R}^{2N}$ as:

$$\mathbf{V}(\mathbf{x}) = \begin{bmatrix} (\mathbf{h} \circ \mathbf{\Phi}_1)(\mathbf{x}) \\ (\mathbf{h} \circ \mathbf{\Phi}_2)(\mathbf{x}) \\ \vdots \\ (\mathbf{h} \circ \mathbf{\Phi}_N)(\mathbf{x}) \end{bmatrix} \tag{4.23}$$

where $\circ$ is used to indicate $(\mathbf{h} \circ \mathbf{\Phi})\mathbf{x} = \mathbf{h}(\mathbf{\Phi}\mathbf{x})$, that is, the composition of the two functions. Its purpose is to map a generic initial state $\mathbf{x}$ to all the corresponding measurements over the interval $\mathcal{T}$. In order to evaluate the observability properties of a reference point $\mathbf{x}_1$, the functional $J_{x_1} : \mathbb{R}^6 \to \mathbb{R}$ is introduced as follows:

$$J_{x_1}(\mathbf{x}) = \|\mathbf{V}(\mathbf{x}) - \mathbf{V}(\mathbf{x}_1)\| \tag{4.24}$$

Equation (4.24) can be exploited to evaluate the observability of a generic initial point $\mathbf{x}_1$ with respect to any other point belonging to a given domain Ω. In other words, it quantifies the difference between the measurements of the reference dynamics and those of all the other trajectories that originate from the points contained in Ω. It is easy to notice that if the LOS vectors of two trajectories are identical, then $\mathbf{V}(\mathbf{x}_2) = \mathbf{V}(\mathbf{x}_1)$ and $J_{x_1}(\mathbf{x_2}) = 0$. Therefore, if it exists a point $\mathbf{x} \in \Omega$ such that the functional $J_{x_1}(\mathbf{x}) = 0$, then $\mathbf{x}_1$ is locally unobservable because its measurement profile is not unique. This observability measure can then be viewed as a natural generalization of observability gramians to a nonlinear framework [47]. Additionally, since the definition of J_{x_1} does not require the measurement equation to be a linear function of $\mathbf{x}$, it can be effectively used to investigate the ability of the neglected non-linear dynamics to enhance the observability of the system.

Under few simplifying assumptions, this formulation has been applied to the case study of Fig. 4.1 and the resulting values of J_{x_1} are illustrated in the figure below.

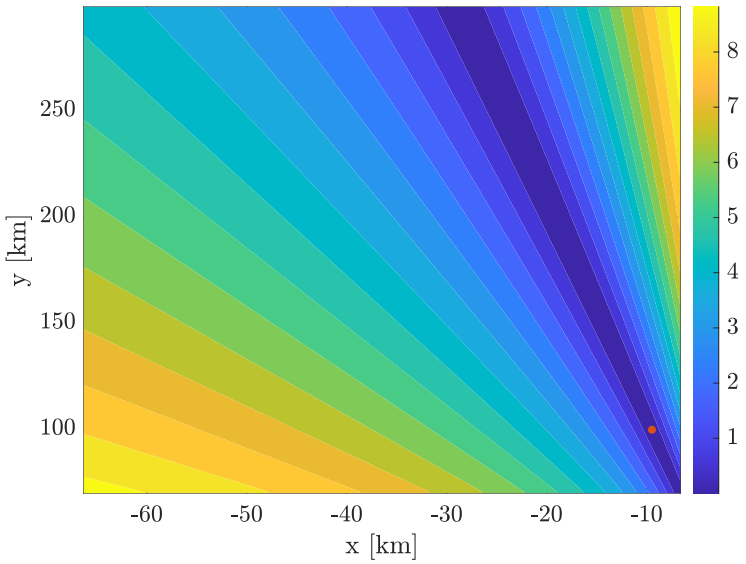

FIGURE 4.2: Non-linear observability levels of J_{x_1} for a Lyapunov orbit in the domain $\Omega(x, y) : x \in [-70, -5]$ and $y \in [50, 300]$ km. The reference point $\mathbf{x}_1$ is highlighted as a red dot.

In order to show the level sets of J_{x_1} in a two-dimensional plot, the space of the solutions has been reduced from $\mathbb{R}^6$ to $\mathbb{R}^2$. In particular, by studying the behaviour of the chaser relative to a target on a Lyapunov orbit, the CR3BP dynamics can be reduced to a planar motion (i.e, $\mathbf{x}_1 \in \mathbb{R}^4$). Additionally, since the purpose of this analysis is to evaluate whether or not the non-linear contributions can compensate the original unobservability, the ratio between the i^{th} velocity component of $\mathbf{x}$ and that of $\mathbf{x}_1$ is chosen equal to the ratio between the respective position elements. Namely, if $y_2 = 3y_1$ then $\dot{y}_2 = 3\dot{y}_1$. This assumption allows for a direct comparison with Figure 4.1 because it makes possible to include in Ω all the points obtained by equally scaling the components of $\mathbf{x}_1$ for a given range of β; that is, the unobservable trajectories of the linear formulation.

The results display a net drop of observability in the neighbourhood of the unobservable region. Nevertheless, the lowest value of J_{x_1} is close but different from zero, meaning that the non-linear terms ideally make the reference point observable in Ω. However, the low values of J_{x_1} indicate that the difference between the measurement profiles are very small thus, from a practical perspective, one may argue that the degree of observability is not high enough to guarantee the convergence of the navigation filter. Moreover, if measurements errors are introduced, very precise sensors might be needed to distinguish the two sets of measurements.

Additional insights on the observability problem are gained by evaluating the functional J_{x_0} for different durations of the observation time $\mathcal{T}$.

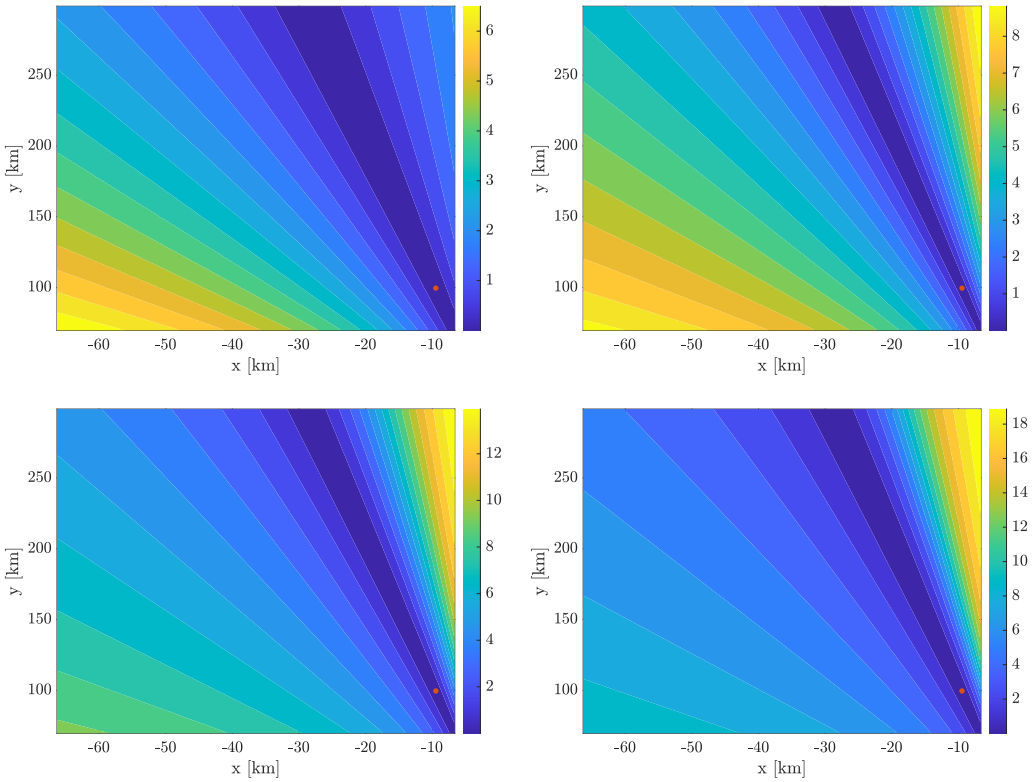

FIGURE 4.3: Comparison between the local observability gramiams J_{x_1} for increasing durations of the observation interval $\mathcal{T}$ (0.5, 1, 1.5 and 2 days). The target is placed on a L1 Lyapunov orbit and the reference point is marked with a red dot. Notice that the color scale is different for each plot.

Figure 4.3 shows that the bottom-left part of the xy-domain has the highest degree of observability for short propagation times. However, as the observation window is increased, the top-right corner outclasses completely the lower region. Therefore, as a reminder for future analysis, it is important to remark that the observability of a generic trajectory strongly depends on the time used to evaluate it. A trajectory profile that has a low level of observability early-on might show sudden changes with respect to the nominal trajectory at a later stage.

A few final considerations are worth to be made. The linear model holds as long as the effects of non-linearities are small and non-influential. Therefore, it is to be expected that their contribution to the overall observability of the system is negligible. If that was not the case, concerns could rise on its ability to approximate the real dynamics. Bearing that in mind, this investigation further proved the validity of the linear analysis. Indeed, the lowest values of J_{x_1} are all associated to the region where the linear criteria foresaw unobservability and, even after long propagation times, the results are still in agreement with the linear predictions. Nonetheless, since the relative dynamics in the CR3BP depends on the positions of both the target and the chaser, there could be certain combinations that provide a much higher degree of observability than the one of this planar example. Furthermore, an additional enhancement might be obtained translating to the full ephemeris dynamics.

As a last remark, the high deviations from the reference point, visible at the top-left of the fourth plot, should not be mistaken with a high level of local observability. Indeed, as explained earlier, a measure of observability over Ω is represented by the lowest value of J_{x_1} in the domain.

4.2 Unobservable Maneuvers

It is now of interest to search for the sub-sets of unobservable maneuvers. Their analysis would validate the observability criteria derived previously and provide insights on what type of maneuvers shall not be performed if a bearing-only navigation solution is being exploited. Again, the derivation follows the steps of [7], generalising the analysis to linear time-variant systems and extending the results of impulsive and constant-thrust maneuvers in LEO to the non-keplerian dynamics.

To derive the unobservable maneuvers, consider the expression for the position vectors with and without an input for three consecutive time-steps:

$$\begin{aligned} \mathbf{r}_2 &= \mathbf{\Lambda}_1\mathbf{x}_1 + \mathbf{\Gamma}_1\mathbf{u} \quad \text{and} \quad \bar{\mathbf{r}}_2 = \mathbf{\Lambda}_1\mathbf{x}_1 \\ \mathbf{r}_3 &= \mathbf{\Lambda}_2\mathbf{\Phi}_1\mathbf{x}_1 + \mathbf{\Lambda_2}\mathbf{G}_1\mathbf{u} \quad \text{and} \quad \bar{\mathbf{r}}_3 = \mathbf{\Lambda}_2\mathbf{\Phi}_1\mathbf{x}_1 \\ \mathbf{r}_4 &= \mathbf{\Lambda}_3\mathbf{\Phi}_2\mathbf{\Phi}_1\mathbf{x}_1 + \mathbf{\Lambda_3}\mathbf{\Phi}_2\mathbf{G}_1\mathbf{u} \quad \text{and} \quad \bar{\mathbf{r}}_4 = \mathbf{\Lambda}_3\mathbf{\Phi}_2\mathbf{\Phi}_1\mathbf{x}_1 \end{aligned} \tag{4.25}$$

where $\mathbf{\Gamma}$ is extracted from:

$$\mathbf{G} = \begin{bmatrix} \mathbf{\Gamma} & \mathbf{G}_v \end{bmatrix}^T \tag{4.26}$$

As seen in section (4.1.1), a maneuver is unobservable if it produces a perturbation parallel to the line-of-sight vector. Therefore, in order for the three equations of (4.25)

to hold simultaneously, the system can be re-written as:

$$\begin{cases} \rho_1 \left(\mathbf{\Lambda}_1 \mathbf{x}_1 + \mathbf{\Gamma}_1 \mathbf{u} \right) = \mathbf{\Lambda}_1 \mathbf{x}_1 \\ \rho_2 \left(\mathbf{\Lambda}_2 \mathbf{\Phi}_1 \mathbf{x}_1 + \mathbf{\Lambda}_2 \mathbf{G}_1 \mathbf{u} \right) = \mathbf{\Lambda}_2 \mathbf{\Phi}_1 \mathbf{x}_1 \\ \rho_3 \left(\mathbf{\Lambda}_3 \mathbf{\Phi}_2 \mathbf{\Phi}_1 \mathbf{x}_1 + \mathbf{\Lambda}_3 \mathbf{\Phi}_2 \mathbf{G}_1 \mathbf{u} \right) = \mathbf{\Lambda}_3 \mathbf{\Phi}_2 \mathbf{\Phi}_1 \mathbf{x}_1 \end{cases} \tag{4.27}$$

For any arbitrary constant $\rho_i \neq 0$. However, it was demonstrated that if the two position vectors are opposite, the measurement profiles are different. Thus the three constants are also constrained to be positive: $\rho_i > 0$. Mathematically, unobservability requires the two position vectors to be positive linear dependent (i.e., point in the same direction). Re-arranging (4.27) by separating the natural and forced responses, these equations turn into:

$$\begin{cases} \alpha_1 \mathbf{\Lambda}_1 \mathbf{x}_1 = \mathbf{\Gamma}_1 \mathbf{u} \\ \alpha_2 \mathbf{\Lambda}_2 \mathbf{\Phi}_1 \mathbf{x}_1 = \mathbf{\Lambda}_2 \mathbf{G}_1 \mathbf{u} \qquad \text{for any} \quad \alpha_i > -1 \\ \alpha_3 \mathbf{\Lambda}_3 \mathbf{\Phi}_2 \mathbf{\Phi}_1 \mathbf{x}_1 = \mathbf{\Lambda}_3 \mathbf{\Phi}_2 \mathbf{G}_1 \mathbf{u} \end{cases} \tag{4.28}$$

where $\alpha_i = 1/\rho_i - 1$. In order for the two trajectories to be indistinguishable, the system (4.28) must also be valid for every subsequent time step after the maneuver. Now, considering the first equation, the matrix $\mathbf{\Gamma}$ can be inverted to solve for the unobservable maneuver. There are some special exceptions that might make this matrix singular, alluding that unobservable maneuvers do not exist for those scenarios. Nevertheless, if that is the case, these restrictions will be reflected in the final solution [7]. The unobservable maneuvers can then be evaluated as:

$$\mathbf{u}_u = \alpha \mathbf{\Gamma}_1^{-1} \mathbf{\Lambda}_1 \mathbf{x}_1 \quad \text{for} \quad \alpha > -1 \wedge \alpha \neq 0 \tag{4.29}$$

The constraint $\alpha \neq 0$ is added to avoid trivial solutions where $\mathbf{u}_u$ is null, namely the cases where no maneuver is performed. It is interesting to notice that this expression for $\mathbf{u}_u$ depends on the initial point $\mathbf{x}_1$, meaning that unobservable maneuvers exist only for specific initial conditions. Therefore, before evaluating $\mathbf{u}_u$ it is necessary to solve for this set of initial conditions by substituting (4.29) inside the last two equations in (4.28). Since the initial state vector is made of 6 components, it should now be clear why the positions for 2 additional time-steps have been propagated throughout this derivation.

$$\begin{cases} \alpha_2 \mathbf{\Lambda}_2 \mathbf{\Phi}_1 \mathbf{x}_1 - \alpha_1 \mathbf{\Lambda}_2 \mathbf{G}_1 \mathbf{\Gamma}_1^{-1} \mathbf{\Lambda}_1 \mathbf{x}_1 = \mathbf{0} \\ \alpha_3 \mathbf{\Lambda}_3 \mathbf{\Phi}_2 \mathbf{\Phi}_1 \mathbf{x}_1 - \alpha_1 \mathbf{\Lambda}_3 \mathbf{\Phi}_2 \mathbf{G}_1 \mathbf{\Gamma}_1^{-1} \mathbf{\Lambda}_1 \mathbf{x}_1 = \mathbf{0} \end{cases} \tag{4.30}$$

After some algebra, defining $\beta_i = \alpha_{i+1}/\alpha_1$, the system reads:

$$\begin{cases} \mathbf{\Lambda}_2 (\beta_1 \mathbf{\Phi}_1 - \mathbf{G}_1 \mathbf{\Gamma}_1^{-1} \mathbf{\Lambda}_1) \mathbf{x}_1 = \mathbf{0} \\ \mathbf{\Lambda}_3 \mathbf{\Phi}_2 (\beta_2 \mathbf{\Phi}_1 - \mathbf{G}_1 \mathbf{\Gamma}_1^{-1} \mathbf{\Lambda}_1) \mathbf{x}_1 = \mathbf{0} \end{cases} \tag{4.31}$$

for $\beta_i \neq 0$. Both equations must be valid when $\mathbf{x}_1$ is different from zero. The only way for this to be possible, is if the intersection between the null-spaces of the two matrices on the LHS is not empty, for any choice of β_i that satisfies the constraints. In this regard, a product between two matrices is a linear map by definition. Therefore, the two terms $\mathbf{\Lambda}_2$ and $\mathbf{\Lambda}_3 \mathbf{\Phi}_2$ can be viewed as linear transformations of the matrices they multiply inside the brackets. This implies that the nullspace of each LHS matrix is a sub-space of the null-space of the respective matrix between the parenthesis.

Therefore, to have a non-empty intersection between the two sub-spaces, the terms in the brackets must be equal, meaning that $\beta_1 = \beta_2$. Additionally, to obtain a non-empty null-space for a matrix, its determinant must be zero.

Thus, the basis that describes the set of initial conditions that allow for unobservable maneuvers can be found from:

$$\mathbf{x}_{0_u} = \text{null}(\mathbf{C}) \quad \text{for} \quad \beta \neq 0 \ \wedge \ \det(\mathbf{C}) = 0 \tag{4.32}$$

where:

$$\mathbf{C} = \beta\mathbf{\Phi}_1 - \mathbf{G}_1\mathbf{\Gamma}_1^{-1}\mathbf{\Lambda}_1 \tag{4.33}$$

It is important to remark that this result has been obtained by assuming that a single maneuver was performed, with an arbitrary duration between the interval $[t_0, t_1]$. A similar formula can be found by assuming that a series of maneuvers is executed, however the more equations are added and the less likely it is that an intersection between the null-spaces exists. Finally notice no assumption on the type of maneuver has been made and (4.33) is valid for any maneuver that can be represented by a matrix $\mathbf{G}$.

To summarise, the procedure to find an unobservable maneuver is as follows:

1. The type of maneuver is selected and the corresponding matrices $\mathbf{G}$ and $\mathbf{\Gamma}$ are evaluated for an arbitrary duration. $\mathbf{\Phi}$ and $\mathbf{\Lambda}$ are also computed over the same time interval.

2. The values of β that yield a null determinant for $\mathbf{C}$ and respect the constraints in (4.32) are sought.

3. The set $\mathbf{x}_{1_u}$ of initial conditions that allow for unobservable maneuvers is obtained by a linear combination of the vectors inside the null-space of $\mathbf{C}$, evaluated for the values of β found at the previous step.

4. Finally, the unobservable maneuver $\mathbf{u}_u$ is obtained by substituting $\mathbf{x}_{0_u}$ inside (4.29).

The initial conditions and the associated impulsive and constant-thrust unobservable maneuvers are now computed numerically and generalised. This will allow to compare the results coming from the CW equations with those of the non-keplarian dynamics. Other types of maneuvers are not investigated because they either do not allow a matrix $\mathbf{G}$ or are less likely to be performed during a rendezvous operation.

4.2.1 Impulsive Maneuvers

Accordingly to the following sub-division of the state transition matrix:

$$\mathbf{\Phi} = \begin{bmatrix} \mathbf{\Phi}_{rr} & \mathbf{\Phi}_{rv} \\ \mathbf{\Phi}_{vr} & \mathbf{\Phi}_{vv} \end{bmatrix} \tag{4.34}$$

for impulsive maneuvers, the input matrices can be written as (2.39):

$$\mathbf{G}_k = \mathbf{\Phi}_k \begin{bmatrix} \mathbf{0} \\ \mathbf{I} \end{bmatrix} = \begin{bmatrix} \mathbf{\Phi}_{rv} \\ \mathbf{\Phi}_{vv} \end{bmatrix} \quad \text{and} \quad \mathbf{\Gamma}_k = \mathbf{\Phi}_{rv} \tag{4.35}$$

From now on, the k-subscript will be dropped as all the matrices are computed over the same time interval. Temporarily define $\mathbf{R}$ equal to the second term of the RHS in (4.33), then:

$$\mathbf{R} = \mathbf{G}\boldsymbol{\Gamma}^{-1}\boldsymbol{\Lambda} = \begin{bmatrix} \boldsymbol{\Phi}_{rv} \\ \boldsymbol{\Phi}_{vv} \end{bmatrix} \boldsymbol{\Phi}_{rv}^{-1} \begin{bmatrix} \boldsymbol{\Phi}_{rr} & \boldsymbol{\Phi}_{rv} \end{bmatrix} \tag{4.36}$$

Taking the products yields:

$$\mathbf{R} = \begin{bmatrix} \boldsymbol{\Phi}_{rv}\boldsymbol{\Phi}_{rv}^{-1}\boldsymbol{\Phi}_{rr} & \boldsymbol{\Phi}_{rv} \\ \boldsymbol{\Phi}_{vv}\boldsymbol{\Phi}_{rv}^{-1}\boldsymbol{\Phi}_{rr} & \boldsymbol{\Phi}_{vv} \end{bmatrix} = \begin{bmatrix} \boldsymbol{\Phi}_{rr} & \boldsymbol{\Phi}_{rv} \\ \boldsymbol{\Phi}_{vv}\boldsymbol{\Phi}_{rv}^{-1}\boldsymbol{\Phi}_{rr} & \boldsymbol{\Phi}_{vv} \end{bmatrix} \tag{4.37}$$

Therefore, the original matrix $\mathbf{C}$ simplifies to:

$$\mathbf{C} = \beta\boldsymbol{\Phi} - \mathbf{R} = \begin{bmatrix} (\beta-1)\boldsymbol{\Phi}_{rr} & (\beta-1)\boldsymbol{\Phi}_{rv} \\ \beta\boldsymbol{\Phi}_{vr} - \boldsymbol{\Phi}_{vv}\boldsymbol{\Phi}_{rv}^{-1}\boldsymbol{\Phi}_{rr} & (\beta-1)\boldsymbol{\Phi}_{vv} \end{bmatrix} \tag{4.38}$$

For this type of matrix, solving for null values of the determinant always yields 6 solutions for β, three with $\beta = 0$ and three for $\beta = 1$. Since $\beta = 0$ violates the constraints (4.32), the initial conditions for impulsive unobservable maneuvers are found from the null space of $\mathbf{C}$ evaluated for $\beta = 1$:

$$\mathbf{x}_{0_u} = \text{null}\left(\begin{bmatrix} \mathbf{0}_{3x3} & \mathbf{0}_{3x3} \\ \boldsymbol{\Phi}_{vr} - \boldsymbol{\Phi}_{vv}\boldsymbol{\Phi}_{rv}^{-1}\boldsymbol{\Phi}_{rr} & \mathbf{0}_{3x3} \end{bmatrix} \right) \tag{4.39}$$

A vector basis for the null-space of this matrix has the form of:

$$\mathbf{x}_{0_u} = \left\{ \begin{bmatrix} 0 \\ 0 \\ 0 \\ 1 \\ 0 \\ 0 \end{bmatrix}, \begin{bmatrix} 0 \\ 0 \\ 0 \\ 0 \\ 1 \\ 0 \end{bmatrix}, \begin{bmatrix} 0 \\ 0 \\ 0 \\ 0 \\ 0 \\ 1 \end{bmatrix} \right\} = \begin{bmatrix} 0 \\ 0 \\ 0 \\ v_x \\ v_y \\ v_z \end{bmatrix} = \begin{bmatrix} \mathbf{0} \\ \mathbf{v} \end{bmatrix} \tag{4.40}$$

Equation (4.40) implies that unobservable impulsive maneuvers can only be performed at the origin; that is, when the chaser and the target are in the same position. The unobservable maneuver is found by substituting (4.40) into (4.29):

$$\mathbf{u}_u = \alpha\boldsymbol{\Phi}_{rv}^{-1} \begin{bmatrix} \boldsymbol{\Phi}_{rr} & \boldsymbol{\Phi}_{rv} \end{bmatrix} \begin{bmatrix} \mathbf{0} \\ \mathbf{v} \end{bmatrix} = \alpha\boldsymbol{\Phi}_{rv}^{-1}\boldsymbol{\Phi}_{rv}\mathbf{v} \tag{4.41}$$

The final expression is:

$$\mathbf{u}_u = \alpha\mathbf{v} \quad \text{for} \quad \alpha > -1 \wedge \alpha \neq 0 \tag{4.42}$$

Equations (4.40) and (4.42) highlight that for impulsive maneuvers, unobservable trajectories are obtained only when the maneuver is executed at the origin and in a direction parallel to the initial relative velocity. This result has been obtained without making any assumption on the numerical values of $\boldsymbol{\Phi}$, therefore it holds for any dynamic system that can be represented in discrete form. As a last remark, note that the components of $\mathbf{v}$ are independent and can assume any arbitrary value, both positive and negative.

Figure 4.4 shows the trajectory associated to an unobservable impulsive maneuver

for a random value of the initial velocity, with the target located at the NRHO apolune. It is easily noticed that the forced dynamics is an exact scaled copy of the natural relative evolution.

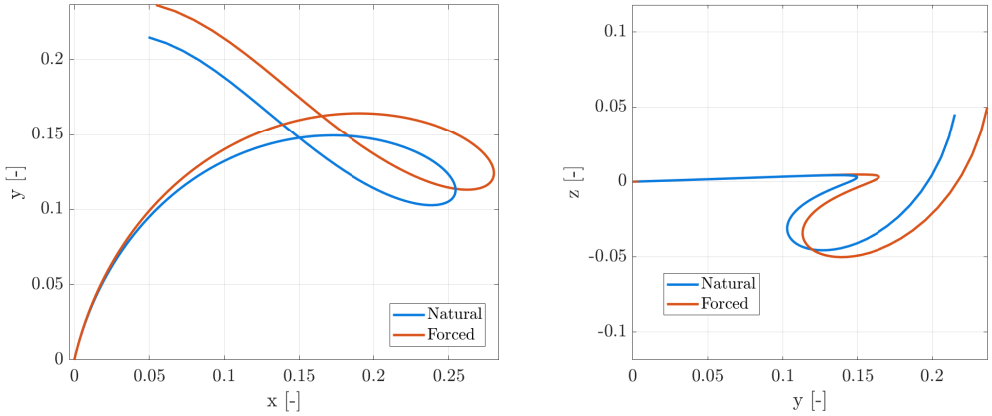

(*a*) Projection in the x-y plane. (*b*) Projection in the y-z plane.

FIGURE 4.4: Projections of the natural and forced dynamics for an unobservable impulsive maneuver.

The trajectories have been propagated with the linear model and the amplitude of the maneuver has been set to an arbitrary high value to easily distinguish the two lines.

The disagreements between the readings of the two trajectories are reported in Figure 4.5. For the linear model, the differences have the same order of magnitude of the integration tolerances, thus are completely negligible. The same is true for the real dynamics; indeed, despite the results are much higher with respect to the linear model, in practice they never exceed 0.1°. The smallest differences are found at the beginning of the propagation where the accuracy of the approximation is highest ($\sim$ 0.001° at 10 hours). Overall, this comparison highlights once again the high-degree of reliability of the linear formulation.

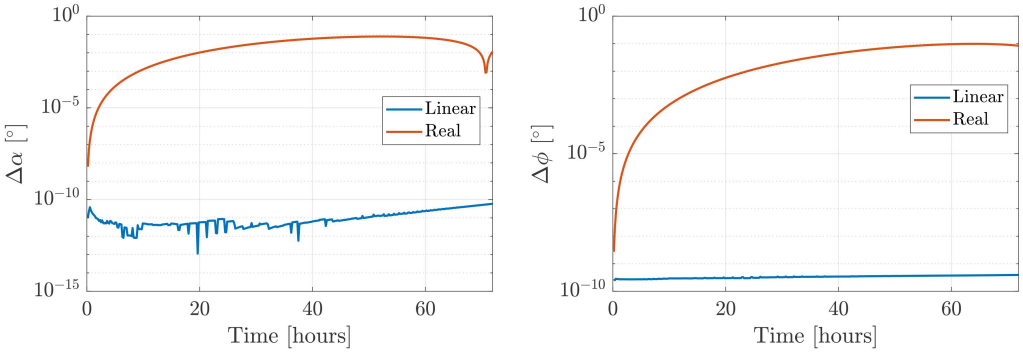

(*a*) Azimuth differences. (*b*) Elevation differences.

FIGURE 4.5: Comparison between the measurements differences of the linear and non-linear dynamics.

Additionally, some interesting considerations can be made from an operational viewpoint. As highlighted by [7], it is almost impossible that the conditions for an impulsive unobservable maneuver are satisfied in a real rendezvous operation. Indeed, as the initial conditions are located in the origin, all the maneuvers that are computed during an arrival trajectory are going to be observable. Moreover, a null relative position would require the chaser to cross the position of the target, resulting

in a collision between the two spacecraft. Even so, when the relative distances are very small, the bearing-only technique is outclassed by other navigation solutions in terms of accuracy, thus even for a departing spacecraft impulsive unobservable maneuvers should be of no concern whatsoever.

4.2.2 Constant-Thrust Maneuvers

In the previous case, the particular structure of the input matrix **G** was exploited to find analytical expressions for the unobservable maneuver and the associated initial conditions. Unfortunately, if constant thrust maneuvers are executed, the matrix **G** cannot be reduced to a simpler form, thus one has to rely on the numerical computation of the convolution integral in (2.39).

However, it is interesting to notice that multiple numerical evaluations of **C** have shown that it can be expressed as:

$$\mathbf{C} = \begin{bmatrix} (\beta-1)\mathbf{\Phi}_{rr} & (\beta-1)\mathbf{\Phi}_{rv} \\ \beta\mathbf{\Phi}_{vr} - \mathbf{R}_{vr} & \beta\mathbf{\Phi}_{vv} - \mathbf{R}_{vv} \end{bmatrix} \tag{4.43}$$

where the $\mathbf{R}_{vr}$ and $\mathbf{R}_{vv}$ are the sub-portions of **R**, defined accordingly to (4.34). Thus, it is clear that if $\beta = 1$, the first three rows vanish and the determinant is null. By exploiting symbolic expressions, the remaining three solutions have been found to be $\beta = 0$ and are thus inadmissible. Similarly to the previous derivation, substituting $\beta = 1$ in (4.43) yields:

$$\mathbf{C} = \begin{bmatrix} \mathbf{0}_{3x3} & \mathbf{0}_{3x3} \\ \mathbf{C}_{vr} & \mathbf{C}_{vv} \end{bmatrix} \tag{4.44}$$

Since the rank of this matrix is 3, from the Rank-Nullity theorem, the null-space of **C** will always have a dimension of 3. Moreover, the reduced Row Echelon Form (REF) for a matrix of this type is written as:

$$\mathbf{C}_{REF} = \begin{bmatrix} \mathbf{I}_{3x3} & \mathbf{A} \\ \mathbf{0}_{3x3} & \mathbf{0}_{3x3} \end{bmatrix} \tag{4.45}$$

where, in the most general case, **A** is a full matrix of unknown coefficients. From this representation, one can see that the basis of the nullspace of **C** (i.e, the set of unobservable initial conditions) has the form of:

$$\mathbf{x}_{0_u} = \left\{ \begin{bmatrix} a_1 \\ a_2 \\ a_3 \\ 1 \\ 0 \\ 0 \end{bmatrix}, \begin{bmatrix} b_1 \\ b_2 \\ b_3 \\ 0 \\ 1 \\ 0 \end{bmatrix}, \begin{bmatrix} c_1 \\ c_2 \\ c_3 \\ 0 \\ 0 \\ 1 \end{bmatrix} \right\} = \begin{bmatrix} \mathbf{r}_0 \\ \mathbf{v}_0 \end{bmatrix} \tag{4.46}$$

Since $\mathbf{x}_{1_u}$ can be obtained by any linear combination of these basis vectors, any location in the three-dimensional domain allows for a specific unobservable constant-thrust maneuver. This statement is best proven with an example. Define $\mathbf{r}_D$ a generic position vector and let the position-related components of the basis vectors in (4.46) be $\{\mathbf{a}, \mathbf{b}, \mathbf{c}\}$. The goal is to find the coefficients $\boldsymbol{\alpha}$ that yield a linear combination of

these vectors equal to $\mathbf{r}_D$. Mathematically:

$$[\mathbf{a},\ \mathbf{b},\ \mathbf{c}]\,\boldsymbol{\alpha} = \mathbf{r}_D \tag{4.47}$$

By definition, **a**, **b** and **c** are linearly independent, therefore the matrix on the LHS can be inverted to find a unique solution for $\boldsymbol{\alpha}$. Additionally, since the basis vectors in (4.46) are defined with unitary velocity components, these coefficients are also equal to the relative initial velocity that allows for the unobservable maneuver.

In summary, for non-impulsive trajectories in any point an unobservable constant thrust maneuver can be performed; however, for each of these positions there exist only a unique value of the initial velocity that allows it. An example for this kind of maneuvers is reported in Figure 4.6.

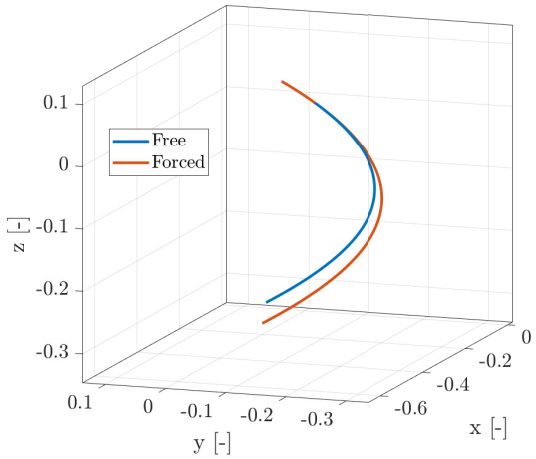

FIGURE 4.6: Comparison between the natural and forced dynamics for an unobservable constant-thrust maneuver.

It is here remarked that the expressions for the unobservable maneuvers have been found under the assumption that the action is performed for any arbitrary duration of the first time step $[t_1, t_2]$. As a result, the generated trajectories are unobservable only when the maneuver is ceased. This stands clear in Figure 4.5, where the measurement differences reach peaks higher than 1° during the maneuvering phase. However, once the firing has stopped, the values of the linear model are again in the order of the integration tolerances.

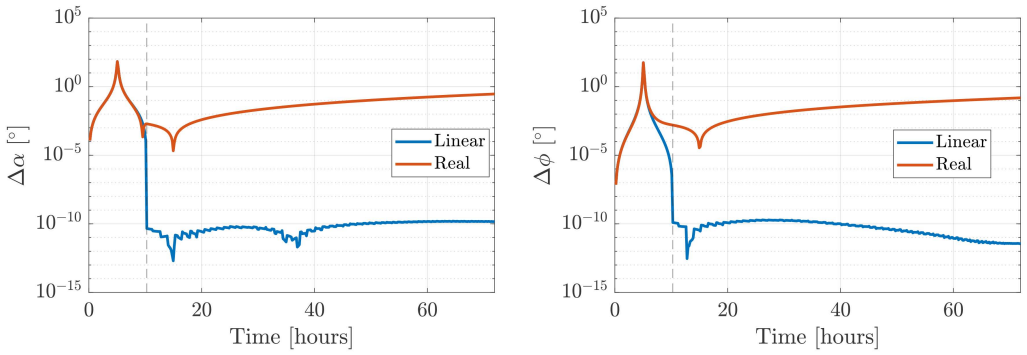

(*a*) Azimuth differences.

(*b*) Elevation differences.

FIGURE 4.7: Comparison between the measurements differences for constant thrust maneuvers. The dotted line represents when the firing is ceased.

Although some degree of observability is provided by these trajectories, the disagreements in the measurement profiles may not be high enough to either guarantee the convergence of the filter or be distinguished by the noisy sensors. Indeed, in the example above the differences are below 0.1° for most of the maneuvering time. Thus, these kind of maneuvers should still be avoided for proximity operations that only rely on angle measurements.

The analysis carried out in these sections, generalised the concepts introduced by [7] and [39] to any linear system that admits a solution in discrete form. It showed that a necessary and sufficient condition for observability is to perform a maneuver that changes the measurement profile from that of the natural evolution. Additionally, it highlighted that in a practical scenario, impulsive maneuvers are never going to be unobservable, whereas the same does not hold when continuous thrust is introduced. Finally, the constant comparisons with the non-linear model proved that the classical techniques of linear analysis can effectively be exploited to investigate the relative motion in the cislunar domain.

4.3 Observability Measures

In an ideal scenario, a system is either observable or unobservable. When a particular dynamics belongs to the former class, the error in the estimation of the state variables will asymptotically approach zero. In this regard, the work in the previous section established the necessary and sufficient criteria to classify a trajectory as either observable or unobservable. However, the real world is far from ideal and when sensor errors are introduced, the convergence of the filter is not granted. A perfect example is given by the set of unobservable maneuvers in Figure 4.7. As already discussed, during the firing, the direction of the LOS vector is slightly different from that of the natural dynamics. Thus, from a theoretical standpoint the trajectories are observable. Nonetheless, when measurements errors are accounted for, the navigation filter may either not be able to distinguish between the two measurement profiles or take a long time to reduce the error below a design threshold.

Therefore, for real applications, it is useful to introduce a measure for the level of observability; one that can be used to classify different trajectories as more or less observable. A high degree of observability would then imply the possibility of great improvements of the navigation estimate. Additionally, an analytical expression for this measure of observability would provide the means to optimise and solve for the maneuvers that guarantee the maximum improvement in the navigation error. This expression should also allow to account for the specific time upon which observability is desired. Indeed, consider the simple scenario where a chaser measures its relative state each hour. Since the filter can only process the information coming from the sensors, it does not matter how much observable the trajectory is in-between two consecutive measurements; the key factor to ensure the error is reduced is to have observability at the same time the measurements are performed.

In the last decade, this problem has been tackled by different authors. In particular, [39] proposed an expression based on the concept of the observability angle, but its complexity allows analytical solutions only in very few simple cases. Additionally, since that measure may vary of many orders of magnitude, different non-linear optimizers struggled at finding a feasible solution when additional terms (e.g., fuel costs) were included in the overall cost function. [48] used the Fisher Information matrix to

gain insights on the estimation performance of the navigation filter and exploited a non-linear solver to find the optimal maneuver. Finally, [12] developed a continuous measure of observability based on the positive linear independence of the perturbed and natural position vectors. Due to its simple nature, this last proposal allows to find a closed-form solution for the optimal observable maneuvers; one that can be applied to any dynamic system/maneuver type that admits a discrete-form matrix solution.

Bearing this in mind, the remaining of the section is structured as follows. The concept of observability angle is recalled to highlight the different factors (e.g, sensor errors and maneuver directions) that affect the estimation of the range and quantify their impact. Then, the analytical expression for the optimal observable maneuvers of [12] is generalised to time-variant linear systems. Finally, numerical simulations are used to verify the ability of this kind of maneuvers to yield the best improvement in the navigation estimate.

4.3.1 Observability Angle

The geometry of the range detectability is well illustrated by Figure 4.8, where the target (the grey circle) is fixed in the origin of the system and the chaser position is depicted before and after the observable maneuver (red circles). The angle γ is called the *perturbation angle* and is the angle between the natural position vector $\bar{\mathbf{r}}$ and the perturbation $\delta\mathbf{r}$ due to the observable maneuver. For the ideal scenario (i.e, perfect measurements), the relative distance ρ can be found through the law of sines:

$$\rho = \delta \mathrm{r} \left[\frac{\sin(\theta + \gamma)}{\sin(\theta)} \right] \tag{4.48}$$

Unfortunately, the sensor readings will always be affected by some kind of noise, leading to an inherent uncertainty in the range estimation. These could be due to pixel misreadings or to errors in the image processing algorithms.

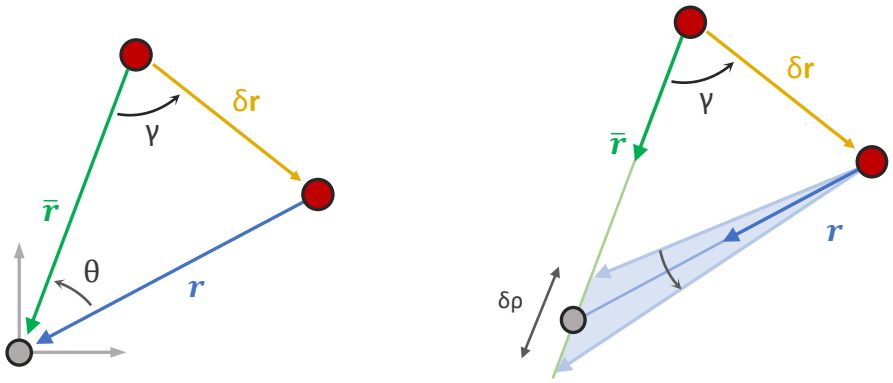

FIGURE 4.8: Range detectability geometry in the ideal (*left*) and real (*right*) scenario. $\mathbf{r}$ is the position vector of the real trajectory whereas $\bar{\mathbf{r}}$ represents the natural dynamics.

In a real application, [39] has shown that the position uncertainty can be written as function of the observability angle θ, the perturbation angle γ and the sensor accuracy ε. The resulting expression is quite complex but if measurement errors are

small, it can be simplified to:

$$\delta\rho \simeq \varepsilon \left[\frac{\rho}{\sin(\theta)} \right] \tag{4.49}$$

where ρ is the relative distance between the two spacecraft and $\delta\rho$ is the range uncertainty. Equation (4.49), shows the estimation uncertainty for the range is affected by three factors: the measurements noise ε, the relative distance ρ and the observability angle θ. Therefore, there are three distinct ways to minimise the uncertainty. The first is to improve the sensor accuracy. However, there are physical and technological limitations to the minimum achievable value for ε. On the other hand, one of the major benefits of bearing-only solutions is that they only require a camera to work, meaning great economic savings in terms of hardware. Thus, requiring very accurate sensors would simply deny them any advantage.

The remaining options are to bring the chaser closer to the target or perform a maneuver that increases the observability angle. In this regard, the range uncertainty is minimised when θ reaches 90 degrees. Namely, when the LOS vector of the perturbed trajectory is perpendicular to the one of the natural dynamics. A visual representation of the range estimation sensitivity at varying values of the observability angle is represented in Figure 4.9.

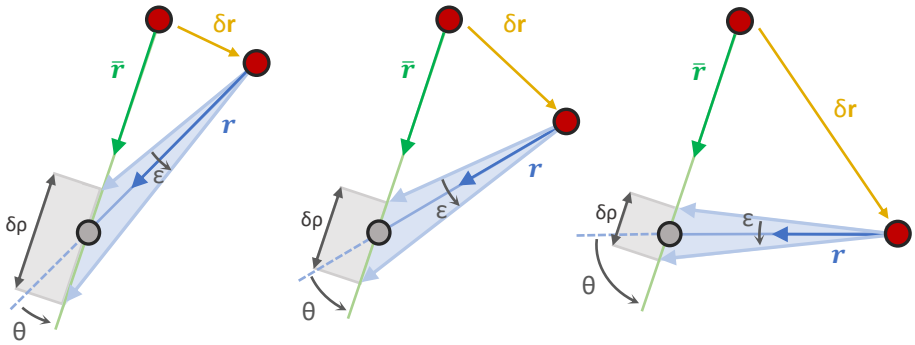

FIGURE 4.9: Range uncertainty sensitivity to the observability angle θ, for fixed relative distance and sensor accuracy.

For typical rendezvous applications, a useful design parameter is the *relative range uncertainty*. Indeed, to evaluate whether or not a specific absolute error is acceptable, one should check the relative distance between the two spacecraft. A range uncertainty of 1 km can be extremely good if the chaser is 500 km or unacceptable if the distance is only 10 km. A classical rule-of-thumb is to set the threshold for the relative error to 0.01; that is, a one-percent accuracy [49]. An expression for this metric is easily obtained from (4.49) as:

$$\frac{\delta\rho}{\rho} \simeq \frac{\varepsilon}{\sin(\theta)} \tag{4.50}$$

This criterion clearly shows that in order to reduce the relative range estimation error, the design of the trajectory should focus on maximising the observability angle θ. From this perspective, reducing the relative distance is not convenient anymore. Indeed, although (4.49) showed that it was a viable alternative to improve the absolute uncertainty, an optimisation algorithm based on that criterion could solve for

a maneuver that reduces ρ while keeping θ very small. If that was the case, the resulting trajectory would most likely violate any threshold on the relative range uncertainty.

Since (4.49) and (4.50) have been obtained without making any reference to the navigation filter, one should check whether or not these criteria are good indicators for the filter uncertainty. Thus, to evaluate the navigation performance, a Monte Carlo simulation has been set up, varying the initial state of the filter and the sensor noise. The real dynamics is modelled with the CR3BP whereas the linear approximation is exploited by the EKF. The chaser performs an impulsive maneuver at the initial time and the direction of $\mathbf{u}$ has been obtained through a non-linear optimizer using as objective (4.51). Figure 4.10 shows the resulting relative position errors for 500 simulations of the relative dynamics in proximity of the LOP-G orbit.

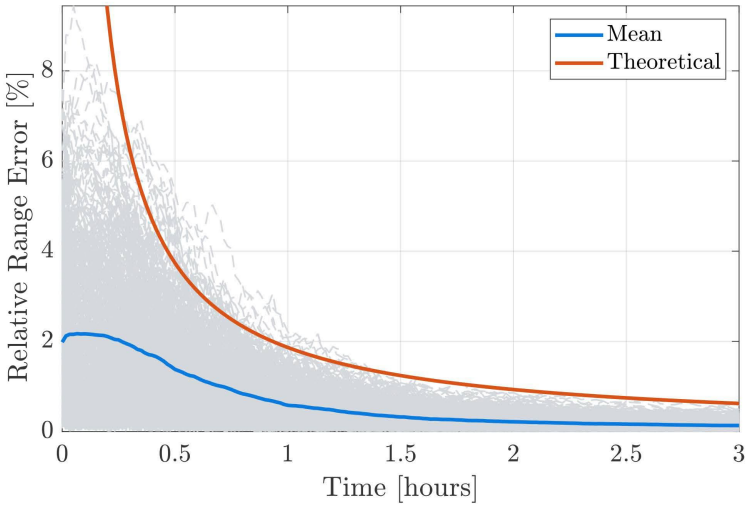

FIGURE 4.10: Theoretical relative range uncertainty prediction performance. The gray lines represent each individual simulation. The maneuver is performed at the initial time. The update time is 1 Hz.

It stands clear that the relative uncertainty metric marks the outer boundary of the navigation errors envelope, whereas the 1-σ mean error is well below the threshold. This is explained by recalling that the previous geometric considerations assumed an infinite initial uncertainty. However, in a practical implementation, the navigation filter is initialised with a finite covariance uncertainty, therefore it is to be expected that the errors will be smaller than the ones predicted by the relative metric. Moreover, it was acknowledged that the errors immediately following the maneuver could be higher than expected when the update frequency of the filter is low. Overall, it appears that (4.50) is a valid measure for the worst possible navigation performance once the filter has reached convergence. Thus, if a requirement on the maximum admissible error is given and the sensor accuracy is known, this metric is easily inverted to find the observability angle necessary to satisfy the demands. Viceversa, if the maximum value of θ is constrained, the same relationship can be exploited to find the needed accuracy for the on-board cameras.

It is interesting to evaluate what happens when a second maneuver is performed. Specifically, one could question whether the second impulse should maximise the angle with the original dynamics θ or with the natural evolution of the chaser after

the maneuver was performed, here denoted φ. In this regard, both directions have been tested and the performance are respectively reported in Figure 4.11. To clear any doubts, in the second scenario, the direction was chosen to ensure that φ is maximised while θ is minimised. From the right plot, it is evident that when θ becomes constant the range uncertainty no longer improves, even though φ is increased. On the other hand, a constant reduction of the estimation error is guaranteed when θ continuously rises.

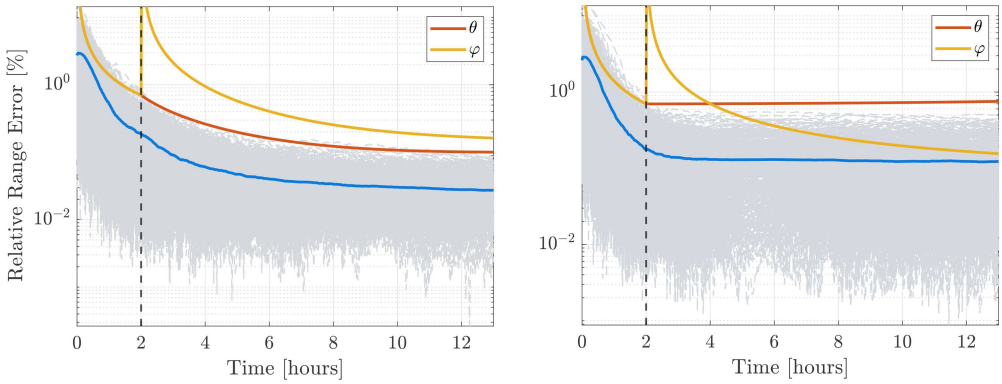

(*a*) Maximisation of θ.

(*b*) Maximisation of φ.

FIGURE 4.11: Comparison between different directions for the second maneuver, performed at the dashed black line. The yellow and red lines are the relative error metrics associated to the two angles. A logarithmic scale is employed to better highlight the estimation errors at the final times.

These simulations confirm that what matters most is the observability angle of the perturbed trajectory with respect to the original evolution of the dynamics, regardless of how many maneuvers are performed in-between. As a consequence, this peculiar behaviour can be exploited to design rendezvous trajectories that naturally maximise θ. Suppose the bearing-only navigation is employed to close the gap between a far-range distance (e.g., 500 km) and a fixed 1 km close-proximity hovering point. If the rendezvous time T_{rdv} is also constrained, one can find an initial optimal point at 500 km, whose natural dynamics at T_{rdv} is as perpendicular as possible to the desired final position vector. Although this does not ensure the error is below the one-percent threshold throughout the whole rendezvous trajectory, it guarantees the final navigation uncertainty will always satisfy the constraints.

4.3.2 Search for Optimal Observable Maneuvers

When bearing-only is used for a rendezvous mission, the trajectory profile should allow to minimise the navigation error. The previous section established what are the key elements that ensure a maneuver yields maximum observability and validated a metric for the navigation filter performance. The concept of observability angle could be exploited to classify a maneuver as either optimal or not, depending on the value reached by θ. A simple expression for the optimisation objective would then be:

$$\mathcal{J}_\theta = \cos^2(\theta) = \left[\frac{(\mathbf{\Lambda x}_1)^T(\mathbf{\Lambda x}_1 + \mathbf{\Gamma u})}{\|\mathbf{\Lambda x}_1\|\|\mathbf{\Lambda x}_1 + \mathbf{\Gamma u}\|}\right]^2 \tag{4.51}$$

where the discrete-form solution of the linear model is employed to ease the computations. However, equation (4.51) cannot be solved by linear or quadratic programming algorithms because the maneuver $\mathbf{u}$ (i.e., the independent variables) enters in both the numerator and denominator. Moreover, for the very same reason it does not admit a closed-form solution either. Such explicit analytical expression for the optimal maneuver is desirable because it would grant the usage of minimisation algorithms that guarantee a solution in polynomial time. Thus, allowing the implementation of the same concept for both large spacecraft and small satellites with limited computational power. With this in mind, [12] proposed a continuous measure of observability that admits an explicit closed-form solution applicable to any type of maneuver and trajectory. Therefore, the objective is now to investigate whether or not this kind of analytic optimal maneuvers yield the best improvement of the navigation estimate when applied to the non-keplerian dynamics.

In this framework, the objective function to minimise has been derived starting from the sufficient condition for observability, that is the *positive linear independence* of the perturbed trajectory ($\mathbf{\Lambda x}_1 + \mathbf{\Gamma u}$) and the natural evolution ($\mathbf{\Lambda x}_1$). An optimal maneuver would then be one that ensures the orthogonality (independence) of the two vectors while simultaneously ensuring the positive nature of their relationship. However, it can be proved that these two conditions cannot be satisfied simultaneously and when possible, the maneuver would simply bring the chaser to the exact position of the target. For this reason the proposed optimisation objective "maximises" the positive linear independence, without necessarily requiring the two vectors to be orthogonal. Mathematically:

$$\mathcal{J}_o(\mathbf{u}, t) = (\mathbf{\Lambda x}_1)^T(\mathbf{\Lambda x}_1 + \mathbf{\Gamma u}) \quad \text{subject to} \quad \mathcal{J}_o(\mathbf{u}, t) > 0 \tag{4.52}$$

Physically, whenever this constraint is not satisfied, the chaser finds himself on the opposite side of the target with respect to where he would have been without the maneuver. Note that this objective is quite similar to (4.51), but the key difference is that $\mathcal{J}_o$ can be minimised by either changing the angle between the two vectors (i.e., θ) or reducing their magnitude (i.e., moving closer to the target). However, as said previously this last alternative does not always guarantee a reduction of the error or the satisfaction of the relative error threshold. Although in the LEO scenario this dissimilarity did not raise any concerns (the maneuvers effectively provided the best minimisation of the error), the peculiar nature of rendezvous operations in the cislunar domain will cause remarkable differences with respect to the other dynamic environment.

Notice that $\mathcal{J}_o$ is function of both the maneuver $\mathbf{u}$ as well as time, which enters the equation through the matrices $\mathbf{\Lambda}$ and $\mathbf{\Gamma}$. In a real operation, the space of admissible maneuvers is constrained by the engine characteristics and by the amount of onboard propellant. Therefore, an additional constraint has been added to (4.52) to limit the maximum magnitude of $\mathbf{u}$. An explicit solution that minimises $\mathcal{J}_o$ can be found by means of Langrange multipliers and the Karush-Kuhn-Tucker (KKT) optimality conditions. The resulting algebraic expression for the optimal maneuver direction is (see [12] for the full derivation):

$$\mathbf{u}_{opt} = -m\frac{\mathbf{\Gamma}^T(\mathbf{\Lambda x}_1)}{\sqrt{(\mathbf{\Lambda x}_1)^T\mathbf{\Gamma\Gamma}^T(\mathbf{\Lambda x}_1)}} \tag{4.53}$$

where m is amplitude of the maneuver. To validate this expression, multiple Monte Carlo simulations have been performed in proximity of the LOP-G orbit. Since the objective is to prove that $\mathbf{u}_{opt}$ effectively yields the best improvement of the navigation estimate, its performance have been compared with those of other maneuver directions (uniformly distributed on a sphere of radius m). To easily asses whether the optimal maneuver improves or deteriorates the estimation error, the mean navigation error of the trajectory without maneuvers (i.e., the natural evolution) has been subtracted to that of all the other directions. According to this process, a negative value would then imply the maneuver direction improves the observability of the relative motion and viceversa when the result is positive.

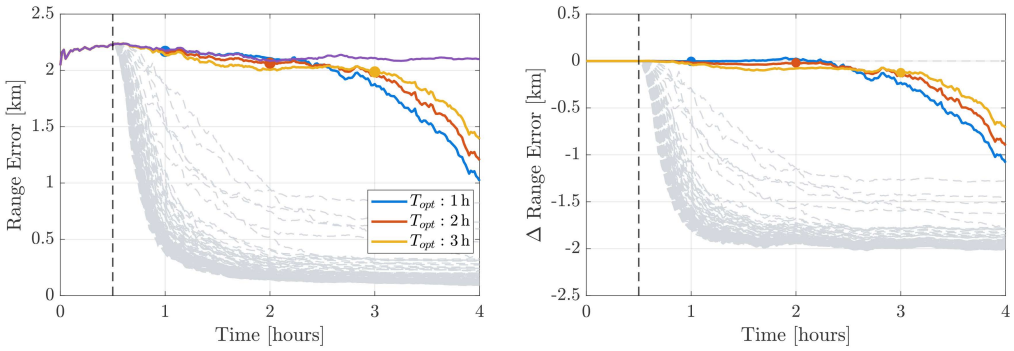

(*a*) Navigation error. (*b*) Navigation error improvement.

FIGURE 4.12: Optimal maneuvers performance in terms of navigation error. The maneuvers are performed at the dashed black line; the violet line represents the errors of the natural evolution. The dotted points are the optimal maneuvering times.

Some interesting results have come out from the simulation. Figure 4.12 clearly indicates that the so-called "optimal maneuvers" are completely uncapable of providing the best improvement of the navigation estimate. Moreover, it almost looks like the corresponding trajectories are unobservable for most of the simulation time as they display little to no differences with respect to the error of the trajectory with no maneuvers at all (the violet line). Figure 4.13a shows that the objective $\mathcal{J}_o$ is effectively minimised by these optimal maneuvers. Thus, the reasons for the bad filter performance are not due to modelling or mathematical errors but rely on the inability of the proposed optimisation objective to yield observability.

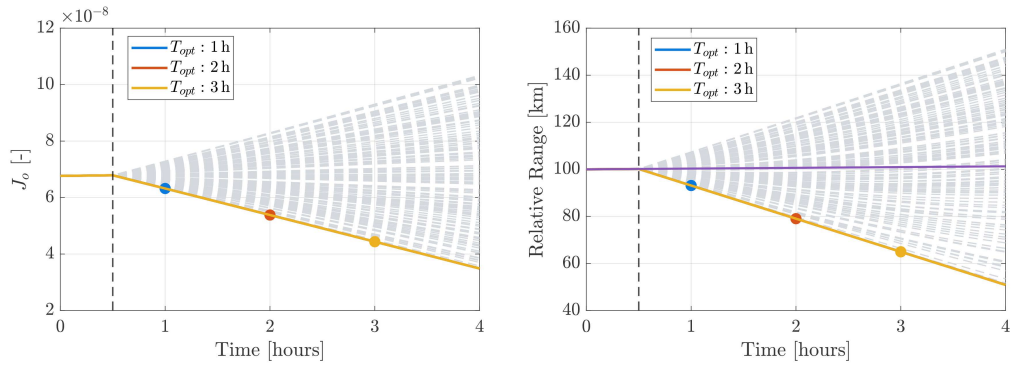

(*a*) Optimisation objective. (*b*) Relative range.

FIGURE 4.13: Characteristics of each maneuver direction.

Recall that the navigation uncertainty in (4.49) depends on two variables: the relative range and the observability angle (sensor errors are currently neglected because they affect in equal way all these trajectories). From Figure 4.13b it appears that these optimal maneuvers are the ones that bring the chaser closer to the target. Nonetheless, a significant improvement in the error happens only when the relative distance is reduced of almost 40 km, implying that a possible one-percent accuracy threshold would be violated for half the trajectory. These simulations are a clear example of the concept mentioned earlier. That is, an objective function that includes information on the range can be minimised by simply reducing the relative distance rather than acting on the observability angle. As shown by Figure 4.14a, the maneuvers coming from the minimisation of $\mathcal{J}_o$ have an observability angle that is close to 0 for almost 2 hours, only then the navigation uncertainty improves. Therefore, although the trajectories associated to these maneuvers minimise the range, the navigation errors cannot be improved because their degree of observability is extremely low.

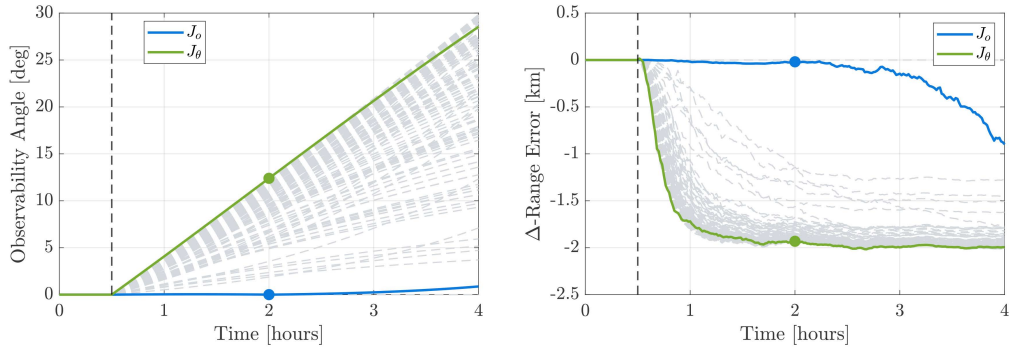

(*a*) Observability angle. (*b*) Navigation error improvement.

FIGURE 4.14: Comparison between optimisation objectives. The blue line ideally represents the optimal maneuver at 2 hours.

In this regard, a simple comparison between the two optimisation objectives $\mathcal{J}_o$ and $\mathcal{J}_\theta$ was performed in Figure 4.14b. It is clear that the best improvement is obtained when the maneuver maximises the observability angle.

Having acknowledged that, additional analyses have been performed in LEO, where [12] has proved these analytical optimal maneuvers work as expected. Interestingly, depending on the initial conditions, and so on the nature of the relative natural motion, these maneuvers either provide some of the best or worst navigation estimates, showcasing that $\mathcal{J}_o$ is not reliable as a measure of observability. The same investigation was carried out in the cis-lunar domain but unfortunately, it was not possible to find any realistic initial condition for $\mathcal{J}_o$ to work properly. The comparison between the two space environments suggests this has to do with the peculiar nature of the CR3BP relative dynamics. Specifically, while in LEO a rendezvous approach may last for several periods of the target's orbit, in the non-keplerian domain the orbital periods are in the order of days if not weeks. Define $\mathcal{T}$ the ratio between the typical duration of the rendezvous and the orbital period, then:

$$\mathcal{T}_{LEO} \gg 1 \quad \text{and} \quad \mathcal{T}_{CR3BP} \ll 1 \tag{4.54}$$

This difference implies that the relative natural dynamics is much slower in the cis-lunar domain than it is in LEO. When that is the case, it seems that to optimise $\mathcal{J}_o$ it

is more convenient to act on the range rather than on the observability angle. Overall, this raises serious doubts on the effectiveness of this observability measure for bearing-only applications in the cislunar domain. On the other hand, $\mathcal{J}_\theta$ successfully allowed to identify the maneuver directions that yield the best improvement in the navigation estimate, although its expression is not compatible with a linear nor quadratic formulation.

Chapter 5

Shrinking Horizon Bearing-Only Guidance

The primary objective of standard techniques for the design of rendezvous trajectories is to minimise either the fuel consumption or the time duration of the operation (or a combination of both). In this regard, many strategies are available and can be classified on the basis of their optimisation method. A common denominator among them is that, as long as the trajectory guarantees that measurements are available, the navigation performance is not actively considered during the planning phase. However, when dealing with a bearing-only architecture, the navigation process is directly influenced by the shape of the trajectory and, as shown in the previous chapter, the range uncertainty can only be reduced through a precise set of observable maneuvers.

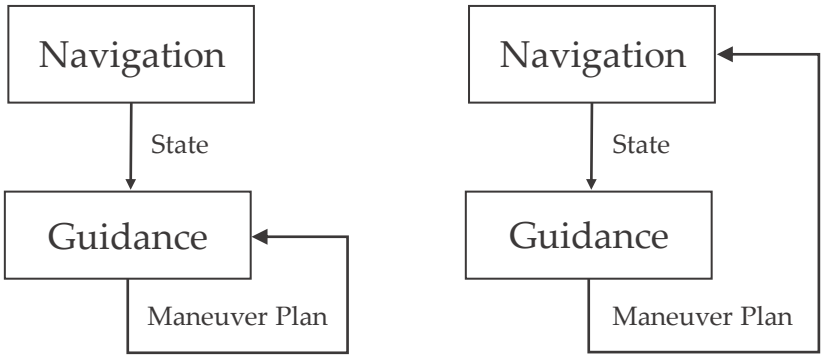

FIGURE 5.1: Comparison between a standard rendezvous planning scheme (*left*) and a bearing-only application (*right*). Image adapted from [50]

This concept is well illustrated in the figure above. The left side shows the traditional approach where the relative state estimate coming from the navigation filter is the primary input of the guidance algorithms. The computed trajectory will then be affected by inherent errors due to the navigation uncertainties; thus, the maneuver plan must be periodically updated to ensure the spacecraft reaches its final destination point. Notice that if the estimation and modelling errors were null, a periodic check (and eventually an update) of the control action would be required nonetheless because of possible malfunctions of the actuators. Depending on the type of sensors used, the state uncertainty decreases with the distance from the target, so that at the final stages the position error is minimised.

On the other side, for a bearing-only application, the navigation uncertainty can only be reduced through specific maneuvers that enhance the observability of the system.

As shown previously, decreasing the range is not a sufficient condition to ensure the navigation estimate improves. Clearly if the range error constantly remains above the one-percent threshold, the final position dispersion will never satisfy the operational constraints, no matter how many times the guidance problem is solved. Therefore, it is mandatory to include, inside the trajectory design, a contribution that allows to improve the navigation performance. This last consideration justifies exactly the need for a measure of the system observability.

With this in mind, the goal of this chapter is to provide a mathematical description of the spacecraft guidance, highlighting how already existing fuel-optimal techniques can be enhanced to account for the navigation performance in the design of a non-keplerian trajectory. Initially, it provides an overview of the Shrinking Horizon - Model Predictive Control (SH-MPC) strategy used to compute feasible rendezvous trajectories. The objectives to account for fuel consumption and to enhance the bearing-only observability are discussed and different formulations are presented for each of them. Concerning the observability, the quadratic objective already proposed in [13] is generalised to any discrete-time system and a linear alternative is suggested. A small survey of multi-objective optimisation techniques is reported to select the most suitable option for the case at hand, on the basis of a bunch of relevant criteria. Additionally, it is shown how different constraints can be included to account for systems engineering limitations, such as the maximum thrust available from the engines, and how the same problem formulation can be exploited for multiple proximity operations. Finally, on the basis of the previous chapter results, an alternative non-linear formulation to generate observable trajectories is proposed.

5.1 Shrinking Horizon - Model Predictive Control

A Model Predictive Control (MPC) can be classified as an optimal control strategy that relies on a repeated on-line constrained optimisation of a series of control actions based on the prediction of the dynamics. In particular, throughout the last decade, this technique has been exploited by many research studies to improve the degree of autonomy of a spacecraft during a rendezvous operation. For this work, a Shrinking Horizon - MPC architecture has been chosen to compute the maneuvers required to bring the spacecraft to a desired location. In this alternative formulation, the trajectory is discretised into a series of n points, arbitrarily spaced in time. However, differently from a standard MPC approach, with a *shrinking horizon* the rendezvous duration is fixed and the problem is always solved from the current epoch until the final time, thus the time window *shrinks* at each re-optimisation according to the remaining rendezvous time. Two main reasons are behind the selection of this strategy. First, it opens the possibility for a direct comparison with the results that [13] obtained with the same bearing-only architecture; establishing a baseline for angles-only navigation in the cis-lunar space. In addition, as the design of a trajectory is always a trade-off between fuel usage and time required, it would allow to investigate the sensitivity of the solution to a different number of perturbing actors and model approximations, leaving time as an a-priori fixed design variable.

The course of action for this kind of architecture is as follows. Calling T_{rdv} the desired rendezvous time, the trajectory is discretised into n steps $t_M = [t_{M_1}, t_{M_2}, ..., t_{M_n}]$, and at each of those a maneuver is allowed. At the same time, the number m of re-optimisation performed along the trajectory is scheduled for $t_O = [t_{O_1}, t_{O_2}, ..., t_{O_m}]$ and is such that t_{O_i} does not necessarily equal t_{M_i}. Once the guidance is initialised,

for each update time t_j it checks whether an optimisation is planned at the current epoch. If that is the case, the minimisation algorithms sets the estimated relative state as the initial point and searches a solution for the remaining discretisation points, eventually updating the maneuver scheme $\mathbf{U}_{opt}$. Afterwards, it also controls if a maneuver is planned; whenever that is the case, the chaser executes the control action according to $\mathbf{U}_{opt}$. Finally, the cycle is stopped when T_{rdv} is reached. The whole scheme is summarised as a simple flow-chart in Fig. 5.2.

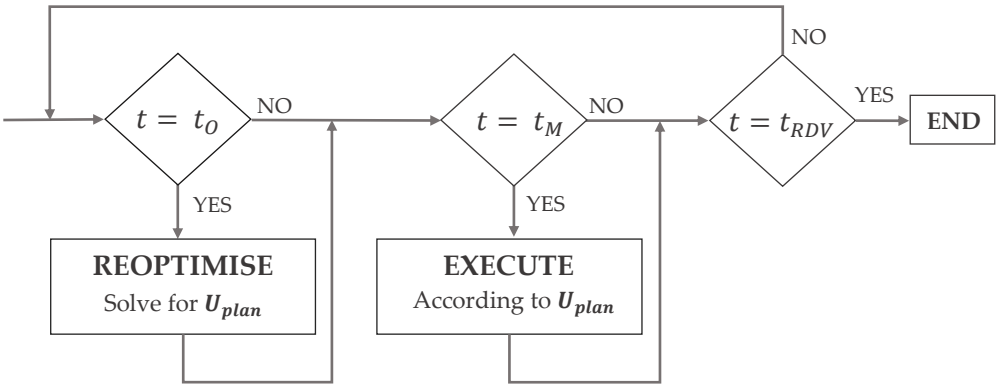

FIGURE 5.2: Guidance Flow-chart.

t_o and t_M are the epochs when re-optimisations are planned and maneuvers are allowed, respectively. At each time step t the on-board CPU checks if a re-optimisation is planned, if that is the case it solves the optimisation problem and updates the maneuver plan $\mathbf{U}_{plan}$. Then, the computer also controls whether a maneuver should be performed. The algorithm is stopped when the current epoch t equals the designed rendezvous time t_{RDV}.

Please notice that in a real implementation, it might not be feasible to solve the optimisation problem and execute a maneuver at the exact same epoch. Nevertheless, it is here assumed that the two tasks can be accomplished simultaneously.

5.1.1 Optimisation Problem

Theoretically, inside an MPC, any type of solver can be used to deal with the optimisation problem, from simple deterministic methods to more complex heuristic ones (e.g., genetic algorithms). Thus, since an analytical solution is not necessarily required, any type of constraint and cost function can be exploited for the design of the approach trajectory. These higher degrees of freedom are one of the reasons why a MPC generally outperforms the competition (e.g., artificial potential methods). On the other hand, the greater level of flexibility makes it computationally heavier when compared to more basic control methods. In this regard, the time-interval between two successive re-optimisations is limited by the specifics of the on-board CPU. Indeed, even though during a far-range approach maneuvers are performed only every now and then, other tasks might require a computational priority and thus, limit the time available to solve the optimisation problem.

For this reason, it is desirable to have a linear time-invariant or time-varying model to approximate the dynamics of the spacecraft motion. This representation would allow to formulate the optimisation problem in such way that Linear Programming (LP) and Quadratic Programming (QP) algorithms can be used to find an optimal

solution. Their major benefit is that, if the problem is feasible, a result is guaranteed in polynomial time with no particular demands in terms of available computational power. This property is very appealing because it would allow for the same guidance scheme to be implemented over a broad class of satellites, from cubesats to large spacecraft. Specifically, the time required by LP and QP algorithms directly depends on the number of variables, i.e., on the discretisation step.

With this in mind, most works in LEO exploit the exact closed-form solution of CW's equations to adopt a wide time-interval between the points and limit the number of independent variables. Once again, such closed-form solution does not exist in the non-keplerian domain and the numerical integration of the relative dynamics would not be compatible with a LP/QP formulation. Nevertheless, the analysis of section 2.5.2 proved that the discrete-form of the linearised relative non-keplerian dynamics has a high degree of accuracy for classical rendezvous times. Therefore, it is here exploited to predict the future evolution of the trajectory and lower the computational demands. In this regard, the results of this section will demonstrate that the linearised model is very well suited for an efficient MPC implementation in the cis-lunar domain.

As a last remark, CW's equations might be viewed as an exact solution to a wrong problem, because the effects of dynamical perturbations (e.g., air drag, SRP, higher gravitational harmonics, Luni-solar perturbations, etc...) are neglected. Thus, it could be reasonable to assume that the adoption of the linearised non-keplerian relative model for the cis-lunar domain is as good of an approximation as CW's equations are for the LEO scenario.

The structure of the resulting optimisation problem is summarised as:

$$\min_{\mathbf{y}} \quad \mathcal{J}_c(\mathbf{y}) \tag{5.1a}$$

$$\text{subject to} \quad \mathbf{A}_{eq}\mathbf{y} = \mathbf{b}_{eq} \tag{5.1b}$$

$$\mathbf{A}_{iq}\mathbf{y} \leq \mathbf{b}_{iq} \tag{5.1c}$$

$$\mathbf{l}_b \leq \mathbf{y} \leq \mathbf{u}_b \tag{5.1d}$$

where $\mathbf{y}$ is the vector of independent variables, containing the maneuvers directions and, possibly, other associated quantities. $\mathbf{A}_{eq}$ and $\mathbf{A}_{iq}$ are the matrices that express the equality and inequality constraints, respectively. These are used to bound the relative motion to specific regions of space and specify the boundary conditions; namely, the initial and final points of the trajectory. $\mathbf{l}_b$ and $\mathbf{u}_b$ are the lower and upper bounds for the solution space of $\mathbf{y}$ and allow to include inside the problem the system engineering limitations (e.g., the maximum thrust available). Finally, $\mathcal{J}_c$ is the objective to minimise and will include linear or quadratic contributions of the observability metric and fuel consumption. The following sections illustrate how to assemble each of the matrices and vectors that enter in the optimisation problem (5.1). Notice that, depending on the expression for the fuel objective, the structure of $\mathbf{y}$ (and of the other matrices) is subject to some slight changes.

To clarify the future notation, the dynamics is expressed according to (2.40) and the state transition matrix $\mathbf{\Phi}$ is computed with one of the approximations in Table 2.2. For the input, it is here supposed that the convolution integral can be expressed as the product between a matrix $\mathbf{G}$ and $\mathbf{u}$; thus, this formulation is valid for both impulsive and constant-thrust maneuvers. Additionally, since (2.40) does not make any

assumption on the model used to propagate the target absolute dynamics, the guidance is straightforwardly adapted to work in the CR3BP or with the Ephemerides.

According to the previous notation, given the vector of n discretised maneuvering times $t_M = [t_1, t_2, ..., t_n]$, the matrices for the trajectory evolution from t_{k-1} to t_k are written as:

$$\begin{aligned} \mathbf{x}_k &= \mathbf{\Phi}_{k-1}\mathbf{x}_{k-1} + \mathbf{G}_{k-1}\mathbf{u}_{k-1} \\ \mathbf{r}_k &= \mathbf{\Lambda}_{k-1}\mathbf{x}_{k-1} + \mathbf{\Gamma}_{k-1}\mathbf{u}_{k-1} \end{aligned} \tag{5.2}$$

where $\mathbf{r}_k$ is the relative position vectors and $\mathbf{x}_k$ the complete state. The matrices $\mathbf{\Lambda}_k$ and $\mathbf{\Gamma}_k$ are easily computed as:

$$\mathbf{\Lambda}_k = \begin{bmatrix} \mathbf{I}_3 & \mathbf{0}_3 \end{bmatrix} \mathbf{\Phi}_k \qquad \mathbf{\Gamma}_k = \begin{bmatrix} \mathbf{I}_3 & \mathbf{0}_3 \end{bmatrix} \mathbf{G}_k \tag{5.3}$$

Assuming the time-interval is discretised in n points, the relative states can be collected inside a vector $\mathbf{X} = [\mathbf{x}_1^T \ \mathbf{x}_2^T \ ... \ \mathbf{x}_n^T]^T$ of size $6n \times 1$. At the same time, the maneuvers are admissible at every point but the last one, otherwise an additional relative state would be produced. Thus, in a similar fashion they are collected inside a global vector $\mathbf{U} = [\mathbf{u}_1^T \ \mathbf{u}_2^T \ ... \ \mathbf{u}_{n-1}^T]^T$ of size $3(n-1) \times 1$. Generally speaking, the usefulness of this formulation of the optimisation problem is that it holds for any dynamic system that can be approximated with a discrete-time solution of this form.

5.2 Fuel Objective

The classical parameter used to quantify the performance of a trajectory in terms of fuel cost is the ΔV. Through Tsiolkovsky's formula, the resulting value can be directly used to estimate the fuel mass required for the transfer and check whether the solution is feasible from an engineering standpoint. Unfortunately, the ΔV cannot be expressed as a linear or quadratic combination of the optimisation variables as it involves a square root by definition. Two workarounds are commonly used in MPC implementations and are here reported.

5.2.1 Quadratic Control

The most common approach is to exploit a cost function $\mathcal{J}_{F_q}$ that is quadratic on control effort, written in function of $\mathbf{U}$ as [26]:

$$\mathcal{J}_{F_q} = \frac{1}{2}\mathbf{U}^T \mathcal{Q} \mathbf{U} \tag{5.4}$$

where $\mathcal{Q}$ is a $3(n-1) \times 3(n-1)$ diagonal weighting matrix. By changing the elements along the diagonals one can either prioritise or penalise the maneuvers associated to certain epochs. In addition, when combined with the observability objective, it is possible to produce trajectories that favour observability at the cost of additional fuel consumption (or vice-versa) by equally scaling all the components of this matrix. Nevertheless, in this work $\mathcal{Q}$ has always been set equal to the identity matrix and additional weight factors are used to cope with the multi-objective optimisation.

The adoption of a quadratic fuel objective usually guarantees a smooth control action and the resulting dynamics is more robust to disturbances and off-nominal conditions [25]. To analyse its performance, $\mathcal{J}_{F_q}$ can be related to the ΔV of the solution

by taking the products in (5.4) and assuming $\mathcal{Q} = \mathbf{I}$:

$$\mathcal{J}_{F_q} = \frac{1}{2}\sum_{k=1}^{n-1}(\Delta V_k)^2 \tag{5.5}$$

Physically, the equation shows that $\mathcal{J}_{F_q}$ is equal to the sum of the squares of the ΔV required by each maneuver. As a consequence, since the ΔV is directly proportional to the control action, the solutions coming from the minimisation of this cost function may not be optimal in terms of overall fuel consumption (see Figure 6.2 for a visual proof). As a final remark, whenever this cost function is used, the optimisation vector $\mathbf{y}$ in (5.1) is equal to the global maneuver vector $\mathbf{U}$ for the fuel-optimal trajectory; if observability is included, $\mathbf{U}$ is augmented with one unitary element (see section 5.3 for further details).

5.2.2 Slack Variables

A more realistic representation of the fuel expenditure can be obtained by adopting a so-called 1-norm objective; that is, the sum of the absolute values of all thrust elements inside $\mathbf{U}$:

$$\mathcal{J}_{F_s} = \sum_{k=1}^{n-1}\sum_{j=1}^{3}|\mathrm{U}_{kj}| \tag{5.6}$$

This class of cost function generally yields solutions with smaller ΔV when compared to the previous quadratic objective. Additionally, the maneuver plan is characterised by sparser control actions that are quite appealing when a continuous-thrust system is not available. However, the downside of having few maneuvers is that, if the control schedule is not executed properly, the trajectory may be subject to large deviations from the original plan.

The objective in (5.6) is a piece-wise linear function and must be properly converted before being implemented inside a LP/QP algorithm. Therefore, a new set of variables $\mathbf{S} = [\mathbf{s}_1^T\ \mathbf{s}_2^T\ ...\ \mathbf{s}_{n-1}^T]^T$, called *slack variables* [13] is introduced inside the optimisation vector $\mathbf{Y}$. Then, by adding specific inequality constraints, each of the elements inside $\mathbf{S}$ can be set equal to the absolute value of the corresponding element in $\mathbf{U}$. Defining $\mathbf{Y} = [\mathbf{U};\ \mathbf{S}]$ the augmented optimisation vector, the cost function in (5.6) is written as:

$$\mathcal{J}_{F_s} = \mathbf{F}^T\mathbf{Y} \tag{5.7}$$

where the vector $\mathbf{F}$ has the first $3(n-1)$ elements equal to zero and the remaining set to one. To ensure $\mathbf{S}$ equals the absolute value of $\mathbf{U}$, each j-element must be subject to the following two constraints:

$$\begin{aligned}\mathbf{U}_j - \mathbf{S}_j &\leq 0\\ -\mathbf{U}_j - \mathbf{S}_j &\leq 0\end{aligned} \tag{5.8}$$

It is easy to prove that when these constraints are simultaneously satisfied, $\mathbf{S} = |\mathbf{U}|$. The system (5.8) is generalised to every maneuver by expressing all the individual constraints through a matrix as:

$$\mathbf{A}_s\mathbf{Y} \leq \mathbf{b}_s \tag{5.9}$$

where $\mathbf{A}_s$ and $\mathbf{b}_s$ are written as:

$$\mathbf{A}_s = \begin{bmatrix}\mathbf{I}_m & -\mathbf{I}_m\\ -\mathbf{I}_m & -\mathbf{I}_m\end{bmatrix} \qquad \mathbf{b}_s = \mathbf{0}_{2m} \tag{5.10}$$

with $m = 3(n-1)$. Notice that, even though the number of variables required by this cost function doubles that of the previous expression, $\mathcal{J}_{F_s}$ is linear in $\mathbf{Y}$ and can be solved in a shorter time with LP algorithms.

5.3 Observability Objective

The previous chapter investigated two observability metrics, $\mathcal{J}_\theta$ and $\mathcal{J}_o$, which are here recalled from (4.51) and (4.52):

$$\mathcal{J}_\theta = \cos^2(\theta) = \left[\frac{(\mathbf{\Lambda x}_1)^T(\mathbf{\Lambda x}_1 + \mathbf{\Gamma u})}{\|\mathbf{\Lambda x}_1\|\|\mathbf{\Lambda x}_1 + \mathbf{\Gamma u}\|}\right]^2 \qquad \mathcal{J}_o = (\mathbf{\Lambda x}_1)^T(\mathbf{\Lambda x}_1 + \mathbf{\Gamma u}) \tag{5.11}$$

The analyses in section 4.3.2 highlighted that the angle θ proved a very promising criterion to quantify the observability. However, it stands clear that a dedicated cost function (i.e., $\mathcal{J}_\theta$) cannot be expressed as a linear or quadratic combination of the optimisation variables because they are found at both sides of the fraction. As a consequence, such objective is not compliant with the structure of the optimisation problem under study in (5.1). Nevertheless, since the results coming from this cost function seemed very encouraging, a different formulation of the MPC problem is later proposed in section 5.6 to account for the observability angle θ.

In order to keep the observability objective in a linear or quadratic form, the same approach of [13] is here exploited. The observability is measured on the basis of $\mathcal{J}_o$, properly adapting the expression to request observability at each discretisation time. Even though it was previously proved that the optimal maneuvers coming from the minimisation of this cost function are completely uncapable of providing observability, it is interesting to investigate the behaviour of the objective function when the geometry of the problem and the duration of the approach are constrained. In particular, the optimal solutions that were computed favoured a drastic reduction of the range rather than increasing the observability angle, resulting in a low-degree-of-observability motion. However, in multi-objective optimisation a single global solution that simultaneously minimises both objectives rarely exists, and whenever the two functions have opposite needs, the resulting solution will be a compromise. Therefore, it could be reasonable to assume that when the optimisation objective is a combination between $\mathcal{J}_o$ and the fuel cost, the optimal solution will favour a slower approach towards the target to limit the ΔV (for a fixed rendezvous time), fostering instead higher observability angles.

In addition, section 4.3.1 proved that to guarantee observability the control actions should maximise the angle between the actual trajectory and that associated with natural evolution of the initial conditions, regardless of the number of maneuvers performed in-between. Therefore, for a fixed rendezvous point $\mathbf{x}_{rdv}$ and time, the starting condition can be selected to yield a trajectory that naturally maximises θ while the chaser gets closer to $\mathbf{x}_{rdv}$. When this constraints are applied to the optimisation problem, it might be possible that $\mathcal{J}_o$ would also favour a higher observability angle, similarly to $\mathcal{J}_\theta$.

Bearing this in mind, the next section will show how the quadratic observability objective proposed in [11] can be generalised to linear time-varying systems. On the other hand, an alternative linear expression is proposed on the basis of the results in 4.3.1.

5.3.1 Quadratic Cost

The observability cost in (4.52) can be expanded by summing the values of this function at each optimisation step. The original measure is here reported to aid the readability of the next paragraph:

$$\mathcal{J}_o(\mathbf{u}) = \bar{\mathbf{r}}^T\mathbf{r} = (\mathbf{\Lambda x})^T(\mathbf{\Lambda x} + \mathbf{\Gamma u}) \tag{5.12}$$

For each discretisation step, the scalar product between the natural position vector $\bar{\mathbf{r}}_j$ and the perturbed position $\mathbf{r}_j$ should be added to $\mathcal{J}_o$. Taking the sum for every j-point:

$$\mathcal{J}_{o_q} = \sum_{j=2}^{n-1} \bar{\mathbf{r}}_j^T \mathbf{r}_j = \sum_{k=1}^{n-2} (\mathbf{\Lambda}_k \mathbf{x}_k)^T (\mathbf{\Lambda}_k \mathbf{x}_k + \mathbf{\Gamma}_k \mathbf{u}_k) \tag{5.13}$$

The subscript q is used to differentiate from the future observability metric. Notice that the initial and final points are excluded because their position is constrained by the problem. With respect to Figure 5.3, as a consequence of the discretisation, if the extremes are fixed there are no observability differences between the two trajectories on the left; thus, including them inside $\mathcal{J}_o$ would be pointless. On the other side instead, the position of the intermediate points can be properly adjusted to minimise the observability objective. According to (5.2) the position of the j-th point is obtained from $\mathbf{u}_{j-1}$ maneuver, thus only up to $n-2$ input terms enter in $\mathcal{J}_o$.

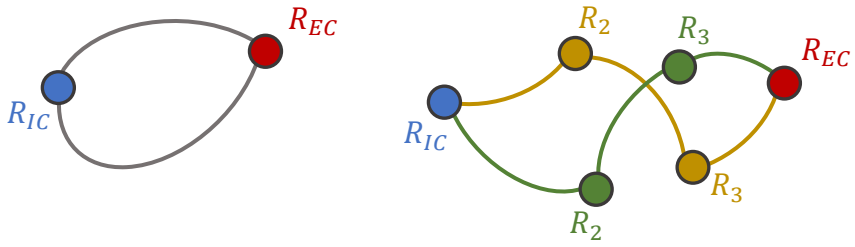

FIGURE 5.3: Observability objective discretisation. IC and EC denote the initial and final points, respectively.

To avoid including also the global position vector $\mathbf{X}$ inside the optimisation variables, the objective (5.13) must be re-formulated as function of the global maneuver vector $\mathbf{U}$ only. A few basic cases of $\mathcal{J}_o$ are here reported for different discretisation points n to better highlight how the expression can be generalised.

For $n = 3$:

$$\mathcal{J}_{o_3} = \mathbf{x}_1^T \mathbf{\Lambda}_1^T \mathbf{\Lambda}_1 \mathbf{x}_1 + \mathbf{x}_1^T \mathbf{\Lambda}_1^T \mathbf{\Gamma}_1 \mathbf{u}_1 \tag{5.14}$$

For $n = 4$:

$$\begin{aligned} \mathcal{J}_{o_4} = \mathcal{J}_{o_3} + \mathbf{x}_1^T \mathbf{\Phi}_1^T \mathbf{\Lambda}_2^T \mathbf{\Lambda}_2 \mathbf{\Phi}_1 \mathbf{x}_1 + 2\mathbf{x}_1^T \mathbf{\Phi}_1^T \mathbf{\Lambda}_2^T \mathbf{\Lambda}_2 \mathbf{G}_1 \mathbf{u}_1 + \mathbf{x}_1^T \mathbf{\Phi}_1^T \mathbf{\Lambda}_2^T \mathbf{\Gamma}_2 \mathbf{u}_2 \ ... \\ + \mathbf{u}_1^T \mathbf{G}_1^T \mathbf{\Lambda}_2^T \mathbf{\Lambda}_2 \mathbf{G}_1 \mathbf{u}_1 + \mathbf{u}_1^T \mathbf{G}_1^T \mathbf{\Lambda}_2^T \mathbf{\Gamma}_2 \mathbf{u}_2 \end{aligned} \tag{5.15}$$

For $n = 5$:

$$\begin{aligned}\mathcal{J}_{o_5} = \mathcal{J}_{o_4} &+ \mathbf{x}_1^T \mathbf{\Phi}_1^T \mathbf{\Phi}_2^T \mathbf{\Lambda}_3^T \mathbf{\Lambda}_3 \mathbf{\Phi}_2 \mathbf{\Phi}_1 \mathbf{x}_1 + 2\mathbf{x}_1^T \mathbf{\Phi}_1^T \mathbf{\Phi}_2^T \mathbf{\Lambda}_3^T \mathbf{\Lambda}_3 \mathbf{\Phi}_2 \mathbf{G}_1 \mathbf{u}_1 \ ... \\ &+ 2\mathbf{x}_1^T \mathbf{\Phi}_1^T \mathbf{\Phi}_2^T \mathbf{\Lambda}_3^T \mathbf{\Lambda}_3 \mathbf{G}_2 \mathbf{u}_2 + \mathbf{x}_1^T \mathbf{\Phi}_1^T \mathbf{\Phi}_2^T \mathbf{\Lambda}_3^T \mathbf{\Gamma}_3 \mathbf{u}_3 \ ... \\ &+ \mathbf{u}_1^T \mathbf{G}_1^T \mathbf{\Phi}_2^T \mathbf{\Lambda}_3^T \mathbf{\Lambda}_3 \mathbf{\Phi}_2 \mathbf{G}_1 \mathbf{u}_1 + \mathbf{u}_2^T \mathbf{G}_2^T \mathbf{\Lambda}_3^T \mathbf{\Lambda}_3 \mathbf{G}_2 \mathbf{u}_2 \ ... \\ &+ 2\mathbf{u}_2^T \mathbf{G}_2^T \mathbf{\Lambda}_3^T \mathbf{\Lambda}_3 \mathbf{\Phi}_2 \mathbf{G}_1 \mathbf{u}_1 + \mathbf{u}_1^T \mathbf{G}_1^T \mathbf{\Phi}_2^T \mathbf{\Lambda}_3^T \mathbf{\Gamma}_3 \mathbf{u}_3 + \mathbf{u}_2^T \mathbf{G}_2^T \mathbf{\Lambda}_3^T \mathbf{\Gamma}_3 \mathbf{u}_3 \end{aligned} \tag{5.16}$$

These expansions show that $\mathcal{J}_o$ can be re-written as a combination of a constant, linear and quadratic terms in $\mathbf{U}$ as:

$$\mathcal{J}_{o_q} = \frac{1}{2}\mathbf{U}^T \mathbb{H} \mathbf{U} + \mathbb{L}^T \mathbf{U} + \mathbb{C} \tag{5.17}$$

where

$$\begin{aligned} \mathbb{L} &= \begin{bmatrix} \mathbb{L}_1^T & \mathbb{L}_2^T & \dots & \mathbb{L}_{n-1}^T \end{bmatrix}^T \\ \mathbb{H} &= \begin{bmatrix} \mathbb{H}_{11} & \mathbb{H}_{21} & \dots & \mathbb{H}_{1(n-1)} \\ \mathbb{H}_{21} & \mathbb{H}_{22} & \dots & \mathbb{H}_{2(n-1)} \\ \vdots & \vdots & \ddots & \vdots \\ \mathbb{H}_{(n-1)1} & \mathbb{H}_{(n-1)2} & \dots & \mathbb{H}_{(n-1)(n-1)} \end{bmatrix} \end{aligned} \tag{5.18}$$

and $\mathbb{C}$ is a constant. Defining $m = 3(n-1)$, the dimensions of $\mathbb{L}$ and $\mathbb{H}$ are $m \times 1$ and $m \times m$, respectively. The subscripts for $\mathbb{L}_j$ refer to the three components of the vector associated with the maneuver $\mathbf{u}_j$: from the $(3j-2)$-th to the $3j$-th element of $\mathbb{L}$. The same notation is used with $\mathbb{H}_{ij}$, where the two indices refers to the row and column elements. Each of these terms is expressed as:

$$\begin{aligned} \mathbb{C} &= \mathbf{x}_1^T \left[\sum_{k=1}^{n-2} \mathbb{A}_{1k}^T \mathbf{\Lambda}_k^T \mathbf{\Lambda}_k \mathbb{A}_{1k} \right] \mathbf{x}_1 \\ \mathbb{L}_j &= \mathbf{x}_1^T \mathbb{A}_{1j}^T \mathbf{\Lambda}_j^T \mathbf{\Gamma}_j + 2\mathbf{x}_1^T \left[\sum_{k=j+1}^{n-2} \mathbb{A}_{1k}^T \mathbf{\Lambda}_k^T \mathbf{\Lambda}_k \mathbb{A}_{(j+1)k} \mathbf{G}_j \right] \\ \mathbb{H}_{ij} &= \mathbf{\Gamma}_i^T \mathbf{\Lambda}_i \mathbb{A}_{(j+1)i} \mathbf{G}_j (1 - \delta_{ij}) + 2 \left[\sum_{k=i+1}^{n-2} \mathbf{G}_i^T \mathbb{A}_{(i+1)k}^T \mathbf{\Lambda}_k^T \mathbf{\Lambda}_k \mathbb{A}_{(j+1)k} \mathbf{G}_j \right] \text{ for } i \geq j \end{aligned} \tag{5.19}$$

where δ_{ij} is the Kronecker delta and the matrix $\mathbb{A}$ is defined as:

$$\mathbb{A}_{ij} = \prod_{k=i}^{j-1} \mathbf{\Phi}_k \ \text{ if } j > i \qquad \text{and} \qquad \mathbb{A}_{ij} = \mathbf{I}_6 \ \text{ if } j \leq i \tag{5.20}$$

Due to the properties of $\mathbf{\Phi}$ (see section 2.32), this matrix equals the state transition matrix from step i to j. However, when $\mathbf{\Phi}_k$ is approximated with Table 2.2, the error introduced by evaluating $\mathbb{A}_{ij}$ with $\mathbf{x}_{t_i}$ and $\Delta t = (t_j - t_i)$ is much higher than that obtained by taking the product of each single STM. Finally, notice that the expression for $\mathbb{H}_{ij}$ is valid only for the lower-triangular portion of the matrix, the remaining half is obtained by exploiting the symmetry of $\mathbb{H}$. The following table summaries

the values of these matrices for different discretisation points.

Matrices	$n \leq 2$	$n = 3$	$n \geq 4$
$\mathbb{C}$	-	From (5.19a)	From (5.19a)
$\mathbb{L}$	-	From (5.19b)	From (5.19b)
$\mathbb{H}$	-	-	From (5.19c)

TABLE 5.1: Observability objective computation

Although it does not depend on $\mathbf{U}$, the computation of $\mathbb{C}$ is necessary to keep the observability objective positive and avoid unfeasible results when $\mathcal{J}_{o_q}$ is combined with the fuel cost function. Therefore, whenever $\mathcal{J}_{o_q}$ is introduced inside the optimisation problem, the decision vector $\mathbf{y}$ is augmented with one element constrained to a unitary value. The observability cost function in (5.17) is then written in terms of the optimisation vector $\mathbf{Y}$ as:

$$\mathcal{J}_{o_q} = \frac{1}{2}\mathbf{Y}^T\mathbb{H}_y\mathbf{Y} + \mathbb{L}_y^T\mathbf{Y} \tag{5.21}$$

with

$$\mathbb{H}_y = \begin{bmatrix} \mathbb{H} & \mathbf{0}_{m\times(p+1)} \\ \mathbf{0}_{(p+1)\times m} & \mathbf{0}_{(p+1)\times(p+1)} \end{bmatrix} \quad \mathbb{L}_y = \begin{bmatrix} \mathbb{L}^T & \mathbf{0}_{1xp} & \mathbb{C} \end{bmatrix}^T \tag{5.22}$$

where $p = 0$ if the quadratic fuel objective is used, otherwise $p = m$ when the slack variables are implemented. It is possible to prove that whenever the dynamic system is time-invariant, the resulting expressions are equal to those of [11].

The evaluation of $\mathbb{C}$, $\mathbb{L}$ and $\mathbb{H}$ from their definition in (5.19) is computationally expensive and denies any advantage coming from the LP/QP formulation. A clever procedure is to compute them by simultaneously adding the contribution of $\mathbf{u}_j$ to all three matrices and store the values of $\mathbb{A}_j$ for the next iteration. In this way, it also straightforward to adapt the algorithm to compute $\mathcal{J}_{o_q}$ only over a sub-set of the whole trajectory, such as in a traditional MPC implementation with a fixed size moving window.

As a last remark, in section 2.32 it was highlighted that the exact relative dynamics could be linearised around the position of the chaser rather than the target, so that only the knowledge of its absolute state would be required to navigate. Nevertheless, it was also suggested that it would not be convenient from a GNC/MPC perspective. The reasons can be well understood by looking at the definition of the matrices in the observability objective. Whenever this linearisation approach is adopted, $\mathbf{\Phi}$ and $\mathbf{G}$ are computed using the chaser position at each discretisation step. However, these states are dependent on the maneuvers so that a change in the control action $\mathbf{U}$ would in turn imply a continuous change of $\mathbb{H}$, $\mathbb{L}$ and $\mathbb{C}$. This coupling between the problem matrices and the optimisation variables makes the solution impossible to find with LP/QP routines.

5.3.2 Linear Cost

The previous formulation demands observability at each j-th maneuver by maximising the positive linear independence of the natural evolution of $\mathbf{x}_j$ and the perturbed

trajectory. However, section 4.3.1 proved the observability should be enforced with respect to the evolution of the initial condition $\mathbf{x}_1$, irrespective of the numbers of maneuvers in-between. Thus, the objective inside (5.13) could be re-written as:

$$\mathcal{J}_{o_l} = \sum_{k=1}^{n-2} (\mathbf{\Lambda}_k \bar{\mathbf{x}}_k)^T (\mathbf{\Lambda}_k \mathbf{x}_k + \mathbf{\Gamma}_k \mathbf{u}_k) \tag{5.23}$$

After some algebra, expressing everything in terms of the global vector $\mathbf{U}$ yields:

$$\mathcal{J}_{o_l} = \mathbb{L}^T \mathbf{U} + \mathbb{C} \tag{5.24}$$

where the expression of $\mathbb{C}$ is unchanged and $\mathbb{L}$ is slightly modified to:

$$\mathbb{L}_j = \mathbf{x}_1^T \mathbb{A}_{1j}^T \mathbf{\Lambda}_j^T \mathbf{\Gamma}_j + \mathbf{x}_1^T \left[\sum_{k=j+1}^{n-2} \mathbb{A}_{1k}^T \mathbf{\Lambda}_k^T \mathbf{\Lambda}_k \mathbb{A}_{(j+1)k} \mathbf{G}_j \right] \tag{5.25}$$

The immediate advantage is that (5.24) is linear in $\mathbf{U}$, thus whenever it is combined with the 1-norm fuel objective, the optimisation problem can be solved with a LP algorithm, with great benefits in terms of computational time. Also in this case $\mathbb{C}$ must be included in the objective to avoid possible errors in the multi-objective optimisation, leading to:

$$\mathcal{J}_{o_l} = \mathbb{L}_y^T \mathbf{Y} \qquad \mathbb{L}_y = \begin{bmatrix} \mathbb{L}^T & \mathbf{0}_{1xp} & \mathbb{C} \end{bmatrix}^T \tag{5.26}$$

5.4 Multi-Objective Optimisation

When both the fuel and observability objectives are considered, the guidance problem becomes a *multi-objective optimisation* (MOO), that is generally expressed in the form of:

$$\begin{aligned} \min_{\mathbf{y}} \quad & \mathbf{F}(\mathbf{y}) = [\mathcal{J}_{\mathbf{F}}(\mathbf{y}),\ \mathcal{J}_{\mathbf{o}}(\mathbf{y})] && \text{(5.27a)} \\ \text{subject to} \quad & \mathbf{A}_{eq}\mathbf{y} = \mathbf{b}_{eq} \\ & \mathbf{A}_{iq}\mathbf{y} \leq \mathbf{b}_{iq} \\ & \mathbf{l}_b \leq \mathbf{y} \leq \mathbf{u}_b \end{aligned}$$

Unfortunately, it is not possible to a find a single solution $\mathbf{y}^*$ that simultaneously minimises both objectives because they are in conflict with one another. Thus, when dealing with MOO problems, the concept of *Pareto Optimality* is introduced: a solution $\mathbf{y}_1$ is said to be Pareto optimal if there is no other $\mathbf{y}$ that improves at least one objective function without worsening the others. Pareto points are often referred to as non-dominated solutions.

5.4.1 Survey of Alternatives

In literature, many approaches have been proposed to find the set of Pareto points; most of these are based on parameters that can be used to find solutions in specific regions of the Pareto curve (see [51] for comprehensive survey). A brief overview of the most promising candidates to solve the problem under study is here reported.

Weighted Sum

The most common approach to deal with MOO problems is to exploit a single global objective, obtained from a linear combination of all the original objective functions:

$$\mathcal{J}_w = \sum_{i=1}^{2} w_i \mathcal{J}_i(\mathbf{y}) \tag{5.28}$$

To guarantee that a minimum of $\mathcal{J}_w$ is Pareto optimal, it is sufficient to ensure all the weights w_i are positive. In addition, a necessary condition to obtain all the non-dominant solutions with this method requires the Pareto curve to be convex. For the case at hand, this criterion is always satisfied because all the previously proposed objective functions are also convex. The major downside of the weighted-sum is that even if the curve is convex, an even spread of the weights does not ensure an even spread of the points on the Pareto curve [52]. Indeed, in many cases the points are clumped in specific regions of the Pareto set and the designer may struggle at finding the remaining part of the curve.

This issue is enhanced by the great difference between the order of magnitudes of the two objective functions, which makes the selection of proper weights more challenging. For example, a scaling factor that guarantees a certain balance between the two objectives in a given scenario, does not necessarily accomplish so in a different environment. In this regard, some techniques are available to ease the selection of the weights:

- *Fuel optimal*: as proposed by [13], the objectives are scaled by their values computed with the fuel-optimal trajectory. Notice this is not a proper normalisation because the fuel objective will always be greater than one before the weights w_i are applied.
- *Max norm*: the objective $\mathcal{J}_i$ is normalised by its maximum possible value; that is, the value of $\mathcal{J}_i$ when the other objective is minimised.
- *Min-Max norm*: before being introduced inside (5.28), each objective is normalised as follows:

$$\mathcal{J}_i = \frac{\mathcal{J}^i - \mathcal{J}^i_{min}}{\mathcal{J}^i_{max} - \mathcal{J}^i_{min}} \tag{5.29}$$

All these normalisation procedures can be employed inside a LP/QP algorithm by either augmenting the decision vector (similarly to the inclusion of $\mathbb{C}$) or simply scaling the objective functions.

Normal Constraint

The Normal Constraint (NC) is a technique that generates a set of evenly spaced solutions on the Pareto curve. By tuning a specific parameter, the algorithm can find all (and only) the Pareto solutions. A detailed explanation of the method can be found in [53] and only a few key information are here given.

The NC scales both objective functions with the min-max norm and includes an additional constraint in the original MOO problem (5.27a) to guarantee a uniform spread of the Pareto points. However, the new constraint acts on the objective functions. As a consequence, since one of the observability objectives is quadratic,

the guidance problem would become a Quadratic Programming Quadratic Constraint (QPQC) problem. This class is classified as *Nondeterministic Polynomial-time hard problem* (NP-hard) [54] and cannot be solved with the same algorithms of the Quadratic Programming Linear Constraint case.

A workaround is only possible when the objective functions are symmetric and positive semi-definite. Under this assumption, (5.27a) can be recast as a Second-Order Cone Programming (SOCP) optimisation problem. However, for the case at hand, the SOCP formulation is unfeasible because the dimensions of the matrices and their condition numbers make the problem numerically unstable. Therefore, a non-linear optimiser must be used to seek a solution, expressing the additional constraint as a non-linear function.

A similar version of this algorithm exists and is called Normal Boundary Intersection [55]. The logic behind it is quite similar to the aforementioned technique but it was discarded because the NC resulted more reliable.

5.4.2 Trade-Off Criteria

When solving the original MOO problem, the designer is interested in finding a single solution on the Pareto curve, rather than a set of points. The solution will then be translated into a maneuver plan and properly executed. This reason is behind the exclusion of heuristic algorithms (e.g., genetic algorithms or particle swarms) from the list of potential candidates: they simultaneously provide all the Pareto points but highly increase the computational demands. A suitable method would be one that guarantees a solution in low time and that is robust with respect to the problem formulation. For example, when solving the optimisation problem multiple times along the trajectory, the boundary conditions and the remaining duration of the approach continuously change. In this regard, robustness is used to identify a technique that, for a given value of the control parameter, always provides the same level of compromise between the two objective functions. If that is not the case, the guidance may not be able to ensure the same level of observability throughout the whole operation.

Method	Computational Cost	Non-Dominance	Robustness
FO - WS	1 LP + 1 QP	Fuel branch optimal	Good
Max - WS	1 LP + 2 QP	Mediocre	Good
MM - WS	1 LP + 2 QP	Good	Mediocre
NC	1 LP + 1 QP + 1 NLP	Observability branch optimal	Mediocre

TABLE 5.2: Comparison among different MOO techniques.

NLP indicates a non-linear solver is used. Max and MM are the Maximum and Min-Max normalisation, respectively. The table assumes the quadratic observability cost function is used.

A comparison among the possible alternatives is shown in Table 5.2. The two techniques that are more appealing, in terms of Pareto optimality, are the Fuel-Optimal Weighted Sum (FOWS) and the NC. However, neither of them is completely capable of capturing the whole curve and only provide good results in the regions associated with the fuel and observability branch, respectively. This behaviour is probably

connected with the large variations of the objectives magnitudes and a very fine tuning of the control parameter might be needed to extend the results to the opposite branch. Nevertheless, the NC method is much more demanding from a computational standpoint and, when applied to large-scale problems, the non-linear solver struggles at finding a reliable solution. The remaining two weighted sum alternatives did not provide good enough performance to justify the additional QP iteration and were discarded.

A simple but practical consideration is used to discriminate between the remaining two candidates. In first approximation, the shape of a convex Pareto curve can be modelled as an equilateral hyperbola. Thus, when moving towards the observability branch, small improvements in observability result in drastic increments of ΔV. However, as the available fuel on-board is limited by the system design, it is always desirable to work in proximity of the fuel optimal solution. Therefore, the FOWS was deemed the most suitable technique to solve the MOO problem. The global objective is formulated as:

$$\mathcal{J}_w = (1-w)\frac{\mathcal{J}_F}{\mathcal{J}_{FO}^F} + w\frac{\mathcal{J}_o}{\mathcal{J}_{FO}^o} \tag{5.30}$$

Finally, notice that throughout the rendezvous approach, observability should be enhanced only to aid the convergence of the navigation filter. Indeed, once the error has been reduced below the desired accuracy threshold, demanding additional observability would only result in an unneeded increment of the fuel consumption. Similarly to [13], the norm of the position-related diagonal components of the covariance matrix $\mathbf{P}$ is used as a metric of the current estimation uncertainty. Whenever this value is below the accuracy threshold, only the fuel-optimal trajectory is computed.

5.5 Problem Constraints

5.5.1 Boundary Conditions

To specify a desired final point for the trajectory, the final position is written in function of the global maneuver vector $\mathbf{U}$ and of the initial conditions:

$$\mathbf{x}_n = \mathbb{G}\mathbf{U} + \mathbb{A}_{1n}\mathbf{x}_1 \tag{5.31}$$

where $\mathbf{x}_1$ is the initial point, $\mathbb{A}$ is computed with (5.20) and $\mathbb{G}$ is a $6 \times m$ matrix defined as:

$$\mathbb{G} = \begin{bmatrix} \mathbb{G}_1 & \mathbb{G}_2 & \dots & \mathbb{G}_{n-1} \end{bmatrix} \tag{5.32}$$

and the general matrix in the j-th slot equals:

$$\mathbb{G}_j = \mathbb{A}_{(j+1)n}\mathbf{G}_j \tag{5.33}$$

The final position is enforced by adding an equality constraint to the problem and augmenting the matrix $\mathbb{G}$ to account for additional variables in the optimisation vector $\mathbf{Y}$:

$$\mathbf{A}_{BC}\mathbf{Y} = \mathbf{b}_{BC} \tag{5.34}$$

with

$$\begin{aligned} \mathbf{A}_{BC} &= \begin{bmatrix} \mathbb{G} & \mathbf{0}_{6\times(p+q)} \end{bmatrix} \\ \mathbf{b}_{BC} &= \hat{\mathbf{x}}_{EC} - \mathbb{A}_{1n}\mathbf{x}_1 \end{aligned} \tag{5.35}$$

where $\hat{\mathbf{x}}_{EC}$ is the desired final point, p depends on the fuel cost function (as reported in section 5.3.1) and q is equal to zero or one for the fuel-optimal or observability-enhanced trajectories, respectively. Notice that the structure of $\mathbf{A}_{BC}$ makes the adoption of a linearisation with respect to the chaser inconvenient also for the fuel-optimal trajectories, because $\mathbf{U}$ affects the boundary conditions constraint as-well.

5.5.2 Thrust Magnitude

Thrust magnitude constraints are easily added through the lower and upper bound vectors as:

$$\begin{aligned} \mathbf{l}_b &= -u_m \begin{bmatrix} \mathbf{1}_{1\times m} & \mathbf{0}_{1\times p} & -\frac{1}{u_m} \end{bmatrix}^T \\ \mathbf{u}_b &= \quad u_m \begin{bmatrix} \mathbf{1}_{1\times m} & \mathbf{1}_{1\times p} & \frac{1}{u_m} \end{bmatrix}^T \end{aligned} \tag{5.36}$$

The final element is added only when observability is required and it allows to include $\mathbb{C}$ inside $\mathcal{J}_o$. Due to the discrete formulation of the original problem (5.2), u_m is expressed as a velocity and equals the maximum ΔV available for each maneuver. These constraints can also be expressed in matrix form as $\mathbf{A}\mathbf{y} \leq \mathbf{0}$; nevertheless, the results are the same. Finally, notice that (5.36) is applied to each direction independently, since a constraint on the norm of each impulse would not be compliant with a LP/QP routine.

5.5.3 Relative Motion

Another useful class of constraints that can be added to the problem allows to specify forbidden zones: areas that the chaser is prohibited from entering. A simple technique that bounds the state of each point is formulated as:

$$\mathbf{X}_l \leq \mathbf{X} \leq \mathbf{X}_u \tag{5.37}$$

where $\mathbf{X}_l$ and $\mathbf{X}_u$ are vectors of dimension $6(n-2)$. With the same algebraic manipulations, the global position vector $\mathbf{X}$ is expressed as function of the global maneuver vector $\mathbf{U}$ as:

$$\mathbf{X} = \mathbb{E}\mathbf{x}_1 + \mathbb{F}\mathbf{U} \tag{5.38}$$

where

$$\begin{aligned} \mathbb{E} &= \begin{bmatrix} \mathbb{A}_{12}^T & \mathbb{A}_{13}^T & \dots & \mathbb{A}_{1(n-1)}^T \end{bmatrix}^T \\ \mathbb{F} &= \begin{bmatrix} \mathbf{G}_1 & \mathbf{0} & \dots & \mathbf{0} \\ \mathbb{A}_{23}\mathbf{G}_1 & \mathbf{G}_2 & \dots & \mathbf{0} \\ \vdots & \vdots & \ddots & \vdots \\ \mathbb{A}_{2(n-1)}\mathbf{G}_1 & \mathbb{A}_{3(n-1)}\mathbf{G}_2 & \dots & \mathbf{G}_{n-2} \end{bmatrix} \end{aligned} \tag{5.39}$$

The final form of the constraint with respect to the augmented optimisation vector $\mathbf{Y}$ is:

$$\begin{aligned} \mathbf{A}_l\mathbf{Y} &\leq \mathbf{b}_l \\ \mathbf{A}_u\mathbf{Y} &\leq \mathbf{b}_u \end{aligned} \tag{5.40}$$

with

$$\begin{aligned} \mathbf{A}_l &= \begin{bmatrix} -\mathbb{F} & \mathbf{0}_{6(n-2)\times(p+q)} \end{bmatrix} & \mathbf{b}_l &= \mathbb{E}\mathbf{x}_1 - \mathbf{X}_l \\ \mathbf{A}_u &= \begin{bmatrix} \mathbb{F} & \mathbf{0}_{6(n-2)\times(p+q)} \end{bmatrix} & \mathbf{b}_u &= \mathbf{X}_u - \mathbb{E}\mathbf{x}_1 \end{aligned} \tag{5.41}$$

The flexibility of this constraint allows to introduce many variations to the original unconstrained trajectory. For example, it can be used to identify the direction of a potential approach corridor or limit the components of the relative velocities from a given step until the final epoch.

When multiple types of constraints are simultaneously applied to the optimisation problem, all the matrices and vectors are combined together as:

$$\begin{aligned} \mathbf{A}_{iq} &= \begin{bmatrix} \mathbf{A}_l^T & \mathbf{A}_u^T & \mathbf{A}_s^T \end{bmatrix}^T \\ \mathbf{b}_{iq} &= \begin{bmatrix} \mathbf{b}_l^T & \mathbf{b}_u^T & \mathbf{b}_s^T \end{bmatrix}^T \end{aligned} \tag{5.42}$$

5.6 Non-Linear Formulation

In order to include the observability angle as a metric inside the optimisation problem, a non-linear formulation is required. A wide number of option is available, such as using (4.51) as an observability cost function, expanding $\mathcal{J}_\theta$ to each single discretisation step.

Nevertheless, the easiest and most effective approach is to augment (5.1) with an additional non-linear constraint, demanding that after M steps the observability angle should be greater or equal than a given threshold. The number of steps can be used as an additional tuning parameter. For example, it can be selected to ensure the error is reduced by the time the next re-optimisation occurs. Mathematically, the constraint is expressed as:

$$c(\mathbf{U}) = \theta_{THR} - \frac{\bar{\mathbf{x}}_M^T \mathbf{x}_M(\mathbf{U})}{\|\bar{\mathbf{x}}_M\| \|\mathbf{x}_M(\mathbf{U})\|} \leq 0 \tag{5.43}$$

where $\bar{\mathbf{x}}_M$ depends only on the initial conditions. By formulating this constraint as an inequality, the solver will automatically find the solution with the lowest fuel consumption among all the possible values of $\theta \geq \theta_{THR}$. The two vectors in the previous expression are easily computed as:

$$\begin{aligned} \bar{\mathbf{x}}_M &= \mathbb{A}_{1M}\mathbf{x}_1 \\ \mathbf{x}_M &= \bar{\mathbf{x}}_M + \mathbb{G}_M\mathbf{U} \end{aligned} \tag{5.44}$$

The matrix $\mathbb{G}_M$ is similar to (5.32) but is evaluated only up to the $(M-1)$-th term:

$$\begin{aligned} \mathbb{G}_M &= \begin{bmatrix} \mathbb{G}_1 & \dots & \mathbb{G}_{M-1} & \mathbf{0} & \dots & \mathbf{0} \end{bmatrix} \\ \mathbb{G}_j &= \mathbb{A}_{(j+1)M}\mathbf{G}_j \end{aligned} \tag{5.45}$$

The evaluation of the non-linear constraint can be accelerated by pre-computing these matrices. In addition, since the observability metric is added as a constraint, the guidance problem becomes a single-objective optimisation and only one iteration of the algorithm is required.

Therefore, the complete non-linear optimisation problem can be summarised as:

$$
\begin{aligned}
\min_{\mathbf{y}} \quad & \mathcal{J}_F(\mathbf{y}) && \text{(5.46a)}\\
\text{subject to} \quad & \mathbf{A}_{eq}\mathbf{y} = \mathbf{b}_{eq} \\
& \mathbf{A}_{iq}\mathbf{y} \leq \mathbf{b}_{iq} \\
& \mathbf{l}_b \leq \mathbf{y} \leq \mathbf{u}_b \\
& c(\mathbf{y}) \leq 0
\end{aligned}
$$

A common approach to solve this problem is to exploit a Sequential Quadratic Programming (SQP) algorithm, which solves the (5.46) as a sequence of optimization sub-problems. Moreover, the computational time can be further reduced by specifying the analytical expression for the gradient of the objective function $\nabla\mathcal{J}$ with respect to the optimisation variables:

$$
\begin{aligned}
\nabla\mathcal{J}_F &= \begin{bmatrix}\mathbf{0}_{1\times m} & \mathbf{1}_{1\times m}\end{bmatrix} && \text{for} \quad \mathcal{J} = \mathcal{J}_{F_s} \\
\nabla\mathcal{J}_F &= \mathbf{U}^T\mathcal{Q} && \text{for} \quad \mathcal{J} = \mathcal{J}_{F_q}
\end{aligned}
\tag{5.47}
$$

Notice that, even though with non-linear solvers the 1-norm of $\mathbf{U}$ can be computed without the need of introducing slack variables, the SQP algorithm finds a solution in less time when $\mathcal{J}_F$ is a continuous and smooth function; that would not be the case if the sum of the modulus of $\mathbf{U}$ was directly computed.

Chapter 6

Simulation Results

This chapter reports the outcomes of the numerical testing campaign performed to assess the applicability and robustness of the proposed SH - MPC approach. Initially, a series of off-line tests is conducted to validate the resulting fuel-optimal solutions and investigate their sensitivity on the number of discretisation points and total rendezvous time. Thereafter, the ability of the different observability metrics to aid the converge of the navigation filter are tested in a closed-loop system on three distinct approach scenarios. The sensitivity of the navigation solution on the target position and on different degrees-of-approximation of the real dynamics is assessed. Finally, a new operational scenario is presented, highlighting that angles-only measurements can also be exploited to perform relative navigation between spacecrafts flying on distant heterogeneous non-keplerian orbits.

Throughout the analysis, the target is always assumed to be moving on a periodic non-keplerian orbit. A southern NRHO around the Earth-Moon L2 point has been selected as a primary reference orbit to mimic a potential rendezvous scenario with the LOP-G, where bearing-only navigation could be used either as a main navigation technique for small satellites or as a back-up solution for larger spacecraft. In addition, by positioning the target on a three-dimensional orbit, both the in-plane and out-of-plane relative motion can be excited, regardless of the chaser initial conditions. Since previous researches have identified the NRHO apolune region as the most favourable area to perform the complex rendezvous and docking operations [22] [23] [24], most of the simulations position the chaser in the same neighborhood. In this regard, it is here assumed that the chaser switches from an absolute to a relative navigation at a distance between 100 and 500 km from the target.

In typical LEO rendezvous and formation-flying applications, the relative dynamics is expressed in the Local Vertical Local Horizon (LVLH) frame. Equivalent representations have been proposed for the non-keplerian dynamics [24] [56], but the transformation between the inertial or synodic frame to the LVLH must be performed at each time-step and requires knowledge of the target absolute dynamics. To ease the computations and assembly of the optimisation problem matrices, in this work the relative dynamics is always expressed and represented in the inertial frame. Nevertheless, this assumption does not limit the applicability of the proposed SH - MPC guidance. Indeed, once the target dynamics is known, any boundary condition and/or constraint over the relative LVLH state is easily converted to its synodic counterpart through a proper transformation matrix.

To validate the results and comply with the typical accuracy required for GNC functions, a high-fidelity non-keplerian simulator is exploited to propagate the relative dynamics in the Earth-Moon domain; it is based on the EpR4BP and includes the SRP effects on both chaser and target, accordingly to their physical properties. As

a last remark, to simplify the computation of the input-matrix $\mathbf{G}$, the chaser is only allowed to perform impulsive maneuvers.

6.1 Offline Guidance Validation

Before testing the performance of the complete architecture, it is important to asses whether or not the guidance is capable of synthesising a suitable maneuver profile. To decouple the results from the observability issues of a bearing-only solution, the navigation filter is temporarily excluded from the simulations and the guidance uses the exact relative position to compute the necessary control actions. These tests will establish the ability of the SH - MPC guidance to yield competitive fuel-optimal solutions (in terms of ΔV) with respect to other approaches for the generation of rendezvous trajectories. In addition, as these results hold irrespective of the navigation technique, they will serve as a potential baseline to compare the performance of future MPC formulations for the non-keplerian dynamics.

6.1.1 Trajectory Discretisation

The time required to solve the optimisation problem strictly depends on the number of variables and in turn, on the discretisation step. The major advantage coming from the LP/QP formulation of the optimisation problem is the low computational effort required to find a solution. However, even though there are many algorithms capable of solving the problem, not all have the same degree of efficiency. For example, considering the linear case, it is well known that the simplex method struggles to deal with large-scale problems as the solving time might become exponential in the number of unknowns and on the amount of data to be stored. Historically, this was the reason that pushed for the development of a much more efficient class of algorithms, called *interior-point* methods, which ensure the number of iterations is polynomially bounded by the dimensions of the problem. Therefore, in this work interior-point algorithms have been adopted to solve both the linear and quadratic versions of the optimisation problem.

With this in mind, the computational time can be further reduced by adopting larger discretisation steps, i.e., increasing the time between each maneuver. Indeed, although an exact solution for the discrete matrices in (5.2) is not available, the analysis in section 2.5.2 highlighted that the approximation errors are below 1 km as long as the propagation time does not exceed 24 hours In addition, if one considers a total rendezvous duration of 10 hours, it immediately stands clear that any reasonable discretisation of this interval will have a minimal impact on the accuracy of the solution. A comparison in terms of solving time between the LP and QP formulations is shown in Figure 6.1a and, even though the LP case has double the amount of unknowns (because of the slack variables), the linear algorithm is almost always faster than the quadratic alternative. Nevertheless, both routines yield a solution in a fraction of a second, regardless of the number of points; making the approach very appealing for multiple on-board optimisations.

However, a limitation on the maximum number of points comes from the time required to assemble the matrices for the observability cost functions. In particular, Figure 6.1b suggests that the time to build the matrix $\mathbb{H}$ (the red line) is much greater than the time required to solve the problem and it even exceeds the minute when a fine time-discretisation is employed. In addition, please notice that despite the high

values, these results have been obtained with an optimised assembly procedure, as the straightforward evaluation of these matrices from their definition in (5.19) would require 10 times more computational resources.

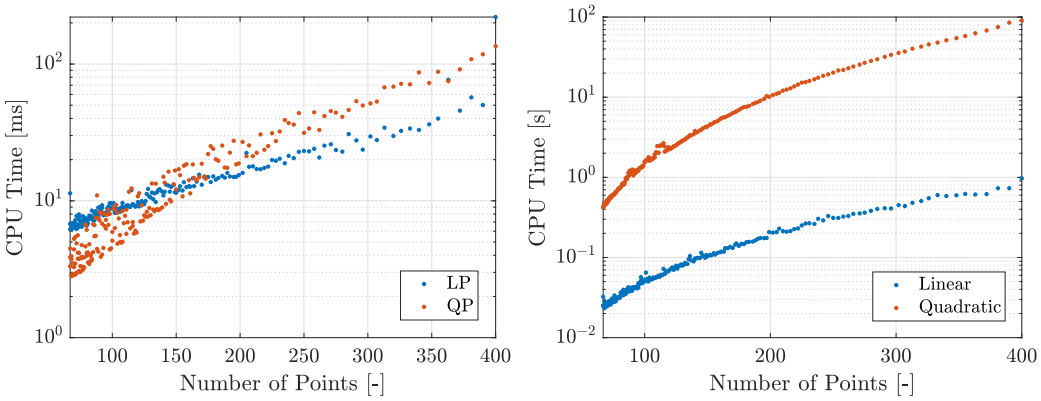

(*a*) Solving Time. (*b*) Assembly Time.

FIGURE 6.1: The left plot shows the comparison in terms of solving times between the two fuel cost functions. The right plot reports the times required to assemble the matrices of the observability metrics. The results are valid for an Intel i7-6700 and a RAM of 16 GB.

On the other hand, the assembly of the vector $\mathbb{L}$ for the linear cost function (the blue line) is much faster than the quadratic version, even though the CPU time is still higher than that required by either of the solving algorithms. Thus, whenever the guidance must account for the quadratic observability objective, it is desirable to work with a low number of discretisation points, otherwise the advantages coming from the the LP/QP formulations are denied by the lengthy times required to build the observability matrices. Another key actor to consider when selecting the time-step is the sensitivity of the solution (in terms ΔV) to the number of discretisation points. In this regard, Figure 6.2 presents the results for the two fuel cost functions.

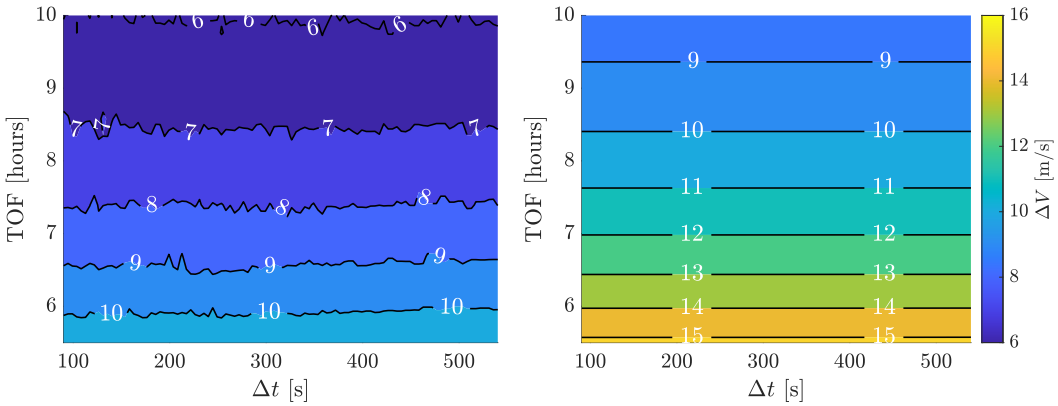

(*a*) Slack Variables. (*b*) Quadratic Control.

FIGURE 6.2: Sensitivity of the fuel-optimal solution to the discretisation step and time-of-flight for the linear and quadratic formulations.

The color-bar is shared among the two plots. The chaser is on an unstable manifold of the NRHO apolune at a distance of 100 km.

It is evident that the fuel consumption holds irrespective of the discretisation step, with an imperceptible improvement at the lowest Δt. Instead, the costs of fuel-optimal trajectories are driven only by the duration of the approach, which is here treated as a fixed design variable. For a visual comparison with Figure 6.1, the number of discretisation points were evaluated with a Time-of-Flight (TOF) of 10 hours. With these results in mind, it is reasonable to assume that a large discretisation step (e.g., about 30 points) can be adopted without the need of worrying for approximation errors nor increments of ΔV.

6.1.2 Fuel-Optimal Solutions

An interesting comparison between the two fuel cost functions is immediately available from Figure 6.2. For the same values of TOF and discretisation step, the quadratic control solution is always more expensive than that coming from the linear objective. The difference is around 2 m/s for the highest rendezvous duration and increases to approximately 5 m/s when the TOF drops to 6 hours. This behaviour is due to the physical meanings of the two fuel objectives: the linear cost function is a more realistic expression for the total ΔV expenditure, as highlighted in section 5.2. Indeed, it can be proved that the trajectory with the minimum ΔV does not appear optimal from a quadratic standpoint. Nevertheless, the trend in the plot suggests that the difference between the two can be attenuated by increasing the rendezvous duration. On the other hand, the quadratic solution appears much more stable to the variations of the discretisation step, whereas the slack variables display some irregularities.

To verify the optimality of the proposed approach, the trajectories provided by the MPC are compared with a Direct Transcription (DT) of the rendezvous problem. This method reduces the optimal control problem into a Non-Linear Programming (NLP) formulation through a polynomial parametrisation of the control action (see [23][24] for further details). The objective function is defined in terms of a minimum energy control (i.e., quadratic control) over the the interval $[0, T_{rdv}]$. To guarantee an optimal result, the NLP algorithm integrates the exact EpR4BP perturbed dynamics; thus, the maneuver plan is computed a-priori and does not require any re-optimisations. Instead, the SH-MPC guidance is based on a CR3BP approximation and is updated once every hour, with a discretisation step of 10 minutes.

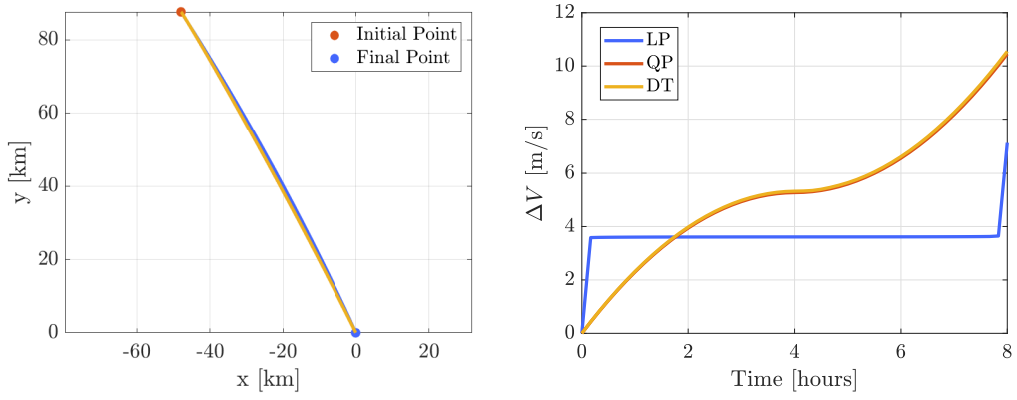

(*a*) Relative motion in the x-y plane.

(*b*) Cumulative ΔV.

FIGURE 6.3: Comparison between the SH - MPC and the direct transcription solutions. The yellow line is superimposed to the red one.

In Figure 6.3 it is straightforward to notice that the DT solution is identical to the quadratic fuel formulation of the guidance. Although the result may seem obvious, the control action employed inside the DT algorithm is continuous, whereas the LP/QP is based on impulsive maneuvers. As highlighted in section 2.5.2, the convolution integral for a generic continuous thrust $\mathbf{u}(t)$ cannot be reduced to a product between an input matrix $\mathbf{G}$ and a vector $\mathbf{u}$, making that kind of maneuvers impossible to model in this framework. Bearing this in mind, the important conclusion coming from Figure 6.3 is that by solving for the quadratic fuel objective $\mathcal{J}_{F_q}$, impulsive maneuvers can also be used to approximate a low-thrust continuous control.

Table 6.1 summarises the performance of the two SH-MPC fuel objectives, together with the maximum and minimum timings required to a find a solution. By re-optimising the maneuver plan, both formulations grant a very high accuracy in the final position, with the errors increasing to about 15 meters when the optimisation is performed only at the beginning of the approach. Notice that with a low number of discretisation points, the LP requires a slightly higher time to find a solution than the QP problem, accordingly to Figure 6.1a.

Method	$\mathbf{T}_{min}$ [ms]	$\mathbf{T}_{max}$ [ms]	ΔV [m/s]	$+\Delta V$ [m/s]	**Accuracy** [m]
LP	3.46	16.73	7.284	0.093	1.42
QP	1.96	8.25	10.561	0.004	1.83

TABLE 6.1: SH-MPC fuel-optimal solutions performance.

$+\Delta V$ is the difference between the fuel expended and that required at the time of the first optimisation. An exact knowledge of the target state at each optimisation time was assumed.

The cumulative ΔV evolution in Figure 6.3b shows that the 1-norm objective (i.e., the slack variables formulation) is characterised by a bang-bang type of control at the initial and final points, exploiting the natural dynamics in-between the impulses. On the other hand, the quadratic control action progressively evolves from a large acceleration at the beginning to a final breaking phase, with the highest relative velocity (about 5 m/s) reached half-way through the approach. This slowly-approaching behaviour makes the QP control more robust to possible thrusters malfunctions with respect to the 1-norm objective. Indeed, if the final maneuver was not executed, the greater relative velocity of the LP case would make the chaser drift-away, largely increasing the ΔV required for a future trajectory re-adjustment.

Figure 6.3a shows the typical form of a non-Keplerian rendezvous trajectory: the chaser moves on an almost straight line towards the desired final point. The rounded shapes of the Keplerian relative dynamics are missing because the rendezvous time is much smaller than the orbital period of a cislunar orbit.

As a last remark, these results confirm the capability of the proposed SH - MPC guidance to yield fuel-optimal trajectories. The approximation due to the CR3BP linearised relative model only causes a final position error of 1 meter, which is negligible when compared to the navigation errors that will be introduced by the bearing-only measurements.

6.2 On-board Guidance for Rendezvous Operations

To investigate the ability of the proposed architecture to perform a quasi autonomous bearing-only rendezvous with the LOP-G, the Shrinking Horizon - MPC guidance is tested in a closed-loop system along with a navigation filter. Two Holding Points (HP) are used to identify the desired initial and final relative states. In a practical rendezvous approach, these points are used as checkpoints: they allow to account for operational constraints by enforcing few desired relative positions throughout the approach. Three different rendezvous scenarios are used to compare the various observability metrics presented in Chapter 5, varying the initial holding point around the NRHO apolune. The results of each simulation are analysed from an operational standpoint to establish which formulation of the observability objective provides the highest degree of observability while satisfying plausible mission and navigation requirements.

6.2.1 Architecture Overview

A scheme of the simulation architecture is presented in Figure 6.4. In this framework, the guidance uses the navigation estimate for the optimisation and updates the control plan accordingly to the logic shown in figure 5.2. A high-fidelity propagator is used to simulate the chaser and target absolute dynamics, accounting for the perturbing effects of the sun gravitational force and the SRP. In this regard, the target is assumed to be a 400-tons spacecraft with an exposure area of 12.000 m^2, mimicking an ISS-class object. On the other hand, the chaser represents a hypothetical automated transfer vehicle, with a mass of 20 tons and total surface of 125 m^2. A summary of the remaining simulation parameters is reported in Table 6.2.

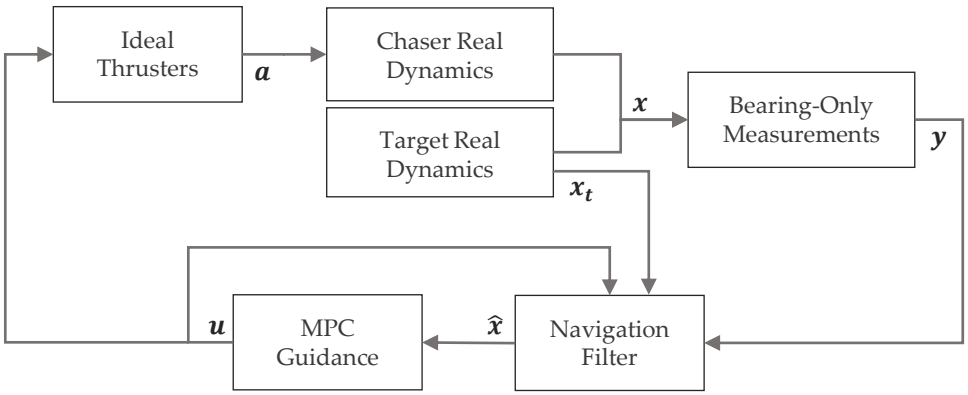

FIGURE 6.4: Simulation architecture scheme.

Notice that the propagation of the relative dynamics inside the navigation filter requires knowledge of the target absolute state. For this reason, it is here supposed that at each re-optimisation epoch, an uncertain estimate of the absolute state of the target is transmitted to the chaser. Then, the information is propagated on-board until the next optimisation. In practice, the communication link could transmit the absolute states of either spacecraft, as the other is immediately available from the relative state. Unfortunately, this need for the absolute navigation makes impossible to completely automatise this guidance scheme.

The control problem is not considered in this work, thus thrusters are modelled as

ideal actuators, neglecting transient states and any kind of pointing errors. An EKF is chosen as navigation filter and is aided by the DMC to tune the state process covariance and approximate unmodelled accelerations. The STM for the guidance and navigation functions is computed with a 2^{nd}- order approximation based on the CR3BP model. In addition, the target position with respect to the primaries is expressed in the inertial frame because it allows for a more reliable estimation than that of a rotating perspective, where the presence of cross-coupling perturbing terms is harder to model. Concerning the desired accuracy threshold, a conservative value of 0.5% of the range has been chosen instead of the classical 1-percent.

Parameter	**Value**	**Confidence Interval**
Time Settings		
Re-optimisation time step	1 hour	-
Discretisation time step	600 s	-
Filter update frequency	1 Hz	-
Filter Settings at 100 km		
Position uncertainty	$\begin{bmatrix}6 & 9 & 6\end{bmatrix}$ km	1σ
Velocity uncertainty	$\begin{bmatrix}0.3 & 0.3 & 0.3\end{bmatrix}$ m/s	1σ
Filter Settings at 250 km		
Position uncertainty	$\begin{bmatrix}15 & 15 & 15\end{bmatrix}$ km	1σ
Velocity uncertainty	$\begin{bmatrix}1 & 1 & 1\end{bmatrix}$ m/s	1σ
Noise Settings		
Target position noise	$\begin{bmatrix}300 & 300 & 300\end{bmatrix}$ m	1σ
Target velocity noise	$\begin{bmatrix}0.1 & 0.1 & 0.1\end{bmatrix}$ m/s	1σ
Measurement noise	1 mrad/axis	1σ

TABLE 6.2: Simulation settings.

The weights for the multi-objective optimisation were selected on the results of a dedicated tuning campaign and represent a trade-off between fuel-consumption and error reduction. As a last remark, to statistically characterise the navigation performance, 300 Monte Carlo simulations are run for each scenario, varying the filter initialisation and the noise effects.

6.2.2 Case A: Center Manifold

In this scenario, the initial holding point (HP_1) is placed on the NRHO center manifold at a relative distance of 250 km. The natural dynamics of this location is characterised by a periodic hovering motion around the target. Therefore, it can be exploited to ensure the chaser does not drift away from the target if the control functions were to malfunction at the beginning of the rendezvous. On the other hand, to guarantee a strong passive safety, the second holding point (HP_2) is set on the unstable manifold at the boundary of a 1 km Keep-Out-Sphere (KOS). In a real operation, this location ensures a safe drift away from the target in case of failures [23]. The total rendezvous duration is set to 12 hours.

The results of the simulation are visually represented in Figure 6.5 and summarised in Table 6.3. From the top-left figure, it immediately stands out that the non-linear formulation provides a sudden reduction of the relative error. By directly acting on the observability angle, the maneuver performed near the 1-hour mark greatly enhances the observability of the system, causing an improvement of about 3000 m in the navigation estimate, while remaining at a relatively higher distance from the target with respect to the other techniques. In this regard, the time-evolution of the range confirms the typical behaviour of an observability metric that includes information on the range: both LP and QP techniques favor a fast reduction of the relative distance at the cost of expensive initial impulses. However, this type of trajectories does not appear convenient from an operational viewpoint as the accuracy threshold is violated for most of the approach.

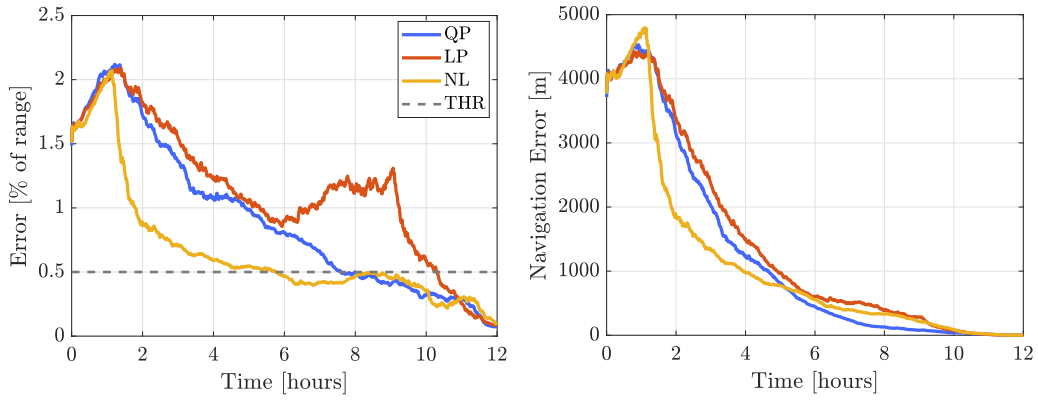

(*a*) Relative navigation error.

(*b*) Absolute navigation error.

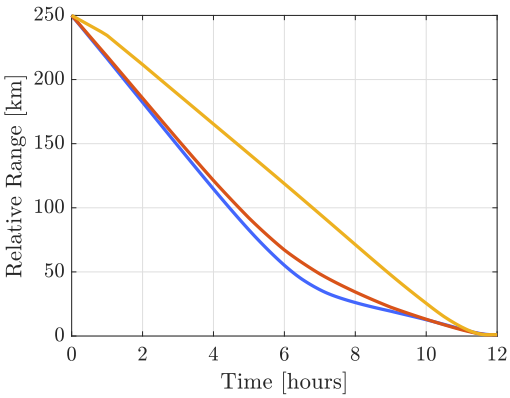

(*c*) Relative distance.

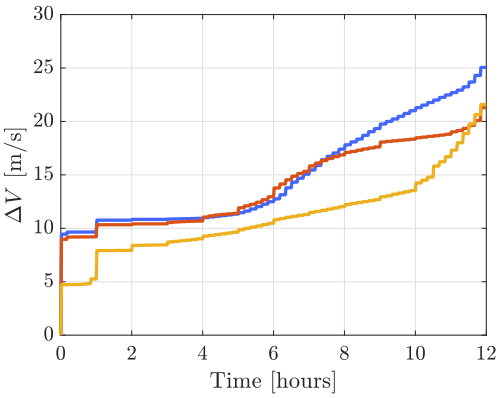

(*d*) Fuel consumption.

FIGURE 6.5: Performance of the bearing-only guidance with the initial point on a center manifold

QP is the quadratic observability objective $\mathcal{J}_{o_q}$, LP the linear observability objective $\mathcal{J}_{o_l}$ and NL is the non-linear formulation.

In particular, Table 6.3 shows that for the formulations based on $\mathcal{J}_o$, the distance at which the filter reaches the desired accuracy is extremely close to the target. Thus, it is very likely that these kind of trajectories would not comply with plausible safety and navigation requirements for a rendezvous with the LOP-G. On the other hand, the non-linear approach outclasses both as it guarantees that from approximately 125 km, the error never exceeds the 0.5% of the relative distance. Nevertheless, all three final navigation errors are smaller than 1 m because the second holding point

was chosen in close-proximity of the station. Indeed, at such a small distance even a low observability angle can provide great reductions of the filter uncertainty, according to (4.49). At the same time, the final position dispersions are slightly higher because at the time of the last re-optimisation (i.e., after 11 hours), the guidance was affected by an inherent position error of approximately 20 m.

Method	$\downarrow \Delta V$ [m/s]	$\downarrow \Delta V_R$ [-]	$\downarrow \mathrm{E}_m$ [km]	$\uparrow \mathrm{R}_{con}$ [km]	$\downarrow$NA [m]	$\downarrow$PA [m]
LP	**21.29**	**1.79**	1.37	10.73	**0.73**	21.02
QP	25.06	2.12	1.22	29.16	0.84	**17.76**
NL	21.58	1.82	**1.04**	**124.42**	0.91	23.20

TABLE 6.3: Center manifold navigation performance.

ΔV_R is the ratio between the ΔV of the observability-ehnanced and fuel-optimal trajectories. E_m is the average value of the Root Mean Square Error (RMSE) of the estimated position and R_{con} is the relative distance at which the filter reaches the desired accuracy. NA and PA are the final navigation and position mean errors (1σ), respectively. The arrow indicates whether the parameter should be minimised ($\downarrow$) or maximised ($\uparrow$).

The ΔV profiles in Figure 6.5d display a peculiar behaviour. Indeed, even though the fuel-consumption was included using the 1-norm objective (i.e., with the slack variables), the resulting acceleration profile is characteristic of low-thrust engines, with small and almost continuous maneuvers. The only exceptions occur at the beginning, when the guidance must account for the observability metric. This result suggests that if a real model of the actuators was included in the simulator, the ΔV of a high-thrust engine would likely be higher than the ones here reported. However, another possible explanation is that each individual run in the Monte Carlo simulation performs a single impulse at a different time from the others. Thus, when taking the mean, the average result is a slowly but constant increment. Overall, despite the LP method requires the lowest ΔV, the non-linear guidance provides much better navigation estimates at the only cost of an extra 0.29 m/s.

6.2.3 Case B: Unstable Manifold

In this scenario, the first holding point is settled on an unstable manifold and the duration of the rendezvous is reduced to 8 hours. Instead, the arrival point remains unchanged.

Interestingly, for the first 2 hours the evolution of the absolute navigation error is almost the same for the three trajectories. Nevertheless, the non-linear approach has a slightly lower relative error because it remains farther from the target. In spite of the previous results, Table 6.4 shows that the linear technique is capable of reaching the accuracy threshold at a similar distance of the NL and also has the lowest average Root Mean Square Error (RMSE). However, in the last two hours it struggles at reducing the absolute range uncertainty and thus, it violates once again the relative threshold. On the other hand, the quadratic metric has the worst performance: it has the highest ΔV because it moves even closer to the target (with respect to the linear metric) but does not manage to simultaneously reduce as much the navigation error, leading to a peak percentage-error above the 1%.

This scenario confirms once again that in the non-keplerian domain, the observability metrics based on $\mathcal{J}_o$ always favour a reduction of the relative range rather than an increment of the angle. Therefore, if an operational requirement for a bearing-only approach was to require the minimisation of the deviations from the original fuel-optimal trajectory, the guidance should be based upon the concept of observability angle.

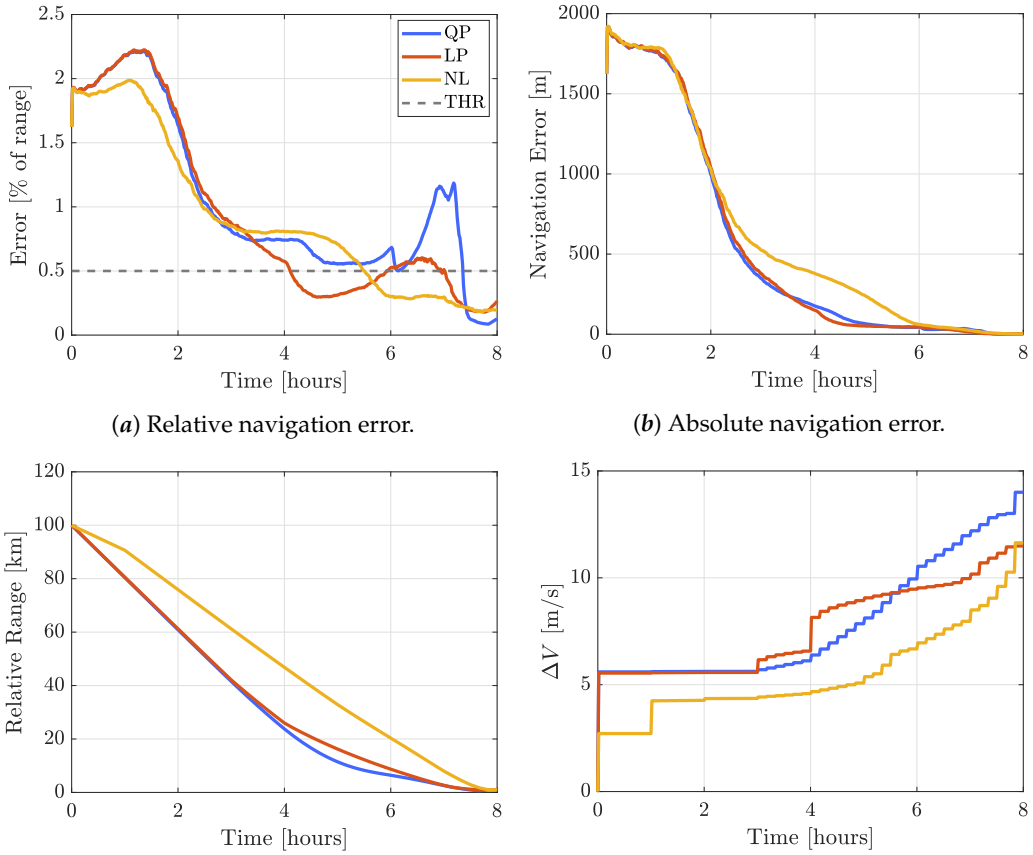

(*a*) Relative navigation error.

(*b*) Absolute navigation error.

(*c*) Relative distance.

(*d*) Fuel consumption.

FIGURE 6.6: Performance of the bearing-only guidance with the initial point on an unstable manifold

Nevertheless, it is important to remark that all three strategies succeed in bringing the chaser to the desired hovering point with minimal position dispersions and navigation errors, similarly to the previous scenario.

Method	↓ ΔV [m/s]	↓ ΔV_R [-]	↓ E_m [km]	↑ R_{con} [km]	↓ NA [m]	↓ PA [m]
LP	14.01	1.79	**0.53**	24.12	2.62	**20.37**
QP	**11.49**	**1.60**	0.54	1.22	**1.31**	41.36
NL	11.60	1.62	0.62	**26.29**	1.96	25.65

TABLE 6.4: Unstable manifold navigation performance.

ΔV_R is the ratio between the ΔV of the observability-ehnanced and fuel-optimal trajectories. E_m is the average value of the Root Mean Square Error (RMSE) of the estimated position and R_{con} is the relative distance at which the filter reaches the desired accuracy. NA and PA are the final navigation and position mean errors (1σ), respectively. The arrow indicates whether the parameter should be minimised (↓) or maximised (↑).

6.2.4 Case C: Periodic Mode

In this last test, the natural dynamics of the initial point is associated to a periodic mode of the NRHO. In particular, since the two spacecraft are on the same absolute orbit, the unperturbed motion of HP_1 simulates an along-track formation, with the chaser shifted backwards of an arbitrary phase angle. Instead, the final point is placed on the very same unstable manifold of the previous scenarios.

Figure 6.7 presents remarkable differences with respect to the performance of the previous tests. Indeed, the initial maneuvers computed with the LP and QP objectives are completely uncapable of providing an improvement in the navigation estimate for almost half of the rendezvous duration. A significant drop of the error only happens when the chaser is extremely close to the target, few hundreds of meters away from the boundary of the KOS. As a result, the relative error at 30 km is almost ten times greater than the allowed maximum. Additional insights on the reasons behind the inability to reduce the error are provided by Figure 6.8. The original periodic trajectory (the violet line) is characterised by an initial motion perpendicular to the x-y plane; at the same time, both LP and QP formulations draw an almost straight line along the y-axis and thus, have minimal differences in terms of azimuth measurements with respect to the nominal trajectory. As a consequence, the filter is unable to reduce the uncertainty along the y-axis. The navigation estimate begins to improve only after 3 hours, when the natural motion bends towards the right-side, effectively differentiating the azimuths.

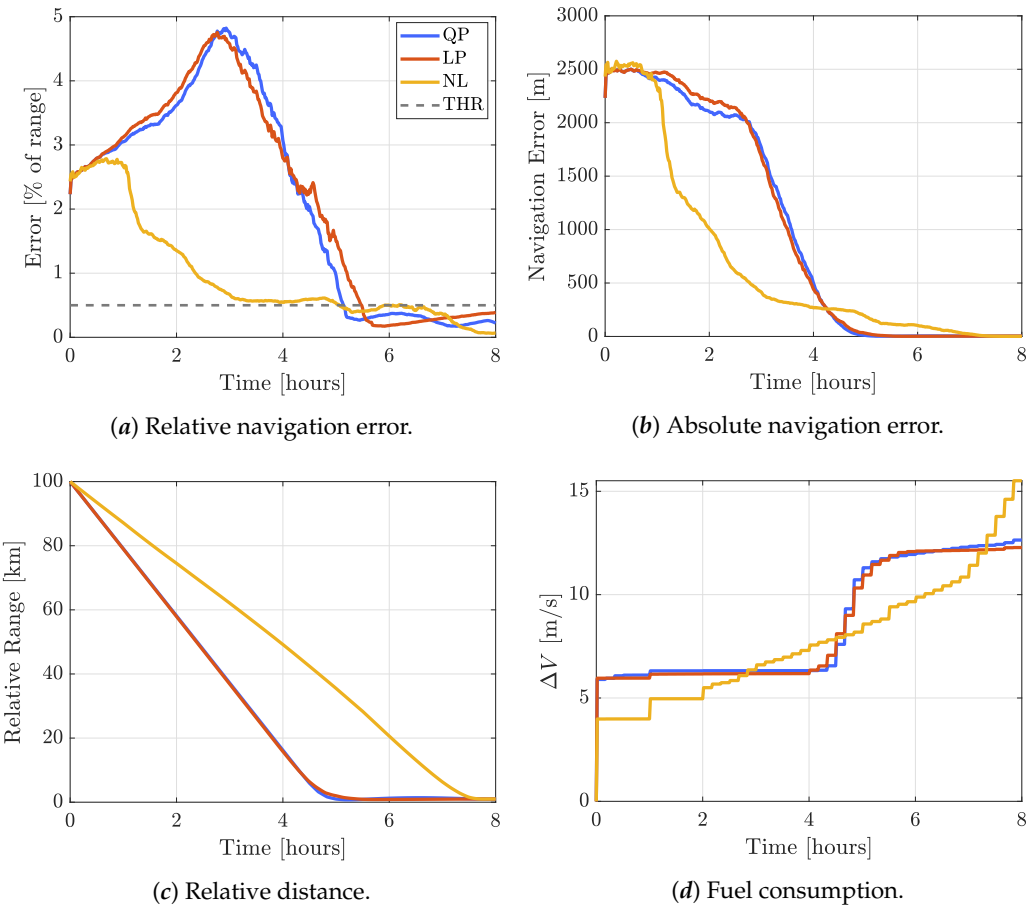

(*a*) Relative navigation error.

(*b*) Absolute navigation error.

(*c*) Relative distance.

(*d*) Fuel consumption.

FIGURE 6.7: Performance of the bearing-only guidance with the initial point on a quasi-periodic mode

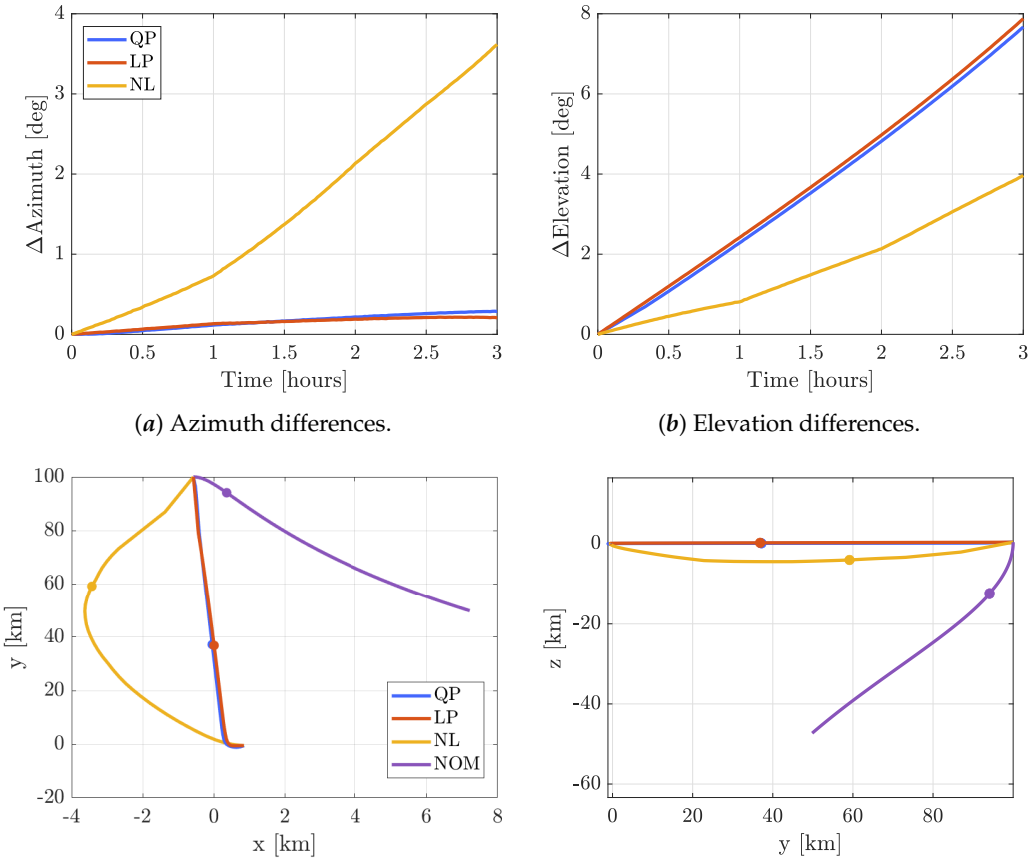

(*a*) Azimuth differences.

(*b*) Elevation differences.

(*c*) Trajectory projection in the x-y plane.

(*d*) Trajectory projection in the y-z plane.

FIGURE 6.8: Approaching trajectories characteristics

In the bottom plots, NOM stands for the nominal trajectory and the tiny dots represent the relative position of the chaser after 3 hours. The red and blue trajectories are superimposed.

On the other side, the NL guidance performs a maneuver at the 1 hour-mark that forces the chaser to move on the opposite side of the y-axis, causing a sudden reduction of more than 1000 m of the navigation error. However, it is interesting to notice that different readings in the elevation angle do not affect the quality of the estimation. In this regard, although the observability angles of the LP and QP trajectories are higher than that of the yellow line, they perform worse because the navigation filter requires differences in the in-plane motion (i.e., the azimuth angle) to reduce the uncertainty along the y-axis. Therefore, these results suggest that there exist some peculiar combinations of nominal and perturbed trajectories, such that a high observability angle does not necessarily guarantee a high degree of observability.

Concerning the final errors, in spite of having the best performance throughout the rendezvous, the non-linear approach has the worst position dispersion. This is again associated with the absolute navigation error at the time of the last re-optimisation. Since the LP/QP trajectories remain in close-proximity of the target for half of the rendezvous duration, they have plenty of time to reduce their absolute errors. Thus, when the final planning is performed, the navigation uncertainty is minimal. With this in mind, these three test scenario highlight that an observability metric based on $\mathcal{J}_o$ is always able to bring the chaser to the desired rendezvous point, with dispersions of only few metres. However, if standard safety and operational requirements (e.g., a threshold on the maximum percentage navigation error) are imposed, the

resulting trajectories will most likely be deemed unfeasible. On the other hand, the addition of a non-linear constraint to enforce the desired observability angle has proven successful in all three cases. Indeed, it consistently allowed the filter to reach convergence at reasonable distances from the target and at the same time, it had very good accomplishments in the remaining performance metrics. As a last remark, the final dispersion can be reduced by introducing additional trajectory re-optimisations towards the ending phase of the rendezvous.

Method	$\downarrow \Delta V$ [m/s]	$\downarrow \Delta V_R$ [-]	$\downarrow \mathrm{E}_m$ [km]	$\uparrow \mathrm{R}_{con}$ [km]	$\downarrow$NA [m]	$\downarrow$PA [m]
LP	**12.27**	**1.71**	1.00	1.12	3.86	**6.39**
QP	12.64	1.77	1.01	1.03	2.21	6.81
NL	15.51	2.16	**0.67**	**34.67**	**0.67**	25.78

TABLE 6.5: Periodic mode navigation performance.

ΔV_R is the ratio between the ΔV of the observability-ehnanced and fuel-optimal trajectories. E_m is the average value of the Root Mean Square Error (RMSE) of the estimated position and R_{con} is the relative distance at which the filter reaches the desired accuracy. NA and PA are the final navigation and position mean errors (1σ), respectively. The arrow indicates whether the parameter should be minimised ($\downarrow$) or maximised ($\uparrow$).

6.2.5 Observability Weights

The previous results were obtained with a fixed observability weight w for the multi-objective optimisation. To display what happens to the quadratic observability metric (QP) $\mathcal{J}_{o_q}$ for different choices of w, the navigation performance for 50 different weights have been collected in Figure 6.9 and 6.10. Notice that each point represents the average performance of 200 Monte Carlo simulations of a rendezvous with similar settings to Case A. In addition, since increasing the observability weight favours a higher fuel consumption (see Figure 6.10a), the ΔV was used in place of w to aid the readability of the plots.

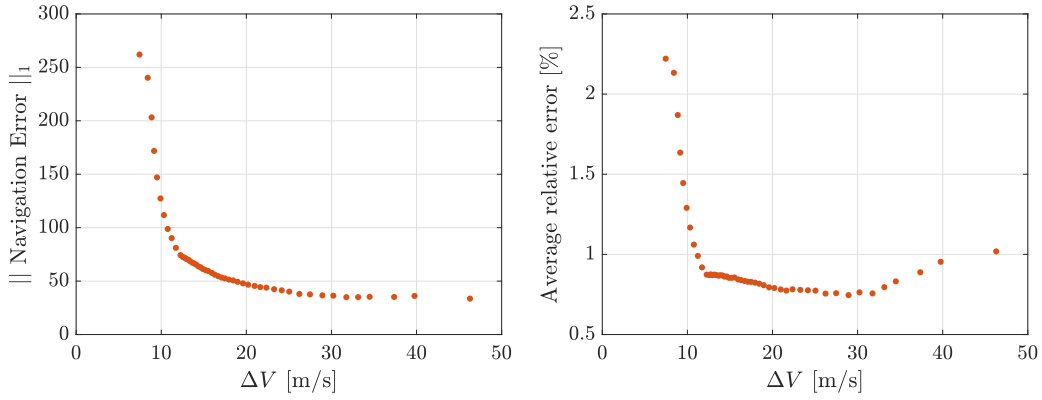

(*a*) Absolute navigation error.

(*b*) Average relative error.

FIGURE 6.9: Navigation errors for increasing observability weights (i.e., for greater ΔVs) for the quadratic observability objective.

Figure 6.9 shows a clear trade-off between the absolute navigation errors and the trajectory cost. In both plots, the points distributions resemble a standard convex

Pareto curve, where small increments of ΔV lead to remarkable improvements of the navigation errors. The exact Pareto Front for the two objectives is visible in 6.10a and confirms that the weighted-sum approach is successful in finding the Pareto optimal solutions. However, despite increasing the observability objective effectively reduces the absolute navigation error, Figure 6.10b shows that the convergence distance does not have a clear nor monotonic trend with the ΔV.

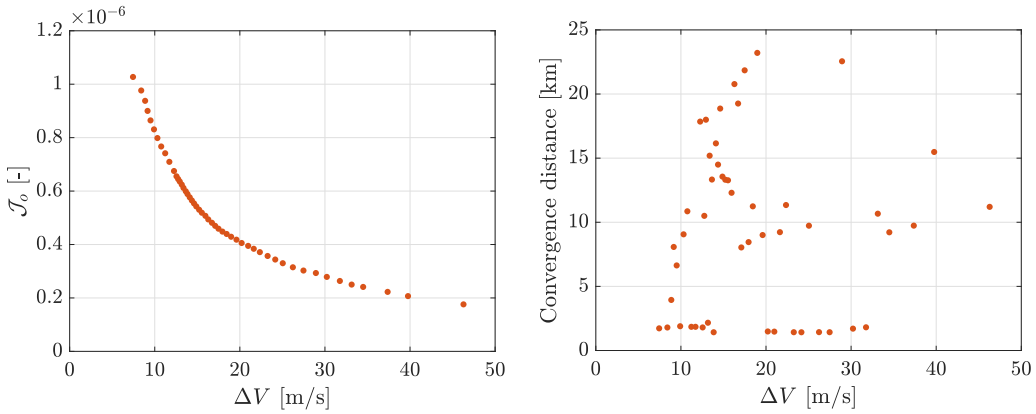

(*a*) Pareto front.

(*b*) Convergence distance.

FIGURE 6.10: Performance for increasing observability weights (i.e., for greater ΔVs) for the quadratic observability objective.

Physically, increasing the observability weight generates larger initial maneuvers to move the chaser towards the final point as fast as possible. Thus, similarly to Figure 6.5, the 1-norm of the absolute error is minimised at the highest ΔV because the chaser spends most of his time in close-proximity of the target. Indeed, recall from (4.49) that in a bearing-only application, the absolute estimation error is proportional to the relative distance. This behaviour is likely connected to the shrinking horizon formulation. In particular, by defining $\mathcal{J}_{o_q}$ as the products between all the discretisation points, the optimisation algorithm finds easier to minimise the objective by reducing as much as possible the norm of the final relative position vectors; leading to a hovering motion around the target for the remaining time. Moreover, although the linear observability objective (LP) enforces the positive linear independence with the original natural motion, the resulting trajectories have the same behaviour of the quadratic metric, since $\mathcal{J}_{o_l}$ embeds the range information as well. Therefore, it could be interesting to investigate the performance of these observability metrics inside a standard MPC guidance; one for which the rendezvous duration is not fixed a-priori and the optimisation is only solved over a small finite horizon.

6.3 Sensitivity Analysis

To prove the robustness of the proposed SH-MPC architecture, the navigation performance are tested over a wide range of orbital families and filter settings. Besides the importance in the field of bearing-only techniques, this analysis will also provide useful insights to aid the implementation of any type of navigation technique in the cis-lunar non-keplerian environment.

6.3.1 Filter settings

All the previous simulations employed an Extended Kalman Filter with a DMC to approximate the unmodelled dynamics. Therefore, it is of interest to present the performances of the architecture when different techniques are used. In particular, in Section 3.3 it was mentioned that a DMC allowed for an easier tuning of the state covariance matrix and at the same time, it properly took into account the time-correlations of the unmodelled dynamics. In this regard, a comparison between the SNC and DMC is shown in Figure 6.11a. The plots present the navigation performance of a rendezvous approach with the same boundary conditions of Case B, however the filter update frequency is decreased to 0.5 Hz. The result suggests that the differences between the two techniques are more conspicuous when the chaser is at an intermediate distance, approximately around 40 km. Then, as the range is decreased, the performance of the SNC improve until the final stages of the rendezvous, where the two lines are almost identical. Nevertheless, although the two methods have similar trends, it is important to remark that the tuning of the DMC has proven to be a much easier task because it has good performance over a broader range of the noise parameters.

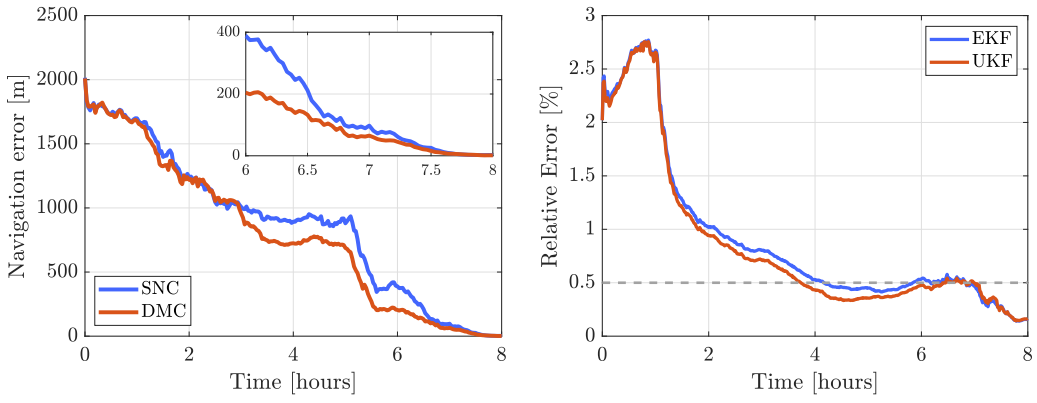

(*a*) SNC vs DMC.

(*b*) EKF vs UKF - 1x Initial Errors.

(*c*) EKF vs UKF - 2x Initial Errors.

(*d*) EKF vs UKF - 3x Initial Errors.

FIGURE 6.11: Filter settings comparisons.

When applied to bearing-only navigation, one of the major limitations of the EKF in cartesian coordinates comes from the linearisation of the measurements equations, which instead are strongly non-linear. As a consequence, further inaccuracies are

introduced in the estimation problem. Therefore, it is reasonable to expect an improvement in the navigation performance when an UKF is adopted. This statement is confirmed by the Figures 6.11b, 6.11c and 6.11d, which present the effects that different initialisation errors have on the navigation quality. The 1x initial errors correspond to a position and velocity uncertainty on each axis of 6 km and 1 m/s, respectively. The error trends show that for small initial uncertainties, the performance of the two filters are quite similar. Yet, when the initial errors increase the EKF is not able to reach convergence because it operates far from its linearisation point. On the other hand the UKF proves more robust, taking an average of 1.18 ms for each iteration with respect to the 0.21 ms of the EKF (with an Intel i7-6700 and a RAM of 16 GB). Nevertheless, for very large initial errors the accuracy threshold is violated for both filters until the chaser arrives in close-proximity of the target. With this in mind, the authors of [18] showed that more accurate results can be obtained by decoupling the observable and unobservable states in the navigation filter. However, to accomplish such task, they implemented a spherical formulation of the CW's equations of motions, one that is currently not available for the non-keplerian dynamics. Moreover, the spherical coordinates made the state equations become non-linear functions of the estimation variables; thus, they would not be compliant with the MPC formulation under study.

6.3.2 Target Propagation Models

To investigate the robustness of this architecture in different orbital families, a few more considerations regarding the knowledge of the target absolute state are worth the attention. By this point, it should be well known that this information is necessary because the state transition matrix of the linearised relative dynamics depends on the motion of the target. In turn, the STM is requested by the guidance and navigation functions at each maneuver and update time, respectively. Previously, it was assumed that the information was passed at each re-optimisation epoch because an active communication link throughout the whole rendezvous might not always be available. In this regard, the chaser could directly interface with the target spacecraft, or be supported by a ground station. The latter option is necessary when the target is uncooperative; for example, when bearing-only is used to improve the absolute navigation of a single spacecraft (see section 6.4). On the other hand, for safety reasons it could be reasonable to assume that in a rendezvous operation, the two spacecraft can directly exchange data among themselves. Additionally, the same considerations hold when the state vector of the chaser is transmitted, as the absolute state of the target is easily obtained through the estimated relative variables. However, whenever that is the case, the target state will be affected by the same level of uncertainty of the navigation estimate and it will be harder to get accurate results. That said, once the absolute orbital information is at hand, different options are available and are summarised in Figure 6.12.

Since the original linear system is time-varying and the shrinking-horizon MPC computes the trajectory from the initial time until the final one, the state information at a given epoch must be propagated on-board over the remaining sample times. Similarly to the relative motion, different levels of approximations can be exploited to compute the absolute dynamics of the target, from a simple CR3BP to a more sophisticated model based on the ephemerides. To maximise the autonomy level of the architecture, it is here assumed that the propagation must be carried out on-board. However, depending on the type of application and on the spacecraft computational

resources, the same process can be performed on ground and the complete history of the trajectory is transmitted when needed. An alternative approach is available by assuming that the time-dependence of the linear system has negligible impact on the relative dynamics for short propagation times (e.g., a typical rendezvous duration). If this hypothesis holds true, the STM can be assumed constant and computed using a single value of the target state, leading to great simplifications in the assembly of the optimisation problem. However, note that the errors introduced by this approximation are also dependent on the shape of the target motion (see Section 6.3.4 for further details).

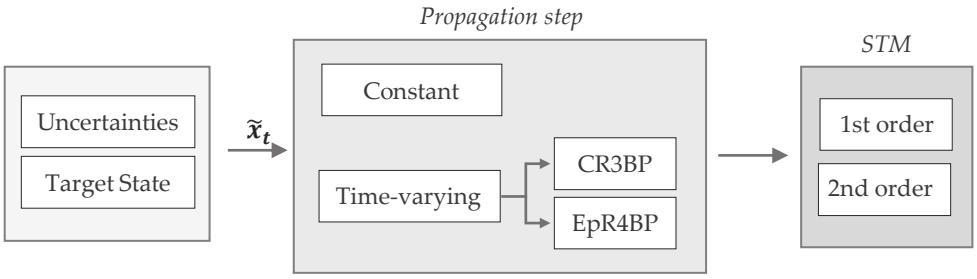

FIGURE 6.12: Target propagation approximations. This process is performed at each re-optimisation epoch.

Regardless of the propagation accuracy, the knowledge of the target absolute state is always affected by an inherent uncertainty, which impacts in different ways both the navigation and guidance algorithms. Regarding the filter, the prediction step at a generic time t_k is written as:

$$\mathbf{x}_{k+1} = \boldsymbol{\Phi}(\mathbf{x}_{t_k})\mathbf{x}_k + \mathbf{G}_k\mathbf{u}_k \tag{6.1}$$

Therefore, the estimation error for $\mathbf{x}_{k+1}$ depends on the previous error at t_k and on the wrong evaluation of $\boldsymbol{\Phi}_k$ due to the inaccuracies of $\mathbf{x}_t$ at the current time. The latter, irrespective of the propagation method, grow proportional to the time passed from the last communication of the target state (i.e., the last re-optimisation epoch). Hence, it is to be expected that the impact of errors in the target state will be greater for longer intervals between two successive transmissions of absolute navigation data.

On the other hand, inside the optimisation problem the STM is exploited to enforce the desired boundary conditions and evaluate the observability metrics. Thus, the inexact knowledge of the target state leads to maneuvers that are incapable of either bringing the chaser to the correct destination point or providing the requested degree-of-observability. However, differently from the navigation filter, the absolute state error at any arbitrary time affects the quality of the solution, since in a SH-MPC the optimisation problem is always solved from the current epoch until the final one. Therefore, when this architecture is implemented, one should always make sure the target does not cross any regions that are characterised by a strong non-linear behaviour. Vice-versa, since in a standard MPC implementation (i.e., with a fixed horizon), the guidance only computes the relative motion over a limited window, the errors in the target dynamics should have a minor impact in the optimisation problem.

On the basis of these considerations, the performance of the proposed architecture

in other cis-lunar regions will mainly depend on their numerical stability and on the ability to correctly predict the motion of the target spacecraft throughout the whole rendezvous duration.

6.3.3 NRHO Rendezvous Region

Previous studies [22] [23] identified the NRHOs perilunes as unfeasible areas to accomplish a rendezvous, since any small perturbation of a state variable generates large deviations in the spacecraft trajectory. Additionally, it was proved that this behaviour is associated to irregularities in the spectrum of the monodromy matrix when evaluated with a full non-linear ephemeris model. In this paragraph, a similar feasible rendezvous region is identified by analysing the performance of the navigation and guidance algorithms for different positions of the target along the whole NRHO. A time anomaly θ_t is used to represent the location of the target on its absolute orbit:

$$\theta_t = 2\pi \frac{t}{T} \tag{6.2}$$

Where T is the orbital period and a null value for the anomaly identifies the aposelene of the orbit. The relative initial conditions are settled on the central manifold of each discretisation point and the rendezvous duration is fixed at 8 hours. Observability is enhanced through the non-linear formulation of the guidance problem and the re-optimisation time is set to 1 hour. In addition, to maximise the accuracy of the GNC architecture, all the on-board propagation models are based on the EpR4BP and the STM is computed with a second-order approximation. The outcomes of the simulations are collected in Figure 6.13 and 6.14, where the x-axis displays the location of the target according to (6.2). Note that each line is the average of 100 Monte Carlo runs.

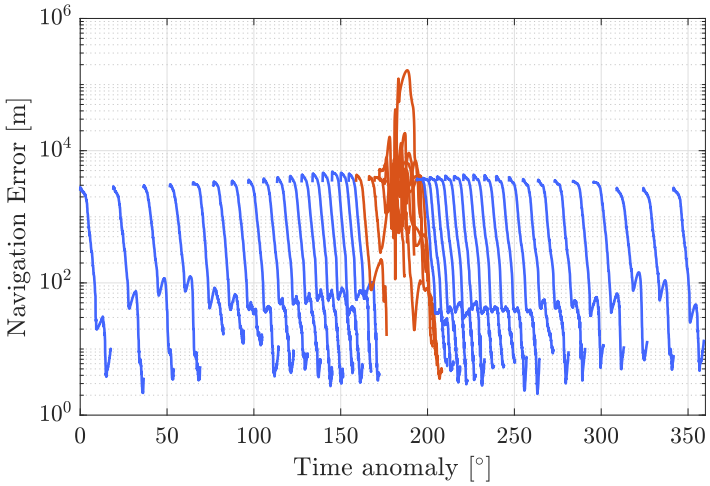

FIGURE 6.13: Navigation error evolution along a NRHO.

It stands quite clear that whenever the target moves in the region between 160 and 200 degrees, the performance of the architecture significantly deteriorate. In particular, the divergence of the navigation filter is caused by the numerical instability of the perilune region: the trajectory predicted with an uncertain relative state results remarkably different from the actual motion because of the high sensitivity to small state perturbations. Successively, the navigation divergence reflects into the inability of the guidance to define a proper maneuver plan. At each re-optimisation, the

chaser finds himself in a completely wrong position and new expensive maneuvers are constantly required to adjust the trajectory.

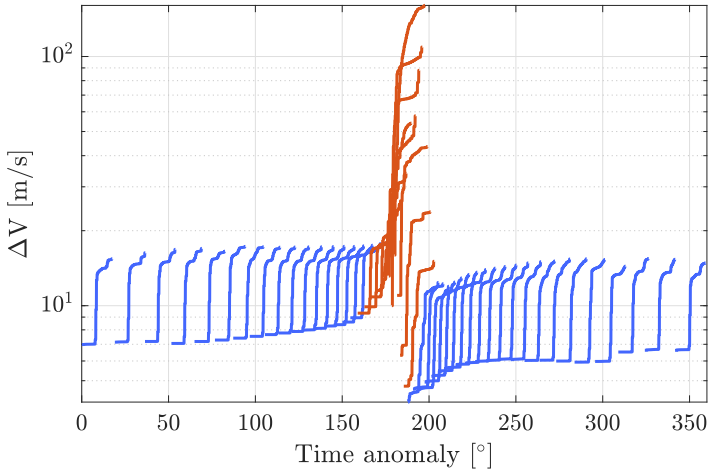

FIGURE 6.14: ΔV requirements along a NRHO.

These results are in agreement with previous studies and confirm once more that the NRHOs perilune region is not a viable candidate to perform a rendezvous. The identified "safe" and "forbidden" regions are depicted in Figure 6.15 and the red area shall be avoided as far as the proposed Bearing-Only guidance-assisted approach is adopted. In particular, since in a shrinking horizon the time of flight is a fixed design variable, the target initial conditions shall be chosen to ensure the spacecraft never reaches the unstable region throughout the whole rendezvous duration. Vice-versa, if the initial position of the target is given, the maximum rendezvous duration equals the time it takes the spacecraft to reach the boundary of the stable region.

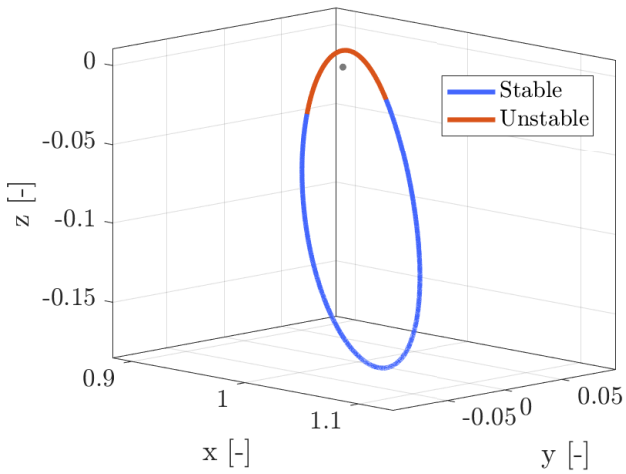

FIGURE 6.15: Suitable rendezvous region in a NRHO.

As a final remark, the performance of the GNC architecture for the different approximation techniques in Figure 6.12 did not show any significant deviations with respect to those presented above. The higher accuracy of the ephemeris second order time-varying model only comes into play for close-proximity operations, where estimation errors below 1 meter are desired.

6.3.4 Time-invariant Approximation

A time-invariant formulation holds many benefits with respect to a time-varying model. In this framework, having a constant expression for the STM allows for an easier assembly of the optimisation problem constraints and an overall reduction of the computational effort required by the GNC functions. In addition, when only the absolute position is available, the target state cannot be propagated forward in time because its velocity is unknown, making a constant first-order STM approximation the only viable approach. To identify the regions where this technique can be exploited, it is helpful to recall the Jacobian expression for the linearised dynamics:

$$\begin{aligned} \mathbf{A}(t) &= \begin{bmatrix} \mathbf{0} & \mathbf{I}_3 \\ \boldsymbol{\Xi}(t) & \mathbf{0} \end{bmatrix} \\ \boldsymbol{\Xi}(t) &= -\left(\frac{1-\mu}{r_{T_1}^3} + \frac{\mu}{r_{T_2}^3} \right) \mathbf{I}_3 + 3\frac{1-\mu}{r_{T_1}^3} \left[\hat{\mathbf{r}}_{T_1} \hat{\mathbf{r}}_{T_1}^{\mathrm{T}} \right] + 3\frac{\mu}{r_{T_2}^3} \left[\hat{\mathbf{r}}_{T_2} \hat{\mathbf{r}}_{T_2}^{\mathrm{T}} \right] \end{aligned} \tag{6.3}$$

The time-dependence is associated with the variations of the relative position vectors of the target with respect to the primaries. Four different time-contributions are identifiable: the magnitudes of the vectors $r_{T_{1/2}}$ and their directions (i.e., the unit vectors $\hat{\mathbf{r}}_{T_{1/2}}$). As the focus is on the cislunar domain, it is reasonable to assume that the variations of the Earth-related terms are negligible because of the much higher distance with respect to the Moon. A proper criterion to establish when the approximation holds is found by evaluating the correlation between the navigation error and the time derivatives of both r_{T_2} and $\hat{\mathbf{r}}_{T_2}$; namely, the range-rate and the rotation velocity of the vector.

Using as a baseline the family of DROs in Figure 6.17a, for each orbit a rendezvous approach based on a constant STM approximation was simulated and the 1-norm of the navigation errors is shown in Figure 6.16 as function of the angular rate of change of $\hat{\mathbf{r}}_{T_2}$. A deterioration of the navigation performance happens for angular speeds higher than 2 mdeg/s, which correspond to the innermost orbits highlighted in red in Figure 6.17b. All the remaining simulations are clustered together, meaning that for lower angular rates, the time-invariant approximation does not affect in a significant way the estimation error.

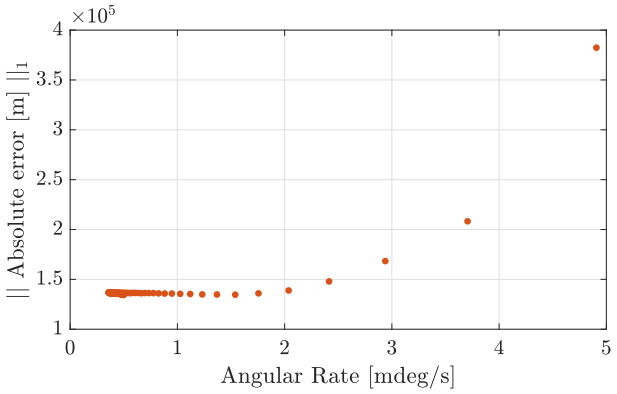

FIGURE 6.16: Time-invariant model validity criterion.

On the other hand, no evident correlation was found between the range-rate and increments of the navigation errors, suggesting that for the cislunar orbital families

a criterion based on the angular rate of $\hat{\mathbf{r}}_{T_2}$ is enough to identify the validity regions for the time-invariant approximation.

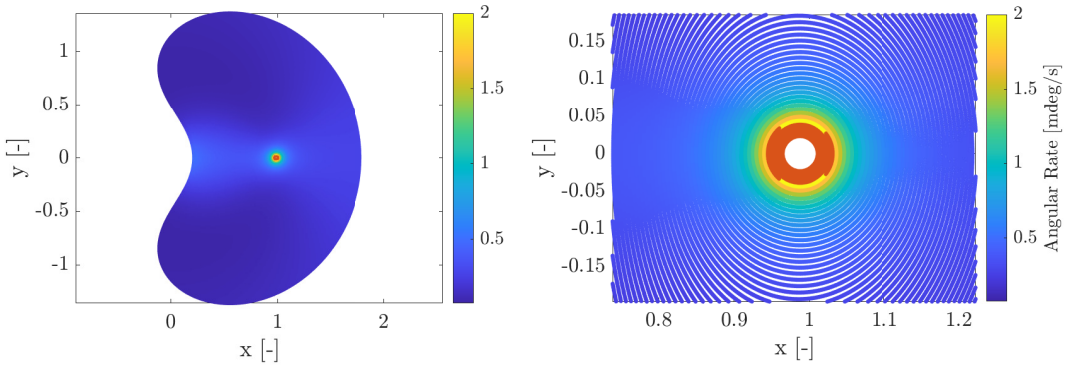

(*a*) DRO. (*b*) DRO zoom-in.

FIGURE 6.17: Angular rate of change of $\hat{\mathbf{r}}_{T_2}$ in a family of DROs. The red markers identify the regions where the time-invariant validity threshold is violated.

The investigation has been expanded to other relevant families in the cislunar domain, as shown in Figures 6.18 and 6.19. The regions where the approximation does not hold are all associated to the close-passages of the spacecraft around the Moon, such as in the NRHOs perilunes. Interestingly, the red areas of the L1/L2 Lyapunov families exhibit the same kind of numerical instability mentioned in the previous section. Indeed, regardless of the propagation method, the proposed architecture is never able to accomplish a safe rendezvous in those areas. Therefore, Figure 6.18 and 6.19 identify the regions were a rendezvous operation shall be avoided with the GNC scheme under study (i.e., the red areas). Viceversa, it is well known that DROs are particularly stable orbits and indeed, any kind of time-varying approximation is accurate enough to perform proximity operations even in the innermost orbits.

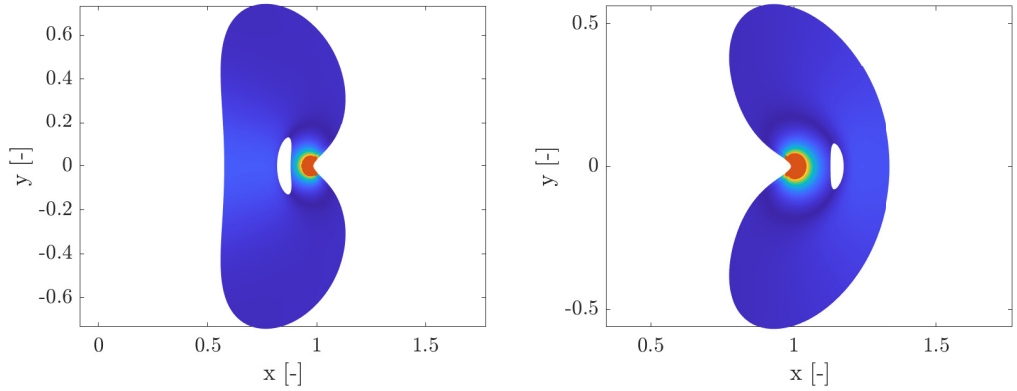

(*a*) Lyapunov L1. (*b*) Lyapunov L2.

FIGURE 6.18: Angular rate of change of $\hat{\mathbf{r}}_{T_2}$ in the L1/L2 CR3BP Lyapunov families. The red markers identify the regions where the time-invariant validity threshold is violated. The color scale is associated to the same values of Figure 6.17.

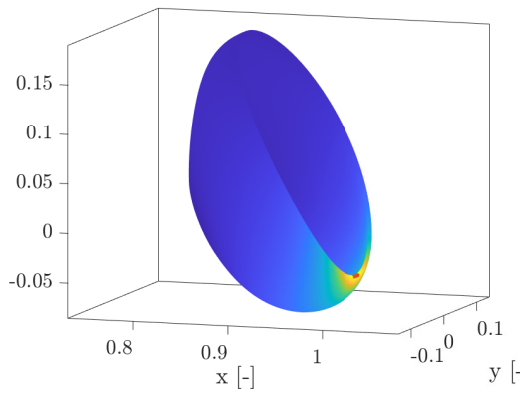

(*c*) Halo L1.

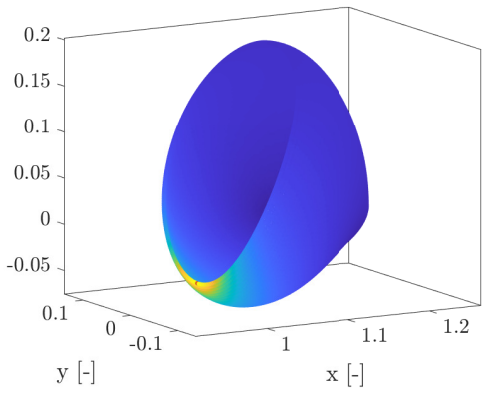

(*d*) Halo L2.

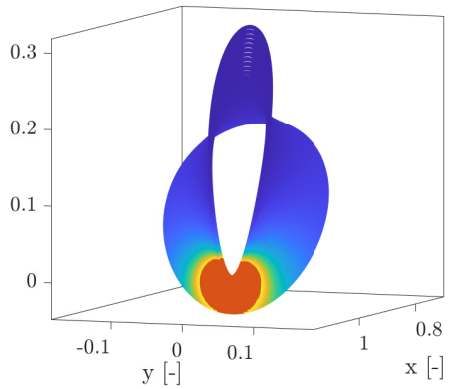

(*e*) NRHO L1.

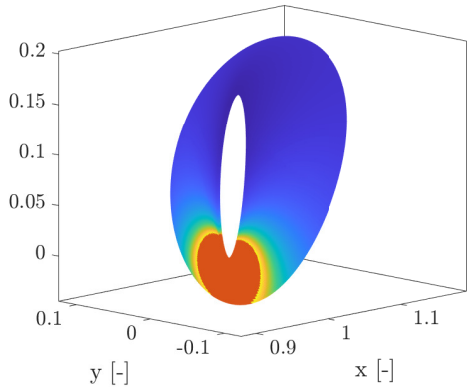

(*f*) NRHO L2.

FIGURE 6.19: Angular rate of change of $\hat{\mathbf{r}}_{T_2}$ in the CR3BP Halo and NRHO orbital families. The red markers identify the regions where the time-invariant validity threshold is violated. The color scale is associated to the same values of Figure 6.17.

6.4 Navigation in Heterogeneous Orbits

The same bearing-only SH-MPC guidance can be adopted by a variety of missions that exploit the relative dynamics of multi-gravitational environments. For example, bearing-only navigation could be used to support a spacecraft during the insertion onto its nominal orbit or throughout a transfer between two distinct locations. This section focuses on assessing the applicability of the proposed GNC architecture to improve the state estimation of a satellite (i.e., the chaser) flying on non-keplerian orbits when the relative distances are in the order of thousands of kilometers. These results will also extend the validity range of this technique with respect to the hundreds of kilometers previously analysed.

The system observability is enhanced through the non-linear formulation by specifying the minimum observability angle of the perturbed motion. The alternative observability metrics based on $\mathcal{J}_o$ resulted completely uncapable of yielding feasible trajectories: by acting on the range they forced the chaser in close-proximity of the target, requiring a ΔV of approximately 600 m/s for an initial distance of 3000 km. In addition, the solution of the multi-objective problem proved to be extremely sensible to the selection of the observability weight, making the method even harder to implement.

6.4.1 DRO to Lyapunov Navigation

To stress the architecture robustness, the scenario selected involves two spacecraft flying on different nominal orbits. The chaser is settled on a L2 Lyapunov while the target is on a DRO, with an initial distance between the spacecraft of 5300 km. Additionally, it is here desired that the chaser remains bounded to its nominal orbit, thus the final boundary conditions of the optimisation problem are set to guarantee that at the end of the relative navigation phase the spacecraft finds himself on its original orbit, as if nothing had happened. The navigation filter is initialised with relative position and velocity uncertainties of 10% and 2.5%, respectively. From an absolute viewpoint, these percentages yield particularly high initial errors because of the great distance between the spacecraft. However, if lower values were selected, much higher observability angles would be required to see an improvement, according to (4.50).

Time Settings	**Value Interval**
Propagation time	72 hours
Re-optimisation time step	5 hours
Discretisation time step	1800 s
Filter update frequency	0.1 Hz

TABLE 6.6: Simulation settings.

The effects of three different desired observability angles are analysed in Figures 6.20 and 6.21. Simultaneously, a comparison between the two fuel cost functions is performed representing high and low-trust engines with the linear and quadratic objectives, respectively. Notice that as the final state is selected on the original nominal orbit, the observability angles at the end of the simulation are always null. However, since the guidance is capable of targeting that position up to a finite accuracy, in practice the final angle is slightly above zero. The constraint on the observability angle has been imposed in the middle of the simulation because the resulting symmetry guarantees the lowest fuel consumption. For example, if the same angles were enforced after 10 hours, the chaser would have to perform larger maneuvers to perturb as much his relative position.

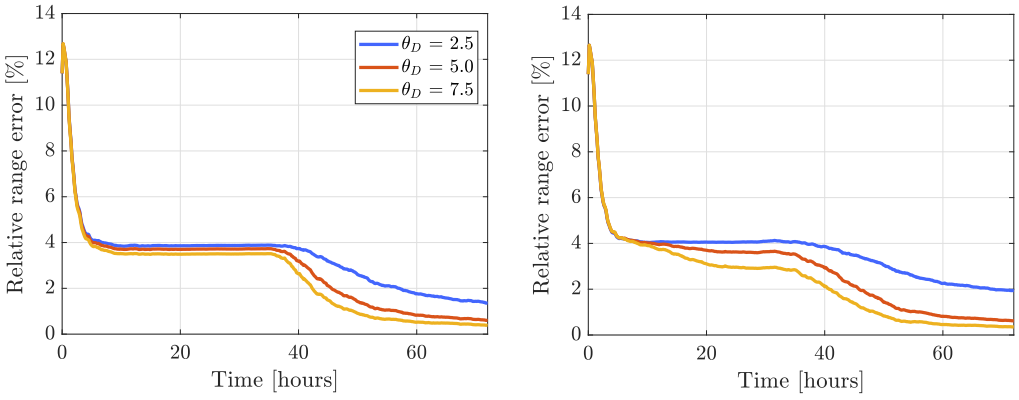

(*a*) Impulsive - Relative estimation error.

(*b*) Low-thrust - Relative estimation error.

FIGURE 6.20: Performance for the relative navigation on heterogeneous orbits (1/2).

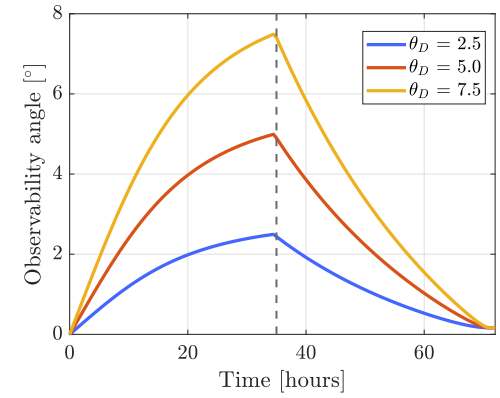

(*c*) Impulsive - Observability angle.

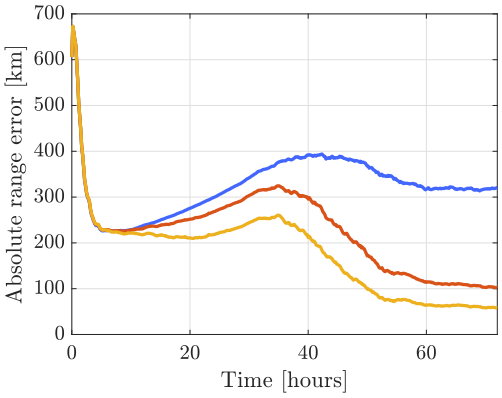

(*b*) Low-thrust - Absolute position error.

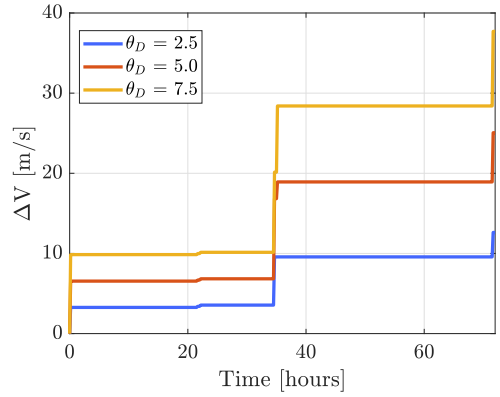

(*e*) Impulsive - ΔV.

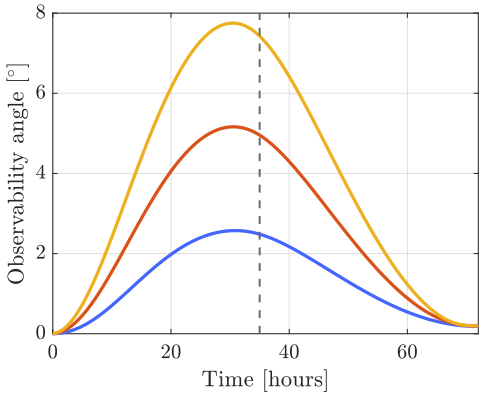

(*d*) Low-thrust - Observability angle.

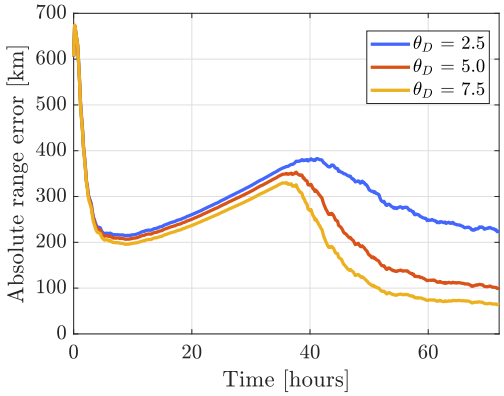

(*a*) Impulsive - Absolute position error.

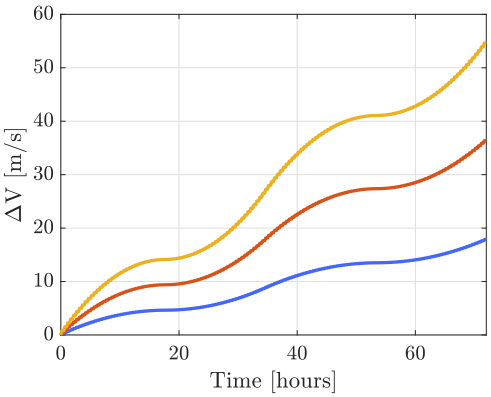

(*f*) Low-thrust - ΔV.

FIGURE 6.21: Performance for the relative navigation on heterogeneous orbits (2/2). The dotted line represents where the observability constraint is enforced.

The two engines result in similar navigation performance, although the low-thrust always requires an extra 10 m/s. The lowest relative error (the yellow line) is around the 0.4% of the range, which corresponds to approximately 60 km; 10 times lower than the original value. Interestingly, for the high-thrust case the greater improvements of the navigation error happen immediately after the execution of the maneuvers, and then remain approximately constant throughout the whole coasting phase. However, since the distance between the spacecraft keeps increasing, the absolute estimation error increases as well.

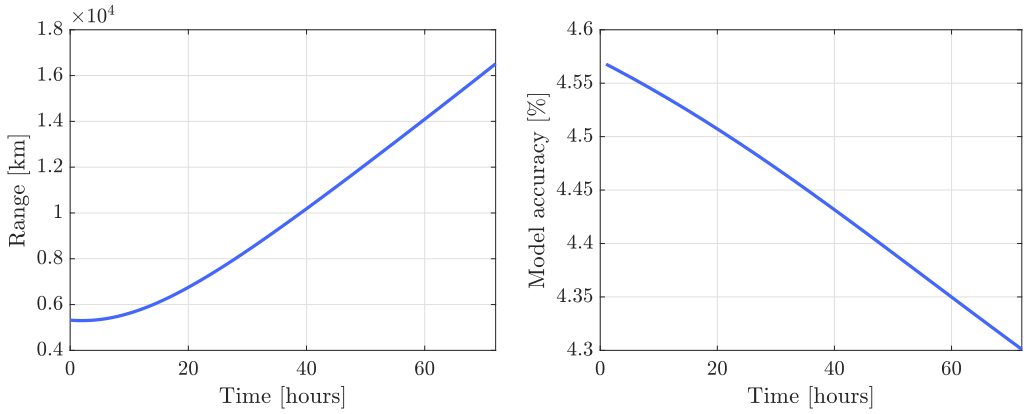

(*c*) Range evolution .

(*d*) Linear model accuracy metric.

FIGURE 6.22: Relative range evolution. Only one line is reported because the range differences between the various approaches are minimal.

A few considerations can be extrapolated from these outcomes. When the goal is to reduce the absolute uncertainty below a given threshold, various possibilities are available. If the target is fixed (i.e., the relative distance), the necessary observability angle is directly obtained from (4.49). On the other hand, if different spacecraft can be exploited as a target for measurements, it is more convenient to choose either the one that is closer to the chaser or that which naturally maximises the observability angle at the desired final location. An alternative is to select a target satellite such that the range reduces in time (contrary to the above configuration). In this test scenario, a relatively high distance was selected with the sole purpose of proving the validity of the GNC architecture. However, it is always desirable to work with smaller distances because, given the angle θ, the ΔV required to perturb the natural trajectory grows as function of the range between the spacecraft.

As a last remark, the accuracy of the linear model deteriorates as the ratio between the spacecraft distance and the target to Moon distance increases. On the basis of multiple numerical simulations, it was found that the model performs relatively well as long as the ratio does not exceed the 10%. In this regard, it is interesting to notice that in the simulations of section 6.3.3, the ratio at the NRHO perilune was approximately around 3%; confirming that the inability of the GNC architecture to navigate in that region is not due modelling errors but rather to the numerical instability of the area.

Chapter 7

Conclusions

The present thesis investigated several challenging aspects connected with the usage of bearing-only techniques to perform proximity operations in the cislunar space. In this final chapter, the most important outcomes and discoveries are summarised, together with few suggestions for the development of future works.

7.1 Summary

Starting from the formalisation of the 3 DOF non-keplerian dynamics, a discrete-form solution of the linearised relative dynamic model was presented to support the analysis of the observability problem and the development of GNC functions. The implementation of this linear framework inside navigation filters has been discussed from a computational viewpoint, highlighting how simple approximations are exploitable for real-time dynamic predictions in the cislunar domain. Extensive numerical tests showed that the linear model is well capable of capturing the shape of the relative motion as long as the spacecraft are located in numerical stable regions. A brief mention of real-world applications was made to discuss the effects that different camera properties have on measurement errors, revealing the impossibility to estimate the relative range from the target dimensions on the camera focal plane.

Existing geometrical and analytical frameworks have been exploited to illustrate the inherent unobservability of bearing-only navigation. The comparisons with the real dynamics have shown that non-linear gravitational and perturbing accelerations are unable to provide a significant enhancement of observability. This led to the conclusion that even in the non-keplerian space, to guarantee the convergence of the navigation filter dedicated maneuvers must be executed to perturb the trajectory from its from its natural evolution without maneuvers. In addition, through this observability criterion, the initial conditions for unobservable maneuvers in LEO were identified for any kind of linear time-varying system.

A general framework for the implementation of Model Predictive Control techniques in the non-keplerian domain has been derived, showing how system engineering limitations and trajectory planning can be incorporated into a single optimisation problem solvable with simple linear programming algorithms. Two different fuel objectives were investigated, discovering that a quadratic control objective provides a simple way to account for low-thrust propulsion inside the optimisation problem. The exploitation of this formulation allowed to develop a novel quasi-autonomous architecture to perform proximity operations with angles-only measurements. In addition, non-linear inequality constraints have been employed to enforce a desired observability angle and favour the convergence of the navigation filter. A numerical

testing campaign was used to validate the capability of the proposed GNC scheme to meet safety and navigation requirements throughout the whole relative approach, with a specific focus on rendezvous operations at the apolune of the NASA LOP-G NRHO. A similar already-existing guidance, which was able to achieve satisfactory results in LEO, has been generalised to a time-varying system and used as a benchmark to compare the performance of our architecture. The outcomes highlighted that in the non-keplerian dynamics, the minimisation of an observability measure based on the positive linear independence of the natural and perturbed relative position vectors generates trajectories with an extremely low degree-of-observability. In particular, it was inferred that in the cislunar space the minimisation of an objective which includes information on the range always favours a reduction of the relative distance rather than an increment on the observability angle. As a consequence, the resulting trajectories are likely to violate any relative accuracy threshold for most of the approach. On the other hand, by directly targeting the angle, the guidance scheme here proposed effectively reduced the navigation error whilst remaining at relatively high distances from the target. In addition, due to its simple formulation, the optimisation problem resulted computationally efficient, with solving times in the order of fractions of a second.

Through a sensitivity analysis the effects of various navigation settings and propagation models were evaluated. The adoption of UKF proved particularly useful for large initialisation errors, as the EKF is not able to reach convergence when it operates far from its linearisation point. Different simulations along the NRHO confirmed that the periselene of the orbit is not a suitable area to perform rendezvous operations as the numerical instability of the region prevents the navigation filter from reaching convergence. A time-invariant approximation for the target motion is suggested to partially overcome the constant need of knowing the absolute state of either spacecraft. The analysis on the validity range of this model allowed to define critical regions in proximity of the Moon where rendezvous operations are unfeasible regardless of the propagation method, such as the NRHO and L1/L2 Lyapunov perilunes. Finally, the versatility of the proposed architecture was assessed by successfully employing it to perform relative navigation between spacecraft flying on distant heterogeneous non-keplerian orbits. Nevertheless, the results highlighted that to minimise the absolute navigation error, it is desirable to choose a target object that naturally reduces the relative distance throughout the navigation phase.

7.2 Future Works

A few recommendations to extend the work presented in this thesis are here suggested.

Standard MPC A shrinking horizon MPC was here adopted to have a common ground to compare the performance of bearing-only navigation between LEO and the cislunar space. The implementation of a standard MPC with a fixed horizon sliding window could improve the architecture robustness to external perturbations and control malfunctions. Additionally, it would be interesting to investigate the behaviour coming from the minimisation of the linear and quadratic observability objective when only few discretisation points are accounted for.

6 DoF dynamics The GNC architecture proposed in this work focused on the estimation of the relative position and velocity only, using a 3 degrees-of-freedom model. For a comprehensive analysis of the rendezvous approach, the design should also incorporate the relative attitude dynamics together with the development of a control scheme to guarantee the target remains in-view of the on-board cameras throughout the whole approach phase.

Filtering techniques For large initialisation errors the EKF struggles to reach convergence in reasonable times because it operates far from the linearisation point. In the recent years, many alternative non-linear filters have been proposed to deal with the estimation from bearing-only measurements. For example, [11] developed a Pseudo-Measurement Filter that completely outperformed the EKF for large estimation errors. On the other hand, [17] developed accurate and computationally efficient Shifted Rayleigh Filter for the angles-only problem, although its performance were not tested for in-orbit applications. Thus, a future investigation could evaluate and compare the estimation capability of different bearing-only filter formulations as function of the initialisation errors.

Bibliography

[1] LAURINI, KATHY et al. *The Global Exploration Roadmap*. In: IAC-11 B 3 (2018).

[2] HAMMEL, SHERRY et al. *Observability requirements for three-dimensional tracking via angle measurements*. In: IEEE Transactions on Aerospace and Electronic Systems 2 (1985).

[3] NARDONE, STEVEN C et al. *A closed-form solution to bearings-only target motion analysis*. In: IEEE Journal of Oceanic Engineering 22.1 (1997).

[4] RISTIC, BRANKO et al. *Tracking a manoeuvring target using angle-only measurements: algorithms and performance*. In: Signal processing 83.6 (2003).

[5] SABOL, CHRIS et al. *A fresh look at angles-only orbit determination*. In: (1999).

[6] WOFFINDEN, DAVID C. *Angles-only navigation for autonomous orbital rendezvous*. PhD thesis. 2008.

[7] GRZYMISCH, JONATHAN et al. *Observability criteria and unobservable maneuvers for in-orbit bearings-only navigation*. In: Journal of Guidance, Control, and Dynamics 37.4 (2014).

[8] GRIFFITH, ERNEST WILLIAM et al. *On the observability of nonlinear systems: I*. In: Journal of Mathematical Analysis and Applications 35.1 (1971).

[9] D'AMICO, SIMONE et al. *Noncooperative rendezvous using angles-only optical navigation: system design and flight results*. In: Journal of Guidance, Control, and Dynamics 36.6 (2013).

[10] ARDAENS, JEAN-SÉBASTIEN et al. *Flight demonstration of spaceborne real-time angles-only navigation to a noncooperative target in low earth orbit*. In: Acta Astronautica 153 (2018).

[11] GRZYMISCH, JONATHAN et al. *Bearings-Only Rendezvous with Enhanced Performance*. In: *Advances in Aerospace Guidance, Navigation and Control*. Springer, 2015.

[12] GRZYMISCH, JONATHAN et al. *Analytic optimal observability maneuvers for in-orbit bearings-only rendezvous*. In: Journal of Guidance, Control, and Dynamics 37.5 (2014).

[13] GRZYMISCH, JONATHAN et al. *Optimal rendezvous guidance with enhanced bearings-only observability*. In: Journal of Guidance, Control, and Dynamics 38.6 (2015).

[14] CHARI, RAJA JON VURPUTOOR. *Autonomous orbital rendezvous using angles-only navigation*. MA thesis. Massachusetts Institute of Technology, 2001.

[15] SPURMANN, J. *Spiraling approach for angles-only navigation within on-orbit servicing missions*. In: (2011).

[16] MOK, SUNG-HOON et al. *One-step rendezvous guidance for improving observability in bearings-only navigation*. In: Advances in Space Research 66.11 (2020).

[17] OZELCI, ATTILA CAN. *Tracking and estimation algorithms for bearings only measurements*. In: (2013).

[18] GRZYMISCH, JONATHAN et al. *A Spherical Coordinate Parametrization for an In-Orbit Bearings-Only Navigation Filter*. In: (2013).

[19] WHITLEY, RYAN et al. *Options for staging orbits in cislunar space*. In: *2016 IEEE Aerospace Conference*. IEEE. 2016.

[20] DAVIS, DIANE et al. *Orbit maintenance and navigation of human spacecraft at cislunar near rectilinear halo orbits*. In: (2017).

[21] WILLIAMS, JACOB AND LEE et al. *Targeting cislunar near rectilinear halo orbits for human space exploration*. In: (2017).

[22] BUCCI, LORENZO. *Mission analysis and operational aspects for a lunar exploration architecture*. PhD thesis. 2020.

[23] COLAGROSSI, ANDREA. *Absolute and relative 6DOF dynamics, guidance and control for large space structures in cislunar environment*. PhD thesis. 2019.

[24] COLOMBI, FRANCESCO. *Characterization of relative 6DOF natural and controlled dynamics in cislunar space*. MA thesis. 2019.

[25] HARTLEY, EDWARD N. *A tutorial on model predictive control for spacecraft rendezvous*. In: *2015 European Control Conference (ECC)*. IEEE. 2015.

[26] SILVESTRINI, STEFANO et al. *Design of Robust Passively Safe Relative Trajectories for Uncooperative Debris Imaging in Preparation to Removal*. In: *2020 AAS/AIAA Astrodynamics Specialist Conference*. 2020.

[27] BERNING JR, ANDREW W et al. *Suboptimal Nonlinear Model Predictive Control Strategies for Tracking Near Rectilinear Halo Orbits*. In: (2020).

[28] LUQUETTE, RICHARD J. *Nonlinear control design techniques for precision formation flying at lagrange points*. PhD thesis. 2006.

[29] BUCCI, LORENZO et al. *Rendezvous in lunar near rectilinear halo orbits*. In: Advances in Astronautics Science and Technology 1.1 (2018).

[30] PESCE, VINCENZO. *Autonomous navigation for close proximity operations around uncooperative space objects*. In: (2019).

[31] SZEBEHELY, VICTOR et al. *Theory of Orbits-The Restricted Problem of Three Bodies*. Vol. 13. 1969.

[32] PAVLAK, THOMAS A. *Mission design applications in the earth-moon system: Transfer trajectories and stationkeeping*. MA thesis. 2010.

[33] VALLADO, DAVID A. *Fundamentals of astrodynamics and applications*. Vol. 12. Springer Science & Business Media, 2001.

[34] CURTIS, HOWARD D. *Orbital mechanics for engineering students*. Butterworth-Heinemann, 2019.

[35] ZIMOVAN, EMILY M. *Characteristics and design strategies for near rectilinear halo orbits within the Earth-Moon system*. PhD thesis. 2017.

[36] GUZZETTI, DAVIDE. *Coupled orbit-attitude mission design in the circular restricted three-body problem*. PhD thesis. 2016.

[37] GREBOW, DANIEL J. *Trajectory design in the Earth-Moon system and lunar South Pole coverage*. PhD thesis. 2010.

[38] GREBOW, DANIEL J. *Generating periodic orbits in the circular restricted three-body problem with applications to lunar south pole coverage*. MA thesis. 2006.

[39] WOFFINDEN, DAVID C et al. *Observability criteria for angles-only navigation*. In: IEEE Transactions on Aerospace and Electronic Systems 45.3 (2009).

[40] CARPENTER, J RUSSELL et al. *Navigation filter best practices*. 2018.

[41] SCHUTZ, BOB et al. *Statistical orbit determination*. Elsevier, 2004.

[42] YOU, DAZHANG et al. *An Improved Unscented Kalman Filter Algorithm for Radar Azimuth Mutation*. In: International Journal of Aerospace Engineering 2020 (2020).

[43] JULIER, SIMON J et al. *New extension of the Kalman filter to nonlinear systems*. In: *Signal processing, sensor fusion, and target recognition VI*. Vol. 3068. International Society for Optics and Photonics. 1997.

[44] WAN, ERIC A et al. *The unscented Kalman filter*. In: Kalman filtering and neural networks 5.2007 (2001).

[45] VAN DER MERWE, RUDOLPH et al. *The square-root unscented Kalman filter for state and parameter-estimation*. In: *2001 IEEE international conference on acoustics, speech, and signal processing. Proceedings (Cat. No. 01CH37221)*. Vol. 6. IEEE. 2001.

[46] KOU, SHAUYING R. et al. *Observability of nonlinear systems*. In: Information and Control 22.1 (1973).

[47] ZENG, SHEN. *Observability measures for nonlinear systems*. In: *2018 IEEE Conference on Decision and Control (CDC)*. IEEE. 2018.

[48] PI, JAEHWAN et al. *Trajectory design for improving observability of angles-only relative navigation between two satellites*. In: The Journal of the Astronautical Sciences 61.4 (2014).

[49] FEHSE, WIGBERT. *Automated rendezvous and docking of spacecraft*. Vol. 16. Cambridge university press, 2003.

[50] GRZYMISCH, JONATHAN. *Bearings-only guidance and navigation for in-orbit rendezvous*. Shaker, 2015.

[51] MARLER, R TIMOTHY et al. *Survey of multi-objective optimization methods for engineering*. In: Structural and multidisciplinary optimization 26.6 (2004).

[52] DAS, INDRANEEL et al. *A closer look at drawbacks of minimizing weighted sums of objectives for Pareto set generation in multicriteria optimization problems*. In: Structural optimization 14.1 (1997).

[53] MESSAC, ACHILLE et al. *The normalized normal constraint method for generating the Pareto frontier*. In: Structural and multidisciplinary optimization 25.2 (2003).

[54] PAZ, AZARIA et al. *Non deterministic polynomial optimization problems and their approximations*. In: Theoretical Computer Science 15.3 (1981).

[55] DAS, INDRANEEL et al. *Normal-boundary intersection: A new method for generating the Pareto surface in nonlinear multicriteria optimization problems*. In: SIAM journal on optimization 8.3 (1998).

[56] COLAGROSSI, ANDREA et al. *Dynamical analysis of rendezvous and docking with very large space infrastructures in non-Keplerian orbits*. In: CEAS Space Journal 10.1 (2018).